# RECONSTRUCTING DUST FLUXES AND SEDIMENT FOCUSING IN THE EQUATORIAL PACIFIC OVER GLACIAL AND INTERGLACIAL TIME-SCALES USING GRAIN SIZE ANALYSIS

by

Diksha Bista

Submitted in partial fulfillment of the requirements
for the degree of Master of Science

at

Dalhousie University
Halifax, Nova Scotia
June 2015

*To my mother*

*without whom I would not be here*

*&*

*In memory of*

*my father*

# TABLE OF CONTENTS

# LIST OF TABLES

# LIST OF FIGURES

# ABSTRACT

Understanding paleo-dust fluxes can provide insights into the dust cycle and its interaction with other components of the Earth's system. In high nutrient low chlorophyll regions like the equatorial Pacific, dust mediates the biogeochemical exchange of carbon between the atmosphere and ocean. However, the interpretation of sediments in this region has been controversial. This thesis presents new disaggregated inorganic grain size (DIGS) distributions of several marine sediment cores from this region, focusing on the last 30,000 yrs. DIGS data are used to derive dust fluxes and to investigate sediment redistribution on the sea floor. Dust fluxes in the eastern equatorial Pacific (EEP) were highest in the deglaciation (15,000 - 18,000 yrs B.P.), rather than during the full glacial period, as previously observed. Furthermore, grain size sorting coefficients show that sediments in the EEP are moderately to well sorted, thus supporting geochemical evidence for sediment reworking in this region.

# LIST OF ABBREVIATIONS AND SYMBOLS USED

| Abbreviation | Description |
|---|---|
| HNLC | High Nutrient Low Chlorophyll |
| $^{232}$Th | Thorium-232 |
| LGM | Last Glacial Maximum |
| MAR$_i$ | Mass Accumulation Rate of component i |
| $^{230}$Th | Thorium-230 |
| $^{234}$U | Uranium-234 |
| DIGS | Disaggregated Inorganic Grain Size |
| EEP | Eastern Equatorial Pacific |
| TR-19 | Sediment core TR163-19 |
| ME-27 | Sediment core ME0005A-27JC |
| ME-24 | Sediment core ME0005A-24JC |
| PC-72 | Sediment core TTN013-PC72 |
| MIS | Marine Isotopic Stage |
| $\delta^{18}$O | Change in ratio of stable oxygen isotopes $^{18}$O to $^{16}$O relative to a standard, in ‰ |
| SPT | Sodium Polytungstate |
| SEM | Scanning Electron Microscope |
| SS | Sortable Silt |
| G-IG | Glacial-Interglacial |

| Symbol | Description | Units |
|---|---|---|
| $z$ | Water depth | m |
| $\beta_{230}$ | Production rate of $^{230}$Th | dpm m$^{-3}$ yr$^{-1}$ |
| $^{230}\mathrm{Th}_{xs,0}$ | Excess scavenged thorium concentration at the time of deposition | dpm g$^{-1}$ |
| $F_v$ | Bulk vertical flux | g m$^{-2}$ yr$^{-1}$ |
| $F_i$ | Vertical flux of a component "i" | g m$^{-2}$ yr$^{-1}$ |
| $f_m$ | Volume fraction in size class "m" | % |
| $V_{ij}$ | Total volume between grain size $i$ and $j$ | % |
| $V_{ss}$ | Total volume in sortable silt size range ( 10 - 63 $\mu$m) | % |
| $\mathrm{Dust}_{Th}$ | $^{232}$Th-based dust flux | g m$^{-2}$ yr$^{-1}$ |
| $\mathrm{Dust}_{GS}$ | Grain size-based dust flux | g m$^{-2}$ yr$^{-1}$ |
| $\sigma_g$ | Geometric standard deviation (sorting coefficient) | - |
| $\overline{x_g}$ | Geometric grain size mean | $\mu$m |
| $\Psi$ | Focusing factor | - |
| $\rho$ | Dry bulk density of the sediment | kg m$^{-3}$ |

# ACKNOWLEDGEMENTS

First and foremost, I would like to thank my supervisor Dr. Stephanie Kienast for her immense support throughout this thesis and my time at Dalhousie. Her encouragement and guidance have been invaluable these last three years. Stephanie has been the best supervisor and mentor I could have hoped for. In addition, I would like to thank my committee members Dr. Paul Hill, Dr. Markus Kienast and Dr. Ian Folkins for their advice, feedback, and comments. Their guidance has been a crucial part of my thesis completion.

Outside the Department of Oceanography, I would like to acknowledge the Particle Dynamics Lab at BIO for providing access to the Plasma Asher. I am grateful to Vanessa Zion and Casey O'Laughlin for putting their time and efforts towards processing my samples. I would also like to thank Matt Kliffer from Dalhousie's Earth Sciences Department for teaching me the use of heavy density liquid. In addition, a big thank you to Dr. David McGee from the Department of Earth, Atmospheric and Planetary Sciences, Massachusetts Institute of Technology, Cambridge for sharing his MATLAB code as well as his expertise on the end member modeling.

I would like to thank Elizabeth Kerrigan, Erin Wilson and Nadine Lehmann for providing their valuable input on the academic and (mostly) non-academic matters. A big thank you to Dalhousie Oceanography Student Association (DOSA) for making my time at Dal an amazing experience. Also, I would like to recognize all my friends and colleagues (present and past) for their help and support, and my family for their continuous love and encouragement.

# CHAPTER 1

# INTRODUCTION

The equatorial Pacific spans one-third of the Earth's circumference and is one of the major high nutrient low chlorophyll (HNLC) regions of the ocean. The nutrients brought to the surface by upwelling by the equatorial divergence are not immediately utilized by phytoplankton due to the limited availability of iron in this region. Iron enrichment experiments have shown that adding dissolved iron in the equatorial Pacific (*Coale et al.*, 1996) and in other HNLC regions (*Boyd et al.*, 2007)stimulates phytoplankton growth. Thus, atmospheric dust input and its associated iron content may also increase primary productivity. Even with the iron-limitation, the equatorial Pacific has high primary productivity (*Chavez and Barber*, 1987; *Antoine et al.*, 1996) and thus provides a significant vertical flux of carbon to the deep sea. Because of this, the equatorial Pacific is an area of great interest for present and past biogeochemical studies.

## 1.1 The Equatorial Pacific Dust Flux

Atmospheric dust is important in the climate system for several reasons. Dust affects Earth's radiative balance by both absorbing and scattering incoming solar radiation and outgoing planetary radiation (*Tegen and Lacis*, 1996; *Miller and Tegen*, 1998). Dust also has an indirect effect on the earth's radiative budget because dust particles act as cloud condensation nuclei (*Twomey et al.*, 1984; *Duce*, 1995). In addition, dust significantly affects marine and terrestrial biogeochemical cycles because of its iron content (*Mahowald et al.*, 2006, 2011). Several iron fertilization experiments have demonstrated that phytoplankton

growth, especially of large diatoms, is limited by iron in HNLC regions (e.g., *Coale et al.*, 1996; *Boyd et al.*, 2007; *Brzezinski et al.*, 2011; *Dugdale et al.*, 2011). Dust deposition is thought to increase productivity in HNLC regions of the ocean such as the equatorial Pacific. Consequently, the supply of dust has strong implications for the partitioning of carbon between ocean and atmosphereic reservoirs and may have played a direct role in forcing past climate change (*Broecker and Henderson*, 1998; *Martin*, 1990; *Harrison et al.*, 2001).

Dust deposition is highly variable in time and space. Records of paleo-dust deposition can provide information about the intensity of atmospheric circulation, transport pathways, and environmental conditions of the source region (*Rea*, 1994; *Kohfeld and Harrison*, 2001; *Harrison et al.*, 2001, and references therein). Significant efforts have been made to understand the spatial and temporal variability of the dust deposition (*Rea*, 1994; *Kohfeld and Harrison*, 2001; *Maher et al.*, 2010). Dust has been incorporated in global climate models to investigate the climate-related variability in dust deposition as well as dust related feedbacks on the global climate system (*Bopp et al.*, 2003; *Reader et al.*, 1999; *Mahowald et al.*, 1999, 2006; *Mahowald*, 2011; *Albani et al.*, 2014, and others). The effect of dust on the climate system, however, is still not properly understood (*IPCC*, 2013, WG1 Chapter 5, 7, and 9), in part because observations of dust deposition in the ocean are still sparse.

Paleo-dust flux reconstructions in the equatorial Pacific have large spatial gaps. Until recently, the reconstruction of glacial-interglacial trends in dust flux in this region was crude. The traditional method of calculating accumulation rates, based on linear sedimentation rate, showed inconsistent results. For example, *Rea* (1994) found higher interglacial dust fluxes whereas *Murray et al.* (1995) did not find coherent glacial-interglacial dust flux patterns in the equatorial Pacific. However, the development of $^{230}$Th normalization (Section 1.2.2) has recently provided a more appropriate approach to estimate past fluxes in the ocean.

Thorium-232 ($^{232}$Th), in conjunction with $^{230}$Th normalization, is an increasingly used proxy for reconstructing dust flux to the ocean. $^{232}$Th is a primordial isotope and is significantly enriched in continental crust ($\sim$10.7 ppm) compared with oceanic crust and mid ocean ridge basalts ($\sim$0.2 ppm, *Taylor and McLennan*, 1985). In regions where there

are no other significant terrigenic inputs, $^{232}$Th found in marine sediments is from eolian sources and can thus be used as a proxy for dust. *Anderson et al.* (2006), *McGee et al.* (2007) and *Winckler et al.* (2008) used this approach and observed increased dust fluxes during glacial periods in the equatorial Pacific. Dust fluxes were higher by a factor of 2 during the Last Glacial Maximum (LGM, 18 - 23 ka[1]) compared to the Holocene (0 - 10 ka) and decreased from west ($\sim$160° E) to east ($\sim$110° W) and from north ($\sim$7° N) to south ($\sim$3° S). In addition to the elevated dust fluxes during the LGM, *Kienast et al.* (2013) found a dust flux maximum during the Heinrich Stadial 1 (HS-1, 15 - 18 ka) in the eastern equatorial Pacific (EEP) at $\sim$86° W.

These glacial-interglacial dust flux trends in the equatorial Pacific are different from modeled dust flux values. Early models by *Mahowald et al.* (1999) and *Reader et al.* (1999) produced LGM to modern dust flux ratios ranging between 12 and 105. These ratios are considered unrealistically large (*Winckler et al.*, 2008; *Maher et al.*, 2010). With the improvement of model simulations, more comparable values have been estimated (*Jickells et al.*, 2005; *Mahowald et al.*, 2006, 2011; *Albani et al.*, 2014). However, uncertainty within and differences between the models are still high. To constrain these uncertainties, more spatially resolved observational data are required.

## 1.2 Approaches for Vertical Flux Estimates

Considerable efforts have been made to reconstruct paleoproductivity in the equatorial Pacific and to understand its link to climate variability on glacial-interglacial time scales. Several biological and geochemical proxies have been developed for reconstructing past changes in productivity and vertical flux (*Averty and Paytan*, 2004). These proxies usually quantify changes in the burial flux of a biogenic component, which is then used to estimate vertical flux and paleoproductivity (*Murray and Leinen*, 1993; *Paytan et al.*, 1996; *Murray et al.*, 2012).

[1] 1 ka = 1000 years.

### 1.2.1 Mass Accumulation Rate Method

Traditionally, the burial flux of a component is quantified by calculating its mass accumulation rates (MAR). This approach uses the dry bulk density (dry weight/ wet volume) of the sediment, the linear sedimentation rate (LSR) between dated horizons and the concentration of the component of interest (*DeMaster*, 1981; *Curry and Lohmann*, 1986; *Francois et al.*, 2004).

$$MAR_i = \rho \times LSR \times [i]_{z1}^{z2} \tag{1.1}$$
$$LSR = \frac{z_2 - z_1}{t_2 - t_1}$$

$MAR_i$ is the accumulation rate of component i in the sediment, $\rho$ is the dry bulk density of the sediment (g $cm^{-3}$), LSR is the linear sedimentation rate (cm $kyr^{-1}$), $z_1$ and $z_2$ are the depths (cm) of sediment horizons 1 and 2, $t_1$ and $t_2$ are the corresponding ages (kyr), and [i] is the concentration of component i averaged over the sediment depth interval. This approach of calculating accumulation rate is still widely used. In recent years the validity of this approach has been questioned, particularly in the equatorial Pacific.

The errors associated with this method can be large because of uncertainties with the age models, the requirement to assume linear sedimentation rates between dated horizons and the errors related to the measurement of dry bulk density. The most prominent potential error, however, is due to the lack of distinction between vertical flux from the overlying water column (variable of interest) and lateral flux from sediment redistribution on the sea floor due to bottom currents. Syndepositional sediment redistribution can lead to significant overestimation of accumulation rates in areas where sediments are added, and underestimation where sediments are removed due to bottom current activity (*Marcantonio et al.*, 2001; *Francois et al.*, 2004; *Kienast et al.*, 2007).

### 1.2.2 $^{230}$Th Normalization Method

To overcome the effect of sediment redistribution, *Bacon* (1984) and *Suman and Bacon* (1989) proposed and developed a method of estimating vertical fluxes to the sea floor using thorium isotope measurements in marine sediments. Thorium-230 ($^{230}$Th) is a radioactive isotope produced in sea water during the decay of Uranium-234 ($^{234}$U). Uranium, added

to the ocean via rivers and groundwater, has a very long residence time (320-560 ka) and behaves conservatively in the water column (*Dunk et al.*, 2002). While residing in the ocean, $^{234}$U undergoes uniform radioactive decay and produces $^{230}$Th at a constant known rate ($\beta_{230}$) throughout the water column.

$$\begin{aligned} \beta_{230} &= \lambda_{230} \times {}^{234}U \\ &= 9.16 \times 10^{-6} yr^{-1} \times 2910\ dpm\ m^{-3} \\ &= 0.0267\ dpm\ m^{-3} yr^{-1} \end{aligned} \tag{1.2}$$

where $\lambda_{230}$ is decay constant of $^{230}$Th and $^{234}$U is the activity of $^{234}$U in sea water. Equation 1.2 assumes that uranium decay series is in secular equilibrium, i.e., the activity of $^{230}$Th is equal to the activity of the preceding isotopes in the decay series (*Francois et al.*, 2004).

Unlike Uranium, $^{230}$Th is highly insoluble in seawater and has a high affinity for particles, resulting in prompt removal from the water column as it adsorbs to settling particles (*Bacon and Anderson*, 1982). Based on the particle-reactive behavior of $^{230}$Th, *Bacon* (1984) proposed that the flux of scavenged $^{230}$Th to the sea floor ($F_{230}$) is equivalent to its production from $^{234}$U decay in the overlying water column.

$$F_{230}\ (dpm\ m^{-2} yr^{-1}) = \beta_{230} \times z \tag{1.3}$$

where z is the water depth. The $^{230}$Th pool in marine sediments also contains detrital and authigenic $^{230}$Th. Detrital $^{230}$Th is locked in the mineral lattice of terrigenous material, whereas authigenic $^{230}$Th is produced from the decay of authigenic U within the sediment. Thus, the scavenged $^{230}$Th is corrected for both detrital and authigenic contributions to get $^{230}Th_{excess}$ ($^{230}Th_{xs}$). Because of its strong particle affinity, the scavenged $^{230}$Th remains incorporated in the sediment but undergoes radioactive decay after burial ($t_{1/2}$ = 75.58 $\pm$ 0.11 ka, *Cheng et al.*, 2013). The $^{230}Th_{xs}$ should also therefore be corrected for decay since the time of deposition ($^{230}Th_{xs,\,0}$). These calculations are explained in detail in *Francois et al.* (2004). $^{230}Th_{xs,\,0}$ is hereafter referred to as excess $^{230}$Th.

Equation 1.3 indicates that there will be a simple inverse relation between preserved

vertical flux ($F_v$) and the scavenged $^{230}Th_{xs,\,0}$ concentration in marine sediment.

$$^{230}Th_{xs,\,0}\ (dpm\ g^{-1}) = \frac{F_{230}\ (dpm\ m^{-2}yr^{-1})}{F_v\ (g\ m^{-2}yr^{-1})}$$

$$or$$

$$F_v = \frac{\beta_{230}\ * z}{^{230}Th_{xs,\,0}} \tag{1.4}$$

The preserved vertical flux of any component [i] can be written as $F_i$.

$$F_i(g\ m^{-2}yr^{-1}) = F_v\ * f_i \tag{1.5}$$

where, $f_i$ is weight fraction of component [i] in the sediment. This method is thought to give more accurate vertical flux estimates by normalizing the particle flux to excess $^{230}$Th and correcting for lateral flux due to sediment redistribution on the sea floor.

One of the disadvantages of this method, however, is the distribution of $^{230}$Th according to sediment grain size. Clay sized grains (<4 $\mu$m) have a high surface area and thus are likely to contain elevated $^{230}$Th concentrations (*Thomson et al.*, 1993; *Francois et al.*, 2004). *Kretschmer et al.* (2010) found that 50 - 90 % of the total excess $^{230}$Th inventory is concentrated in the fine material (<10 $\mu$m). This "grain size bias" leads to an over-estimation of focusing factors and under-estimation of the actual vertical flux at focused sites due to size fractionation during lateral transport (*Kretschmer et al.*, 2010). *Kretschmer et al.* (2010) also concluded that $^{230}$Th normalization is still a considerable improvement for vertical flux estimates compared to the traditional MAR approach. *McGee et al.* (2010) also examined the size fractionation effect on the Blake Ridge, a drift deposit in the western North Atlantic. They found that despite the enrichment of $^{230}$Th in the fine fraction (<4 $\mu$m), the total $^{230}$Th inventory in bulk sediment is only minimally affected by lateral sediment transport. This is possibly due to the cohesive behavior of fine grains in marine settings, which limits the fractionation of grains finer than 4 $\mu$m from coarser grains during lateral transport (*McGee et al.*, 2010). *Marcantonio et al.* (2014) examined the inventories of $^{230}$Th from winnowed and focused sites at the Cocos and Carnegie Ridges and speculated that the size fractionation occurs most frequently at lower current velocities. These authors also concluded that the $^{230}$Th normalization works well for recording fine grained (detrital and opal) fluxes, but is not effective for coarse grained (carbonate) fluxes

in the regions that have undergone sediment redistribution.

## 1.3 The Focusing Debate

Export fluxes calculated using the traditional MAR and the $^{230}$Th normalization method give divergent results particularly in the equatorial Pacific (e.g., *Paytan et al.*, 1996; *Marcantonio et al.*, 2001; *Loubere et al.*, 2004; *Averty and Paytan*, 2004; *Broecker*, 2008). Traditional MARs suggest large export fluxes (e.g., organic matter) and by inference higher primary productivity during the glacial period compared to the Holocene (*Paytan et al.*, 1996; *Lyle et al.*, 2002; *Broecker*, 2008). However, estimates based on $^{230}$Th normalization show significantly lower export flux (20 - 40 %) and little to no change in production between glacial and interglacial periods in the equatorial Pacific (*Marcantonio et al.*, 2001; *Higgins et al.*, 2002; *Loubere et al.*, 2004; *Anderson et al.*, 2008). The inconsistencies between these two methods have given rise to the "focusing debate" (*Francois et al.*, 2004; *Lyle et al.*, 2005; *Broecker*, 2008).

Studies supporting $^{230}$Th normalization suggest that traditional MARs are influenced by lateral sediment redistribution that occurs in the deep Pacific Ocean, possibly in a systematic climate related fashion. *Suman and Bacon* (1989) quantified syndepositional sediment redistribution using the inventory of excess $^{230}$Th in the sediment by means of the "focusing factor ($\Psi$)". The calculation of the focusing factor is based on the assumption that the inventory of excess $^{230}$Th in the sediment is equal to its production rate in the water column by uranium decay. If there is no sediment redistribution on the sea floor, then the ratio between inventory and production is equal to 1 ($\Psi$ = 1). The inventory of excess $^{230}$Th in the sediment will change if there is addition (focusing) or removal (winnowing) of sediment on the sea floor (*Suman and Bacon*, 1989; *Francois et al.*, 2004). The focusing factor thus quantifies the extent of sediment redistribution on the sea floor. See Section 2.8.6 for details on the calculations and interpretation of focusing factors.

Studies against $^{230}$Th normalization argue that sedimentary evidence does not support widespread sediment redistribution in the equatorial Pacific (*Lyle et al.*, 2005, 2007; *Broecker*, 2008). These studies also suggest horizontal diffusion of dissolved $^{230}$Th in the water column from areas of low particle flux, such as gyres, to areas of high particle flux,

such as the equatorial upwelling region. According to these authors the lateral transport of dissolved $^{230}$Th in the water column and not on the sea floor causes the high accumulation of excess $^{230}$Th, thus biasing the $^{230}$Th normalization method and giving rise to focusing factors $\neq 1$. *Francois et al.* (2007) opposed this mechanism arguing that the low residence time of dissolved $^{230}$Th ($<$4 - 40 yrs) and low residence time of suspended particulates (5 - 10 yrs) limits the lateral transport of $^{230}$Th in the dissolved form as well as attached on suspended particles. *Siddall et al.* (2008) used a circulation model to further challenge the studies by *Lyle et al.* (2007) and *Broecker* (2008) and showed that this effect does not fully explain the high excess $^{230}$Th accumulation in the equatorial Pacific. Similarly, *Singh et al.* (2013) found that the transport of dissolved $^{230}$Th from the Peru Basin into Panama Basin was relatively small and only contributed 15 - 30 % to the total dissolved $^{230}$Th produced within the water column of Panama Basin itself. The lateral export of $^{230}$Th between these two basins could only produce focusing factors of 1.3 and cannot explain focusing factors of $\sim$8 that are found at some sites in Panama Basin (*Kienast et al.*, 2007).

To further examine the issue of sediment focusing an independent proxy is needed. Sediment grain size distribution can be used to help characterize the depositional environment on the sea floor.

## 1.4 Sediment Grain Size Distribution

The disaggregated inorganic grain size (DIGS) distribution is a function of sediment sources, distance from the source regions and the processes affecting sediment transport and deposition (*Kranck*, 1975; *Middleton*, 1976; *Kranck and Milligan*, 1985; *Flemming*, 2007; *Weltje and Prins*, 2007). These processes influence the sediment grains in a characteristic way that results in a distinct frequency distribution. Therefore, grain size parameters like mean size, sorting, and skewness provide information about environmental conditions and different processes affecting the sediment before its deposition (e.g., *Folk and Ward*, 1957; *Middleton*, 1976; *Blott and Pye*, 2001; *Flemming*, 2007). In recent years, different numerical models have been developed to decompose the DIGS distribution according to its subpopulations (*Weltje and Prins*, 2007; *Sun et al.*, 2002; *Dietze et al.*, 2012), which offer more details on sedimentary dynamics and processes.

*Rea and Hovan* (1995) found that the North Pacific abyssal plain shows two distinct grain size distributions. Sediments further away from the coast are dominantly eolian, and sediments closer to the continents are dominantly hemipelagic. Hemipelagic sediments are unsorted and show a fairly flat distributions (Figure 1.1(a)) whereas eolian dominated sediments show a fine mode and very low contributions of larger grains (Figure 1.1(b)). In the equatorial Pacific, the boundary between hemipelagic and eolian sediment is thought to be approximately at 300 km from the continental margin (*Singh et al.*, 2011). Beyond 300 km, the sediments are mostly eolian with a characteristic DIGS distribution exhibiting a well sorted mode between 1 - 5 $\mu$m (*Rea and Hovan*, 1995). The distinct mode smaller than 10 $\mu$m contrasts with marine clays, very fine silt, and fine silts that, because of cohesion among grains, cannot be sorted hydrodynamically (*McCave et al.*, 1995). Thus, a mode in the fine silt range can only represent a sorting process that took place prior to deposition i.e., in the atmosphere. *Prospero and Bonatti* (1969) also found a dust mass peak between 2 - 5 $\mu$m when atmospheric dust in the equatorial Pacific was collected using a mesh. Dust, once it is suspended into the atmosphere, is subjected to gravimetric settling. Thus, as the distance from the source area increases, dust particles are more size sorted and the mean dust grain size decreases. *Prospero* (1999) found that long-range transport of dusts produces a peak in the 2 - 5 $\mu$m size range.

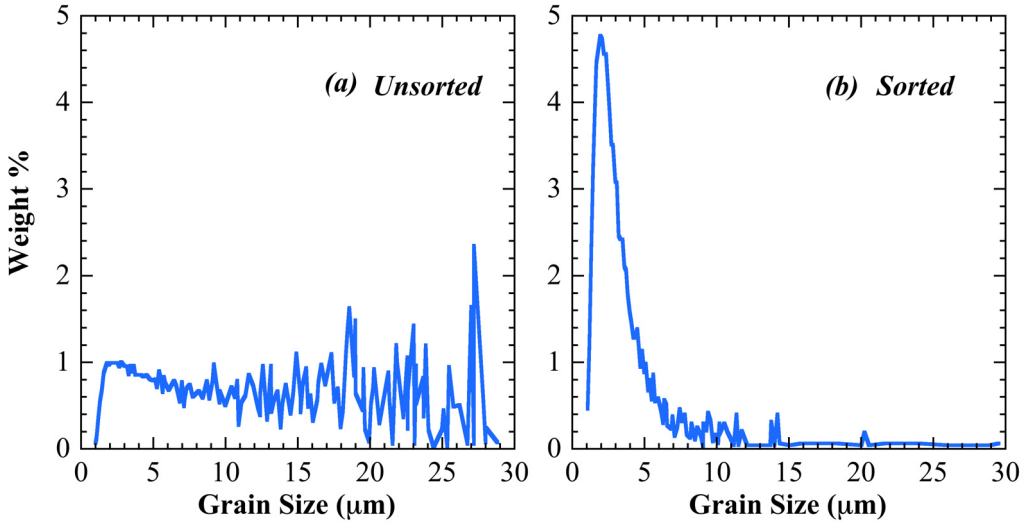


Figure 1.1: Grain size distributions of (a) an unsorted sediment (b) a well sorted sediment. Figures are modified from *Rea and Hovan* (1995): (a) Hemipelagic surface sediment from Gulf of Alaska core Par87-2 and (b) eolian sediment from North Pacific core W8809A-38GC.

Once sediments are deposited on the sea floor, bottom currents can influence the DIGS distribution. These processes mostly affect the grains in the sortable silt size range (10 - 63 $\mu$m) because of the tendency of material finer than 10 $\mu$m to behave cohesively and because of the inability of average deep sea current to move materials coarser than 63 $\mu$m (*Ledbetter*, 1986; *McCave et al.*, 1995; *McCave and Hall*, 2006). Material within the 10 - 63 $\mu$m grain size range responds to hydrodynamic forcing and is size selected according to the bed shear stress (related to current velocity) and settling velocity. The degree of sorting affects the shape of the DIGS distribution in the sortable silt size range (Figure 1.2). Because of size selection during sorting, a better sorted sediment shows a narrower mode. In the deep sea, current induced sorting occurs primarily during resuspension, transport and deposition (*McCave et al.*, 1995). The degree of sorting can thus provide information about the extent of lateral sediment transport on the sea floor.

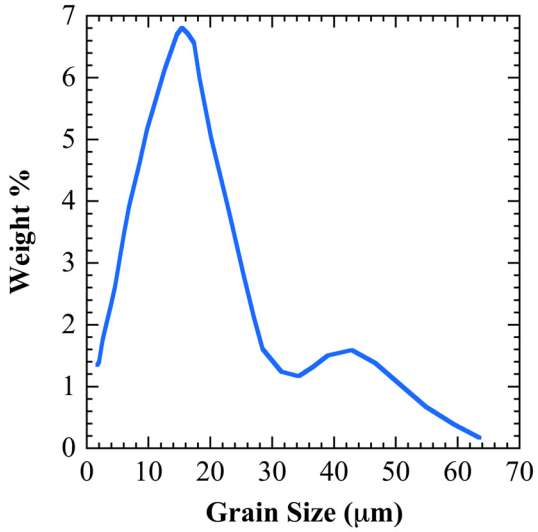


Figure 1.2: Grain size distribution of sediment from the Nova Scotian rise under a strong current (10 - 15 cm $s^{-1}$). Figure modified from *McCave et al.* (1995).

In summary, sediment DIGS distributions can be used as an independent proxy for dust flux estimates and the extent of lateral sediment redistribution.

## 1.5 Marine Authigenic Barite

Sea water is largely undersaturated with respect to barite ($BaSO_4$) which is formed when supersaturation is achieved upon mixing of barium ($Ba^{2+}$) and sulphate ($SO_4{}^{2-}$) ions (*Monnin et al.*, 1999). The formation of barite occurs either by direct biological mediation or inorganic precipitation within supersaturated micro-environments (*Goldberg and Arrhenius*, 1958; *Ganeshram et al.*, 2003; *Griffith and Paytan*, 2012). There are four general modes of barite formation: marine, hydrothermal, diagenetic, and cold seep (*Paytan et al.*, 2002; *Griffith and Paytan*, 2012). Among these modes, marine barite is the only biologically mediated form and most relevant for this thesis because of its size (0.5 - 5 $\mu$m).

*Ganeshram et al.* (2003) looked at laboratory cultured and coastal phytoplankton to investigate the mechanism of marine barite formation. The authors suggested that the enrichment of $Ba^{2+}$ rather than $SO_4{}^{2-}$ in the water column induces barite precipitation. The barium content of many different organisms is considerably higher (2 - 589 ppm, *Fisher et al.*, 1991) than that of sea water (0.005 - 0.028 ppm, *Bishop*, 1990). During organic matter degradation, $Ba^{2+}$ is released, supersaturating the micro-environment around the decaying organic matter with respect to barite. As a result, barite crystals are abundant in sinking and suspended particulate matter. Barite precipitation is thought to occur mainly in the upper water column where most of the organic matter is regenerated, but the recent study by *Van Beek et al.* (2007) has shown that barite precipitation may occur at greater water depths as well. Barite is formed continuously during aggregate degradation and vertical transport, and accumulates in the sediment. Although little research has been done to quantitatively determine the different parameters influencing the preservation of barite (*Schenau et al.*, 2001), *Paytan and Kastner* (1996) found that, at least in productive areas, the fraction of marine barite preserved could reach up to 30 % of the amount of barite arriving at the sea floor. Marine barite crystals are well preserved in oxic sediments because of their low solubility and resistance to diagenetic alteration after burial.

Marine barite crystals range from 0.5 to 5 $\mu$m in size (*Paytan et al.*, 1993, 2002). This is the same size as dust particles (1 - 5 $\mu$m). Thus, the presence of barite is expected to affect, and possibly overwhelm the grain size distribution of deep sea sediments in the $<5$ $\mu$m

size range. The effect of barite crystals on the overall grain size distribution could be particularly pronounced in the central equatorial Pacific, because of the lack of significant inorganic terrestrial sediment sources in this region and the higher accumulation of barite in productive areas.

## 1.6 Significance of the Present Study

The effect of dust on the climate system is still poorly understood or quantified. Global dust models are able to reproduce the overall magnitude and spatial variability of the dust cycle reasonably well, but they are not capable of correctly simulating the impact of changing dust load on climate (*Kohfeld and Harrison*, 2001; *Mahowald et al.*, 2006; *Maher et al.*, 2010; *Albani et al.*, 2014). Understanding past amplitudes, ranges, and time scales of dust fluxes can help towards the development of future climate models that provide insight into the dust cycle and its interaction with other components of the Earth's system. In the equatorial Pacific, in particular, a full understanding of past dust dynamics is lacking. This is largely due to the gap in spatial and temporal resolution of the dust flux estimates in this region.

On the other hand, the equatorial Pacific is one of the most studied areas with respect to paleoproductivity reconstructions because of its contribution to the vertical carbon flux and the biological pump. In recent years, several studies have been conducted to resolve the debate regarding sea floor sediment redistribution which results in inaccurate vertical flux estimations. The validity of the $^{230}$Th normalization method has been questioned based on the behavior of the $^{230}$Th isotope in the water column (*Lyle et al.*, 2005, 2007; *Broecker*, 2008). These studies also oppose the idea of lateral transport of sediment on the equatorial Pacific sea floor.

DIGS is an independent proxy and has never been applied to the question of sediment focusing or to reconstruct dust fluxes in the EEP. The DIGS based dust fluxes provide a different approach to dust flux estimates and at the same time allow comparison of flux records to a different proxy. In doing so, uncertainties regarding the dust fluxes in the equatorial Pacific can be constrained. This will provide more spatially and temporally resolved dust flux estimates in the equatorial Pacific. At the same time, DIGS distributions

can provide an independent approach to investigate sea floor sediment dynamics. DIGS distributions are not influenced by the geochemistry of the sediment like the other proxy ($^{230}$Th) but are driven by hydrodynamic processes. With this approach, the existence and extent of sediment redistribution can be better understood. This can provide further insight into the focusing debate which in turn will help in the validation of the $^{230}$Th normalization method.

Marine authigenic barite has been used as a paleoproductivity proxy (*Paytan et al.*, 1996; *Averty and Paytan*, 2004), however its potential influence on the fine fraction of sediments has not been studied yet. Examining DIGS distributions before and after removal of barite from the sediment provides a unique way to assess the influence of barite crystals on the fine fraction. Particularly in the equatorial Pacific, the influence of barite on the DIGS distribution could be large, resulting in inaccurate dust flux estimates. This thesis will provide a method to gravimetrically separate barite crystals from very small subsamples of marine sediment, which has never been conducted before.

## 1.7 Goals

The overarching goals of this thesis are (1) to reconstruct dust fluxes over the last glacial-interglacial cycle in the equatorial Pacific, and (2) to contribute to the ongoing debate about sediment focusing in the equatorial Pacific with the help of grain size analyses. More specifically, this thesis has the following objectives:

- Reconstruct glacial-interglacial trends of dust deposition in the equatorial Pacific region based on grain size analyses.
- Compare the grain size-based dust fluxes (dust$_{GS}$) with $^{232}$Th-based dust fluxes (dust$_{Th}$) and other existing dust flux records in the literature. This comparison will assess the use of DIGS as a dust flux proxy.
- Examine the sediments for evidence of bottom current induced size sorting. This will help to confirm (or reject) the influence of syndepositional sediment redistribution in the Pacific.

- Develop a separation technique to remove barite crystals from a small volume of marine sediment using heavy density fluids. This is envisioned as a first step to assess the potential bias of barite on dust flux reconstructions using grain size.

# CHAPTER 2

# METHODOLOGY

## 2.1 Core Material

Three cores from the eastern equatorial Pacific (EEP) and one core from the central equatorial Pacific were studied for this project (Figure 2.1). Core TR163-19 (hereafter referred to as TR-19) was recovered during cruise 163 aboard R/V Trident in 1975 from 2348 m water depth in the EEP. Sediment cores ME0005A-24JC (hereafter referred to as ME-24) and ME0005A-27JC (hereafter referred to as ME-27) were recovered from water depths of 2941 m and 2203 m, respectively, in the EEP during the ME0005A expedition aboard the R/V Melville in 2000. Core TTN013-PC72 (hereafter referred to as PC-72) lies on the equator in the central Pacific. It was recovered from a water depth of 4298 m in 1992 during the US Joint Global Ocean Flux Study (JGOFS) equatorial Pacific Process Study at $\sim$140° W. The geographical coordinates of all core sites are provided in Table 2.1.

Table 2.1: Core locations, water depths and distance from the continental margin.

| **Core ID** | **Latitude** | **Longitude** | **Water depth (m)** | **Approx. distance offshore (km)** |
|---|---|---|---|---|
| TR163-19P | 2° 15.5' N | 90° 57.1' W | 2348 m | 1250 km |
| ME0005A-24JC | 0° 01.302' N | 86° 27.788' W | 2941 m | 600 km |
| ME0005A-27JC | 1° 51.201' S | 82° 47.20' W | 2203 m | 155 km |
| TTN013-PC72 | 0° 06.8' N | 139° 24.1' W | 4298 m | 6553 km |

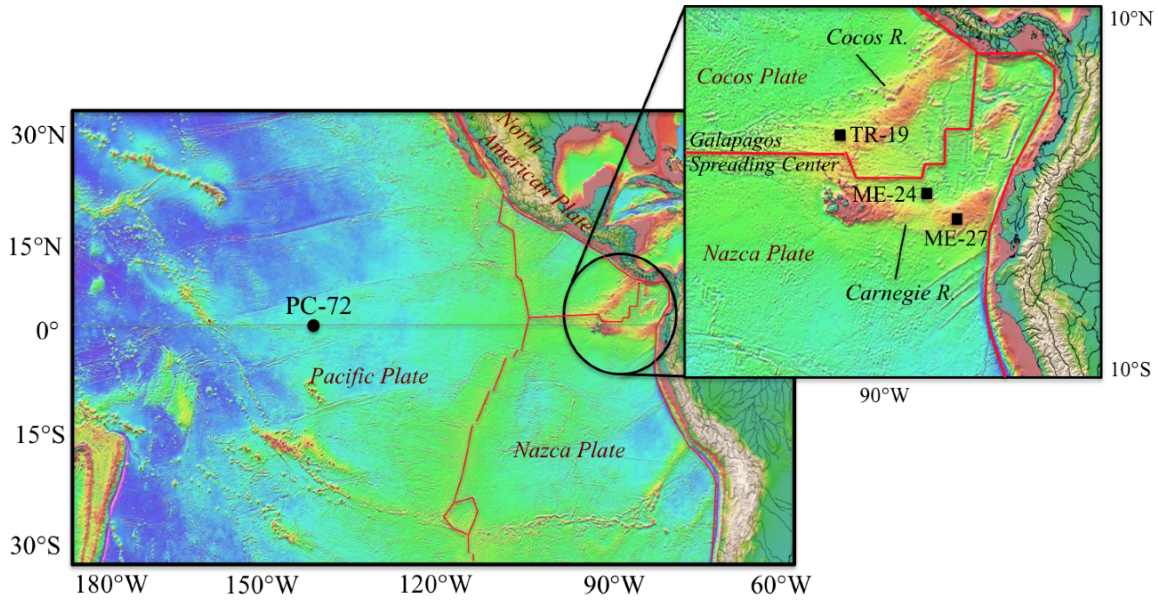


Figure 2.1: Map of the core site (a) TTN013-PC72, (b) eastern equatorial Pacific (EEP) region showing cores TR163-19P, ME0005A-24JC and ME0005A-27JC. Bathymetry from *Smith and Sandwell* (1997) *(http://topex.ucsd.edu/marine_topo/mar_topo.html).*

## 2.2 Study Area

Geologically, the fundamental tectonic process in the equatorial Pacific is spreading along the East Pacific Rise that defines four major plates: North American, Pacific, Cocos and Nazca plate (*Van Andel et al.*, 1975). The spreading of the Cocos and Nazca plate 27 to 8 Ma B.P.[1] formed the Panama Basin (*Longsdale and Klitgord*, 1978). The basin is enclosed by the continental shelves of Panama, Columbia, and Ecuador in the east and by the now inactive Cocos and Carnegie Ridges in the northwest and south, respectively. TR-19 lies on the outer flank of the Cocos Ridge. Core ME-27 lies on the southern side of the Carnegie Ridge, which forms the southern boundary of the basin, whereas core ME-24 lies within the basin at the foot of the Carnegie Ridge. Both the Cocos and Carnegie Ridges rise over 1000 m above the surrounding sea floor (*Moore Jr. et al.*, 1973). Within the basin, the Coiba and Malpelo Ridges separate the Panama basin into a deeper eastern basin (east of 83° W) dominated by terrigenic debris from the continent shelves and a western basin (west of 83° W) dominated by pelagic biogenic sediments (*Moore Jr. et al.*, 1973). Within the western basin, the Cocos and Nazca plates are separated by the active Galapagos

[1]Ma B.P. = Million years before present.

spreading zone that provides hydrothermal input to the surrounding area. Among the three EEP cores, ME-24 is mostly affected by hydrothermal input since this site is approximately 50 nautical miles south of the spreading center (*Kienast et al.*, 2007). Contrary to the EEP cores, the central Pacific core PC-72 is removed from any significant hemipelagic as well as hydrothermal inputs.

The equatorial Pacific is a key area for the study of present and past global biogeochemical cycles. It forms a boundary between the northern and southern tropical gyres and hosts complex current systems. The major currents in this region are shown in Figure 2.2. The westward flowing North Equatorial Current (NEC) marks the boundary of the North Pacific Gyre, and lies north of the equator. The South Equatorial Current (SEC), which marks the boundary of the South Pacific Gyre flows westward slightly north of the equator. The North Equatorial Counter Current (NECC) acts as a boundary between the NEC and SEC at the surface (Figure 2.2(a)).

The entire region is affected by wind driven upwelling along the equatorial divergence zone and off the coast of South America. Upwelling brings cooler and nutrient rich water from the eastward flowing Equatorial Undercurrent (EUC) to the surface. *Toggweiler and Carson* (1995) separated the EUC into two vertical components: upper EUC (roughly between 100 and 250 m) and lower EUC (roughly between 220 and 290 m) (*Dugdale et al.*, 2002). The lower EUC water flows eastward without upwelling until it reaches the Galapagos Islands, where it splits into northward and southward branches. The northward branch becomes the California Undercurrent (CUC) whereas the southward branch enters the Peru-Chile Undercurrent (PCUC; Figure 2.2(b)). Meridional wind driven upwelling along the coasts of Peru and Ecuador brings the cold nutrient rich PCUC water back to the surface as the Peru Current (PC). The PC is then transported westward along with the SEC forming a cold tongue (*Toggweiler et al.*, 1991; *Toggweiler and Carson*, 1995; *Dugdale et al.*, 2002). Core ME-27 is mostly affected by this highly productive water.

The upper EUC is the source water for upwelling along the equatorial divergence zone. In comparison to the lower EUC, the upper EUC water has slightly higher temperature and lower nutrient content (*Dugdale et al.*, 2002). All three EEP sites experience intensive productivity because of upwelling of nutrient rich EUC water. However, the magnitude of productivity varies according to the source of the upwelled water. Site ME-27 experiences

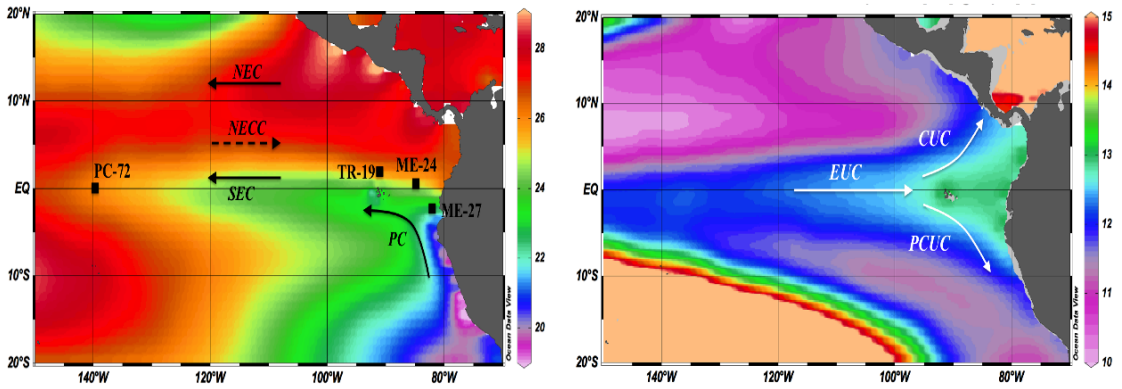


(a) Surface temperature (°C)

(b) Temperature at 200 m water depth (°C)

Figure 2.2: Map of present day annual temperature at 200 m water depth and sea surface, derived from WOA09 (*Locarnini et al.*, 2010). White arrows indicate undercurrents: Equatorial Undercurrent (EUC), California Undercurrent (CUC), and Peru-Chile Undercurrent (PCUC). Black arrows indicate surface currents: North Equatorial Current (NEC), North Equatorial Counter Current (NECC), South Equatorial Current (SEC), and Peru Current (PC). Black boxes show the core sites.

upwelling of the lower EUC via the PC and thus has the highest productivity $\sim$600 gC m$^{-2}$ yr$^{-1}$ (*Gregg et al.*, 2003). Site ME-24 lies within the upwelling region of the equatorial divergence zone and TR-19 beneath the northern boundary of the upwelling region. These sites experience upwelling of the upper EUC water and have productivity of $\sim$350 and $\sim$150 gC m$^{-2}$ yr$^{-1}$, respectively (*Gregg et al.*, 2003). Further west along the equator, site PC-72 lies just outside of the SEC cold tongue. Nevertheless, the central Pacific region also experiences relatively high productivity ($\sim$200 gC m$^{-2}$ yr$^{-1}$; *Gregg et al.*, 2003) due to upwelling of the upper EUC along the equatorial divergence zone. The deposition at all four sites is dominated by calcareous sediments (*Dubois et al.*, 2011, Supplimentary data).

## 2.3 Core Chronologies

The age models of the three EEP cores are adopted from *Dubois et al.* (2011). For core ME-24, *Dubois et al.* (2011) presents an updated age model for Marine Isotopic Stage 1 and 2 (MIS1 and MIS2) based on 6 radiocarbon dates on *Neogloboquadrina dutertrei*. The radiocarbon dates were calibrated to calendar dates using the calibration software CALIB 6.0 (deltaR = 167$\pm$106 yr) and the MARINE09 calibration data set (*Dubois et al.*, 2011).

Age models for MIS1 and MIS2 in cores ME-27 and TR-19 were previously published by *Kienast et al.* (2007) and were later updated by *Dubois et al.* (2011). For core ME-27, 4 radiocarbon dates on *N. dutertrei* were used to calibrate calendar ages. The age model of TR-19 is based on planktonic $\delta^{18}$O stratigraphy augmented by 2 radiocarbon measurements (*Kienast et al.*, 2007, and references therein). For the time interval prior to 25 ka[2], the age models of all three cores, ME-24, ME-27, and TR-19, are based on graphical correlation to the high resolution $\delta^{18}O_{ice}$ EPICA record in Antarctica (for more details, see *Dubois et al.*, 2011).

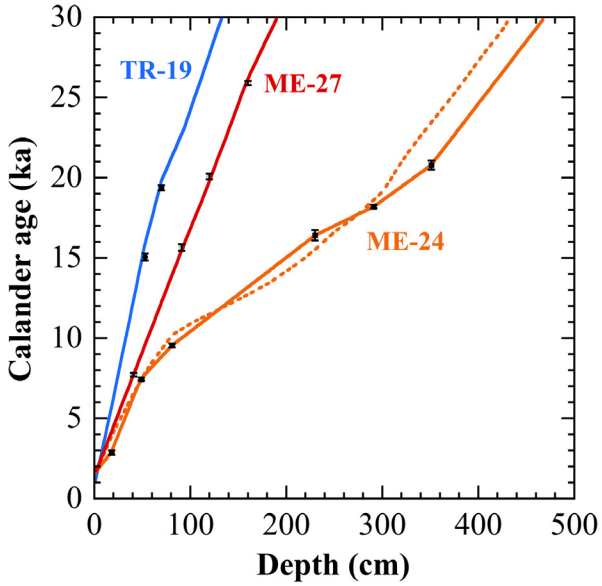


Figure 2.3: Depth-age relationship for three EEP cores (solid lines). The markers on the lines are radiocarbon dates with respective error bars. Orange dotted line shows the previously used chronology for ME-24 (*Kienast et al.*, 2007).

The chronology of the central Pacific core PC-72 is adopted from *Winckler et al.* (2008). This age model was determined by correlating $\delta^{18}$O of benthic foraminifera (*Murray et al.*, 1995, 2000) to a global stack of 57 benthic oxygen isotope records (*Lisiecki and Raymo*, 2005) and includes additional $^{14}$C dates for the upper 100 cm of the core provided by *Anderson et al.* (2008). The age model presented by *Winckler et al.* (2008) was also used by *Hayes et al.* (2011).

[2] 1 ka = 1000 years

## 2.4 Pretreatment and Grain Size Analysis

### 2.4.1 Sample Selection

The samples for the EEP cores were selected to encompass the Holocene and the Last Glacial Maximum (LGM). Samples were selected at depths containing enough material for replicates.

For the central Pacific core PC-72, a few sample depths were selected to examine the last two glacial-interglacial (G-IG) cycles. Core samples exist at 5 cm depth intervals at Dalhousie University. Thus, interglacial and glacial samples were selected based on their proximity to the depths containing the lowest and the highest $\delta^{18}$O values within the two chosen G-IG cycles. Additionally, some samples were selected at depths between the lowest and the highest $\delta^{18}$O values to represent the transition periods. Note that the temporal resolution is lower in the central Pacific core compared to the EEP cores.

### 2.4.2 Removal of Organic Carbon, Carbonate and Biogenic Opal

All sediment samples were pretreated to remove carbonate, biogenic opal and total organic matter as suggested by *McCave et al.* (1995). The samples were freeze dried for three days. For core TR-19, 60 mg subsamples were placed in test tubes for further treatment. Because of the high carbonate content in core PC-72, 0.5 g of sample material was used. First, hydrogen peroxide (10%, ACS grade) and hydrochloric acid (10%, ACS grade) were added to the samples to remove organic carbon and carbonate ($CaCO_3$), respectively. For core TR-19, 4 ml hydrogen peroxide and 4 ml hydrochloric acid was used. Depending on the concentration of organic matter and carbonate, volume of hydrogen peroxide and hydrochloric acid was increased to $\sim$10 - 20 ml and $\sim$10 ml, respectively for PC-72. The samples were rinsed with 20 ml of distilled water and centrifuged for 20 min at 4000 RPM. After carefully decanting the solution, the samples were dried overnight at 65°C. Following the procedure outlined by *Mortlock and Froelich* (1989), the samples were then treated with 2M Sodium carbonate ($Na_2CO_3$) and placed in a water bath at 85°C for 5 hours to dissolve biogenic opal. After 2 and again after 4 hours in the hot bath, the samples were taken out and sonicated for 2 minutes. At the end of the 5 hour period, the

samples were centrifuged for 20 min at 4000 RPM. After carefully decanting the $Na_2CO_3$ solution, which contains dissolved biogenic silica, the samples were rinsed with 40 ml distilled water and centrifuged again for 15 min at 4000 RPM. The rinsing procedure was repeated three times to ensure that all the $Na_2CO_3$ solution was removed from the residual sediment. The disaggregated inorganic grain size (DIGS) distribution of the sample was then determined using a Coulter Counter Multisizer III (Section 2.4.4).

### 2.4.3 Removal of Biogenic Barite

Marine barite crystals have the same size as dust particles (1 - 5 $\mu$m, *Paytan et al.*, 1993, 2002). The presence of barite is therefore expected to affect, and possibly overwhelm the grain size distribution of the deep sea sediment in the less than 10 $\mu$m size range. To understand the effect of marine barite on the grain size distribution of deep sea sediment, a new method of barite separation was developed in this thesis.

Barite crystals present in the sediment are expected to have a high density (4490 kg $m^{-3}$) compared to the siliciclastic sediment fraction (2650 kg $m^{-3}$). Because of their density difference, the barite crystals and siliciclastic sediments can be separated gravimetrically using a heavy density liquid. Heavy density liquids are usually three times heavier than water and are thus used for separating materials of different densities by their buoyancy. In this study, a Sodium Polytungstate (SPT) solution was used as a heavy density liquid because of its compatibility with the membrane filter (Mixed Cellulose Esters (MCE), Millipore®) that was used during filtration. SPT is a user friendly inorganic salt with low volatility and toxicity. It is soluble in water and the density of the SPT solution can be regulated between 1000 and 3100 kg $m^{-3}$. The SPT crystals were first dissolved in distilled water, and the required density was achieved by evaporating the water from the solution using a hot plate (Figure 2.4). A quartz crystal (density 2650 kg $m^{-3}$) was used to determine the density of the solution. The quartz crystal, when dropped into the SPT solution, quickly floats back to the surface as the density of the solution becomes greater than 2650 kg $m^{-3}$. The hot plate was turned off when the surface of the solution started to recrystalize. Though the absolute density at this point is unknown, for calculation purposes, 2890 kg $m^{-3}$ was used as the density of the SPT solution. This value was provided by the manufacturer as nominal density for the SPT solution at 25°C (*GeoLiquids*, 2012).

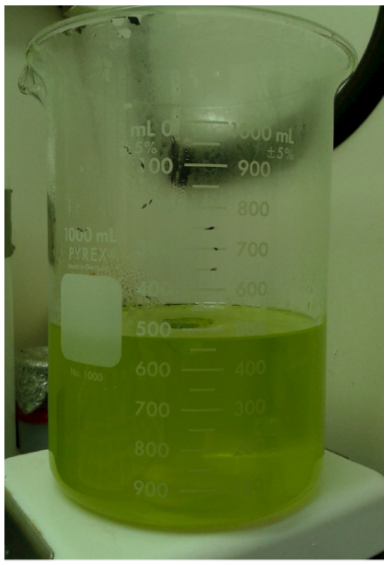


Figure 2.4: Sodium Polytungstate (SPT) solution during evaporation.

A set of subsamples from core PC-72 was treated according to the barite separation method before DIGS analyses were conducted. After the removal of biogenic material, the samples were dried in the oven at 65°C until only a very small amount of water remained in the test tubes. Allowing the sediment to remain slightly wet made subsequent sonification easier. 10 ml of SPT was then added to the test tubes and the samples were sonicated for 15 minutes. An additional volume of 30 ml of SPT solution was added and the samples were sonicated for 15 more minutes. The aim of the repeated sonification was to allow for complete particle disaggregation, so that even the smallest particles with different densities could be separated by the SPT solution according to their buoyancy.

When suspended into the SPT solution, the barite crystals are expected to gravimetrically settle to the bottom of the test tube. Based on Stokes' law, the settling velocity of a barite particle of 2 $\mu$m size suspended in SPT solution is $1.34 \times 10^{-7}$ m s$^{-1}$ (Equation A.2). If allowed to settle gravimetrically, a particle of that size would take about a week to settle to the bottom of the test tube. Because of this long settling time, the samples mixed with SPT solution were centrifuged at 4000 RPM for 10 minutes to speed up the settling process (Equation A.3). Centrifugation allows the barite crystals, along with other particles with a density $>$2890 kg m$^{-3}$, to sink to the bottom of the test tubes and leaves an isopycnic layer of siliciclastic sediment at subsurface (Figure 2.5).

Following centrifugation, the test tubes were dipped into liquid nitrogen (-196°C) so

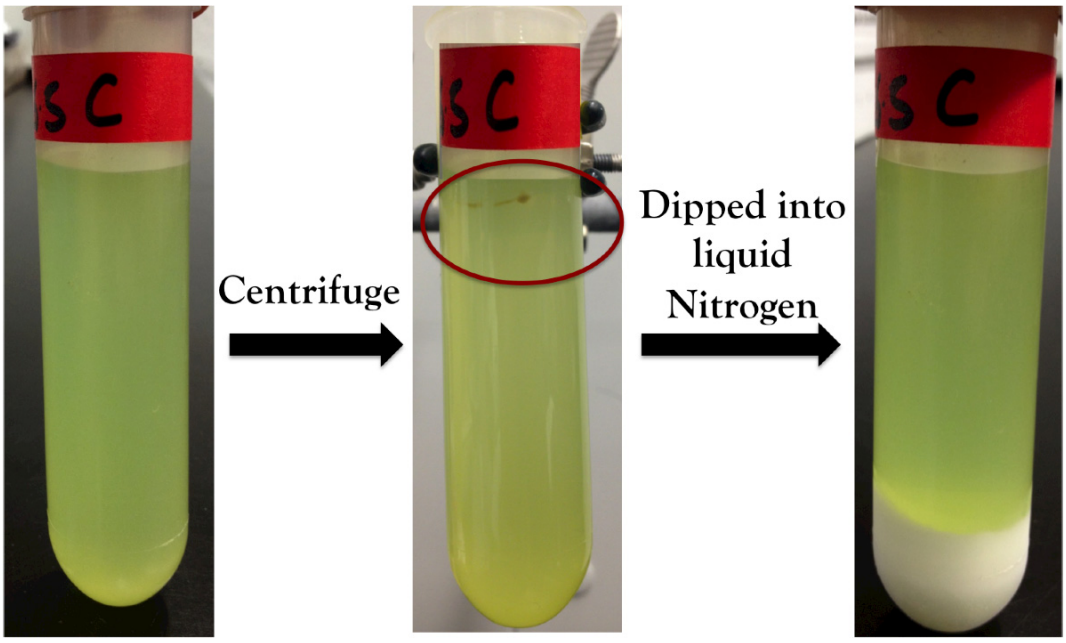


Figure 2.5: The sediment samples in SPT solution after each step in the "Barite Separation" procedure. The first picture shows the test tube containing samples suspended in SPT solution. The middle picture shows the isopycnic layer of silisiclastic sediment (inside the red circle) after centrifugation. The last picture shows the frozen bottom part of the test tube after it was dipped in liquid nitrogen.

that the bottom half of the tube content froze. The upper, unfrozen part of the SPT was then decanted and filtered through a 0.8 $\mu$m pore size membrane filter using vacuum to retain only the siliciclastic sediment. The filter membranes were rinsed several times using distilled water to remove all traces of SPT solution. The sediment covered filters were then ashed overnight (12 hours) at Bedford Institute of Oceanography (BIO) using a low-temperature gas plasma asher. The plasma asher uses oxygen, compressed air and microwaves to combust the filter membranes leaving only the unaltered sediment behind.

The frozen bottom part of the test tube containing barite, and possibly other heavy particles, was thawed and then filtered through a 0.8 $\mu$m pore size membrane filter using vacuum. The heavy material from all the depths was collected onto a single filter membrane which was then used for scanning electron microscope (SEM) analysis (Section 2.6).

### 2.4.4 Disaggregated Inorganic Grain Size Distributions

Disaggregated inorganic grain size (DIGS) distributions were obtained using a Beckman Coulter Counter Multisizer III following a procedure similar to the one described by *Milligan and Kranck* (1991). The sediment samples were first resuspended in an electrolyte solution and then disaggregated using an ultrasonic probe immediately prior to grain size analysis. For this study, 0.45 $\mu$m filtered NaCl (1%) solution was used as an electrolyte. In the Coulter Counter, suspended particles are drawn through an aperture across which a constant electrical current is maintained using two electrodes, one on either side of the aperture tube. In this study, two aperture tubes (diameter 200 $\mu$m and 30 $\mu$m) were used. To prevent the clogging of the aperture tubes, suspended samples were screened through 20 $\mu$m and 100$\mu$m sieves.

The Coulter Counter is based on the principle that a particle passing through an electric field in an electrolyte will cause a voltage impedance proportional to the particle volume. In principle, the detection window is 2 - 60 % of the aperture diameter, thus particles between 0.6 - 120 $\mu$m diameter could be resolved using the 30 $\mu$m and 200 $\mu$m aperture tubes. The data obtained from each tube were merged and normalized using a custom-written Matlab code that generates grain size distributions over the range of 1 - 100 $\mu$m (code available at *https://github.com/JessCG/MS3*).

DIGS distributions for core ME-27 and ME-24 were provided by Dr. Stephanie Kienast (unpublished). Organic carbon, carbonate, and opal were removed from these two cores prior to DIGS analysis following the same method as described in Section (2.4.2). DIGS distributions were obtained using a 30 $\mu$m and a 200 $\mu$m aperture tube on the Multisizer III and merged using the Matlab code described above.

## 2.5 Internal Laboratory Standards

The reproducibility of the grain size distributions as well as the analytical error of the instrument was determined by using a poorly sorted glacial sediment collected in Sillikers, New Brunswick. This standard is referred to as “Sillikers” and has a characteristic grain size distribution. Sillikers were run everyday the Coulter Counter was used to examine

instrument error.

Sediment samples underwent several chemical treatments before DIGS distributions were obtained. To quantify the variability associated with the removal of biogenic material (procedural error), two internal laboratory standards were created in this study. These standards were used to validate the reproducibility of the DIGS distributions after treatments.

The internal marine sediment standards were created by mixing 3 depths of core ME-27. Sediments from 116, 118 and 119.5 cm were mixed together to form Standard-1 (Std-1). Since these three depths have low opal content ($\sim$8 %), Std-1 is considered to be representative of the sediment samples containing low weight % of opal. Similarly, sediments containing high opal content ($\sim$35 %) from 281.5, 284.5, and 287.5 cm depth were mixed together to form Standard-2 (Std-2). A large batch of these internal standards underwent the biogenic removal procedure (Section 2.4.2) and DIGS distribution were obtained.

A subsample from both Std-1 and Std-2 was always treated along with the core samples. The reproducibility of the DIGS distribution of these standards was observed to quantify the procedural error. The analytical error was quantified by the reproducibility of Sillikers runs.

### 2.5.1 Results from Sillikers

The mean modal grain size of Sillikers (n = 23) is 9.19 $\mu$m. Standard deviations in the individual Coulter Counter size bins range from 0.12 to 0.44 vol % (Figure 2.6). *DeGelleke et al.* (2013) obtained similar results for Sillikers (n = 14) and found a mode of 10.56 $\mu$m and standard deviations in the individual size bins ranging from 0.11 % to 0.39 %. The errors in different size fractions (1 - 5, 1 - 10, 10 - 63 $\mu$m; as described in Table 2.2) were quantified by averaging the volume concentration within the size class and obtaining 1$\sigma$ range about the average. The standard deviations in the different size fractions are 0.82, 0.91, and 1.05 % for the 1 - 5, 1 - 10, and 10 - 63 $\mu$m fractions, respectively (Figure 2.6, bottom panel).

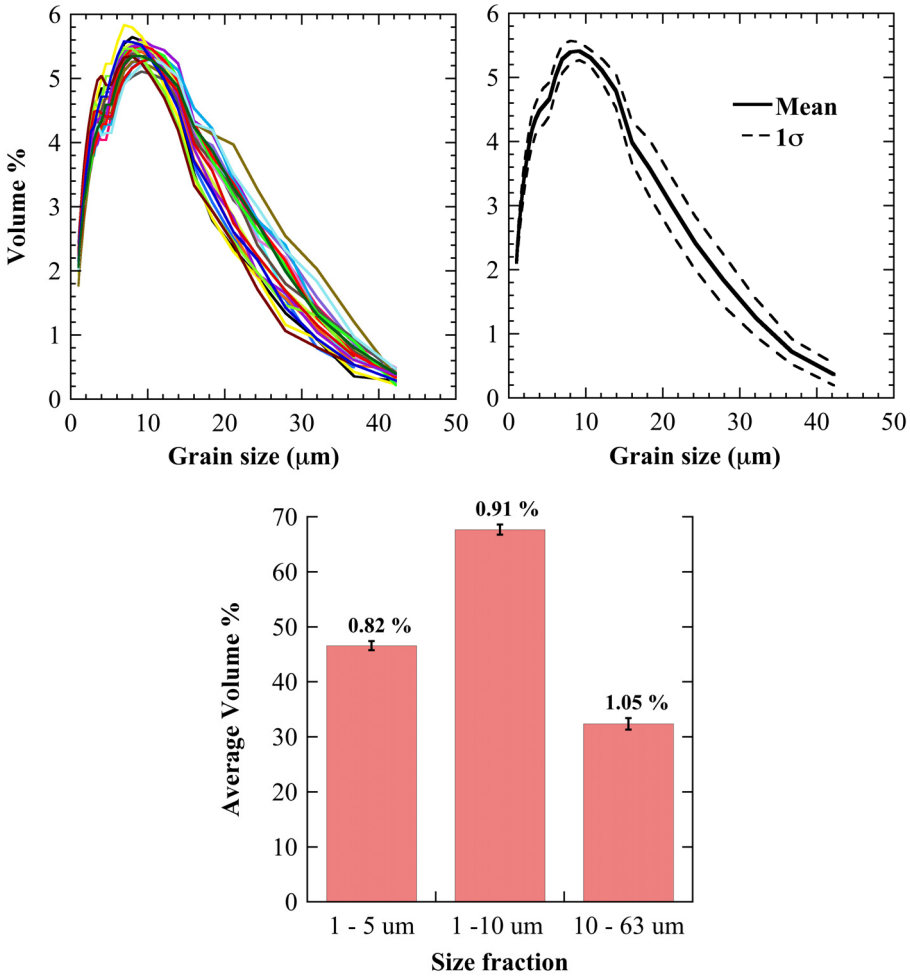


Figure 2.6: Top left panel: 23 replicates of Sillikers DIGS distributions. Top right panel: a mean DIGS distribution (solid black line) with $1\sigma$ (dashed black lines). Bottom panel: Average volume % and standard deviation within different size fractions. Standard deviation values are used to quantify the analytical error of the instrument.

### 2.5.2 Results from Internal Standards

The DIGS distributions show good reproducibility (Figure 2.7, top panel) with standard deviations in individual size bins ranging from 0.13 - 0.48 vol % (Figure 2.7, middle panel). The standard deviations in different size fractions relevant to this study are shown in the bottom panel of Figure 2.7 and represent error associated with pretreatment of the grain size for biogenic removal. These values are only slightly greater (for the 1 - 5 and 1 - 10 $\mu$m fractions) than the standard deviations from Sillikers run, which only provides the instrumental error. Because the study cores contain similar opal concentration as Std-1,

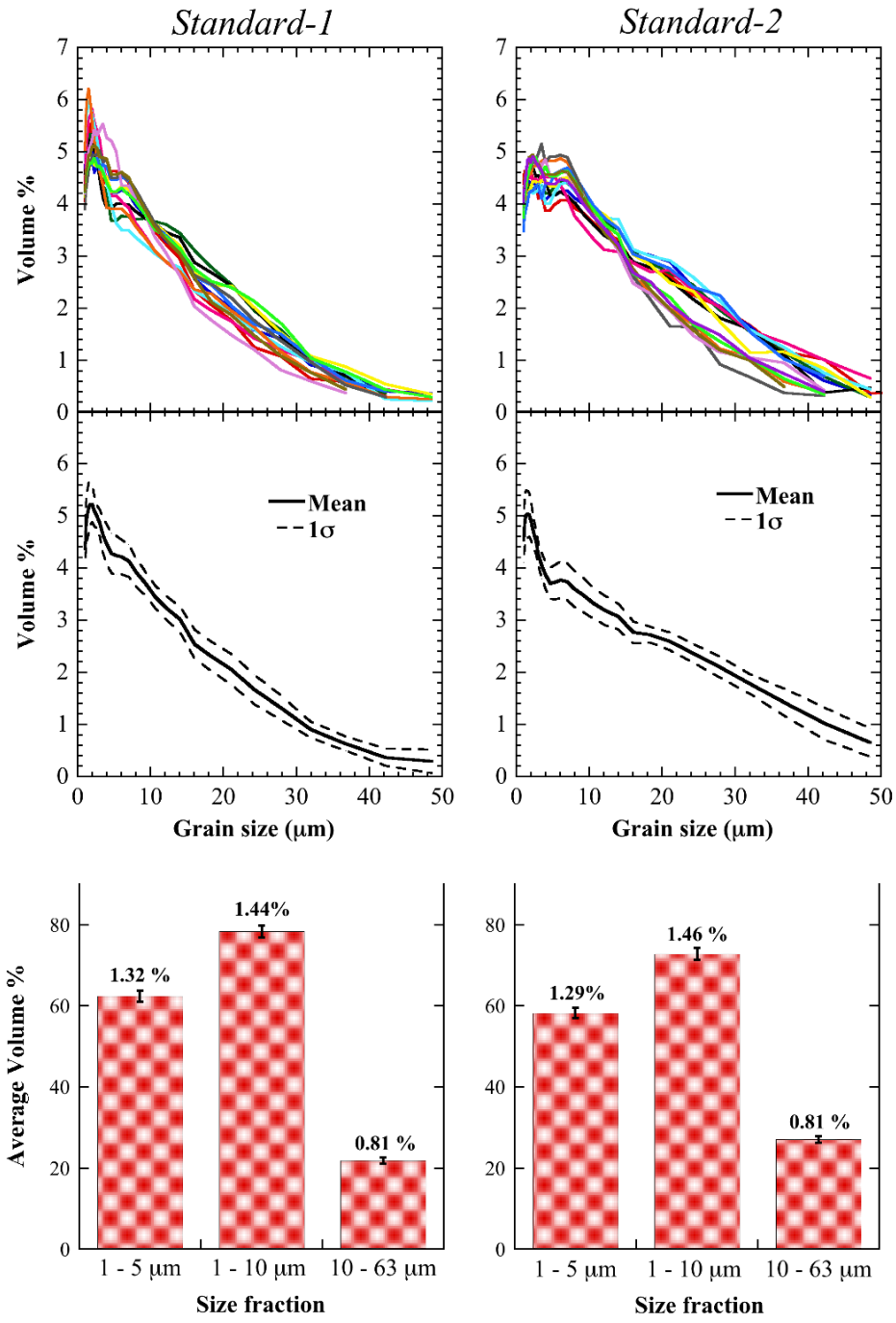


Figure 2.7: Top panel: 13 replicates of DIGS distributions of two lab standards, Std-1 and Std-2, after the removal of biogenic materials. Middle panel: mean DIGS distributions (solid black lines) for Std-1 and Std-2 with $1\sigma$ (dashed black lines). Bottom panel: Average volume % and standard deviation within different size fractions for Std-1 and Std-2. Standard deviation values are used to quantify the procedural error.

the standard deviations in different size fractions for the Std-1 are used as the procedural error as they include both treatment as well as instrumental error.

## 2.6 Scanning Electron Microscope Imaging

Scanning electron microscope (SEM) images were taken of selected samples to visually examine the sediment after the various pre-treatments. Images were taken of bulk sediment, carbonate free sediment, and carbonate and opal free sediment of Std-1, Std-2, ME-27 (118 cm), and PC-72 (20 and 40 cm). For PC-72, images were also taken for selected samples after the barite removal.

The sediment samples were first coated with a thin layer (10 nm) of gold/palladium alloy to prevent electrostatic charging during SEM imaging. The conductive coating was applied in the Scientific Imaging Suite (SIS) located in the Department of Biology at Dalhousie University. The SEM images of Std-1, Std-2 and ME-27 (118 cm) were taken at the SIS. The SEM images of core PC-72 (20 and 40 cm) were taken at the SEM-FIB facility located on Sexton campus at Dalhousie University following the same procedure.

### Results from SEM Imaging

Examples of the SEM images after various pretreatments of the samples are shown in Figures 2.8, 2.9, and 2.10. These images are of PC-72 samples. SEM images of Std-1, Std-2 and ME-27 (118cm) are presented in Appendix B.

Prior to treatment, the bulk samples contained diatoms, radiolarians, and carbonaceous shells of foraminifera and coccolithophores (Figure 2.8). After treatment with HCl, no carbonate shells are seen in the images. Even for the central Pacific core PC-72, which has a very high carbonate content (80 - 90 wt %; *Murray et al.*, 1995), the removal of carbonate using HCl was successful (Figure 2.9). After opal removal, no diatoms or radiolaria are visible (Figure 2.10). Collectively, these images indicate that the pretreatment procedures for the removing of carbonate, opal and organic matter (Section 2.4.2) were successful.

The SEM images of PC-72, which underwent barite removal (Section 2.4.3), show small ($\sim$5 $\mu$m) platy particles, which are interpreted as clays (Figure 2.11). The images

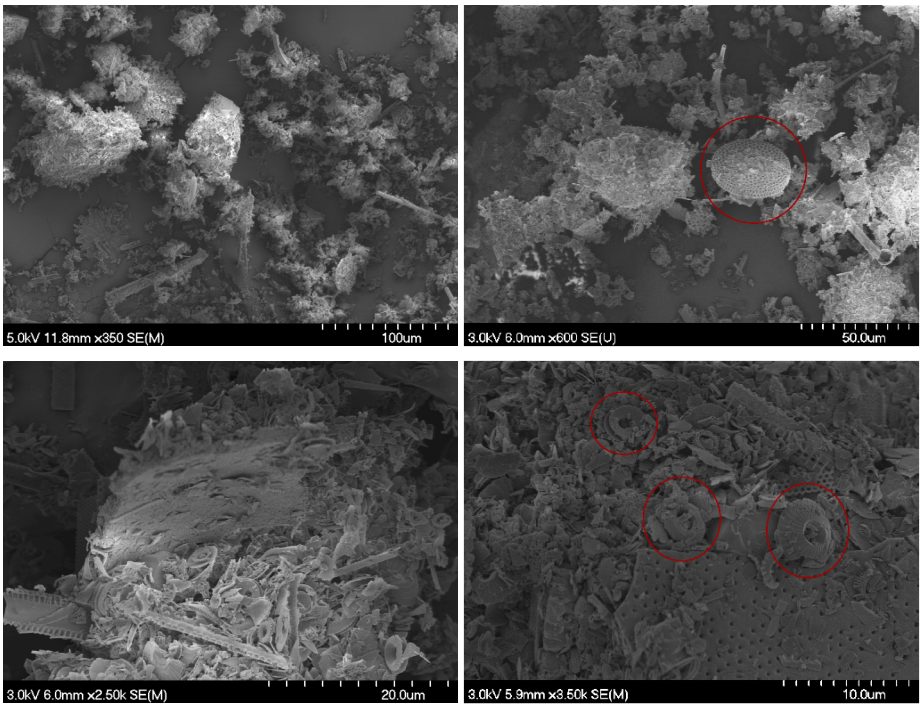


Figure 2.8: SEM images of the freeze dried bulk sediment at different magnifications.

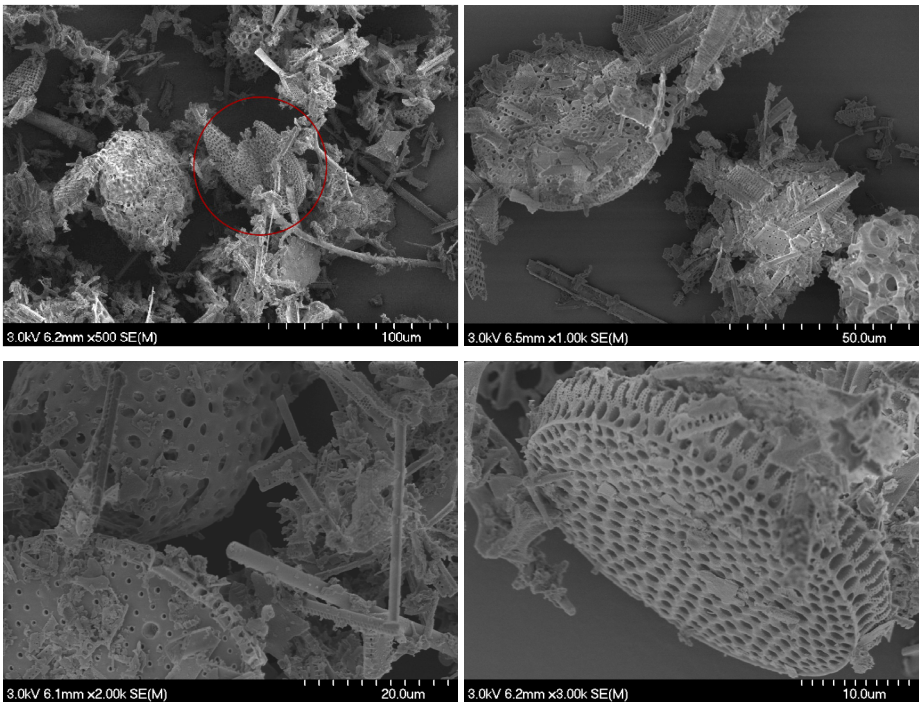


Figure 2.9: SEM images of a sample from which organic carbon and carbonate have been removed. The images are taken at different magnifications.

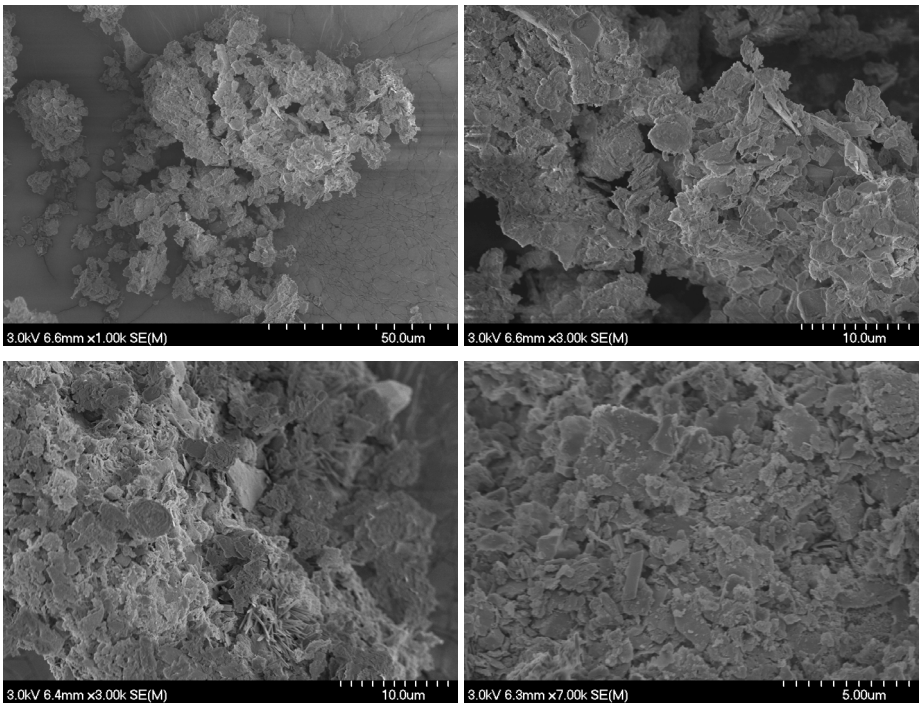


Figure 2.10: SEM images of a sample from which organic carbon, carbonate and opal have been removed. The images are taken at different magnifications.

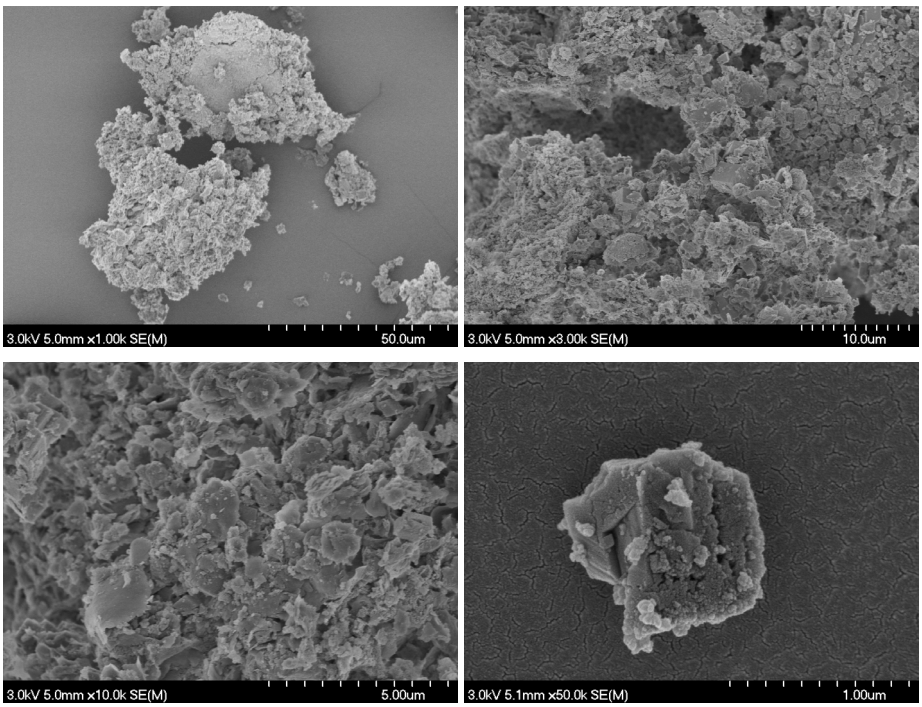


Figure 2.11: SEM images of a sample after the removal of organic carbon, carbonate, opal and marine barite at different magnifications.

reveal that there was no visible change in sediment composition before (Figure 2.10) and after barite removal (Figure 2.11). Figure 2.12 shows the SEM images of the removed dense fraction of the sediment. Irregularly-shaped grains highlighted in Figure 2.12 are assumed to be barite crystals. The size of the particles seen on these images (2 - 5 $\mu$m) is consistent with that of marine barite presented in Figure 1 of *Paytan et al.* (1993). However, it was difficult to clearly identify the barite crystals because of the presence of other materials. This might be because the samples cannot be disaggregated prior to SEM imaging, hence they show particles in an aggregated state. Also, materials that are denser than 2890 kg m$^{-3}$ would have settled along with barite crystals.

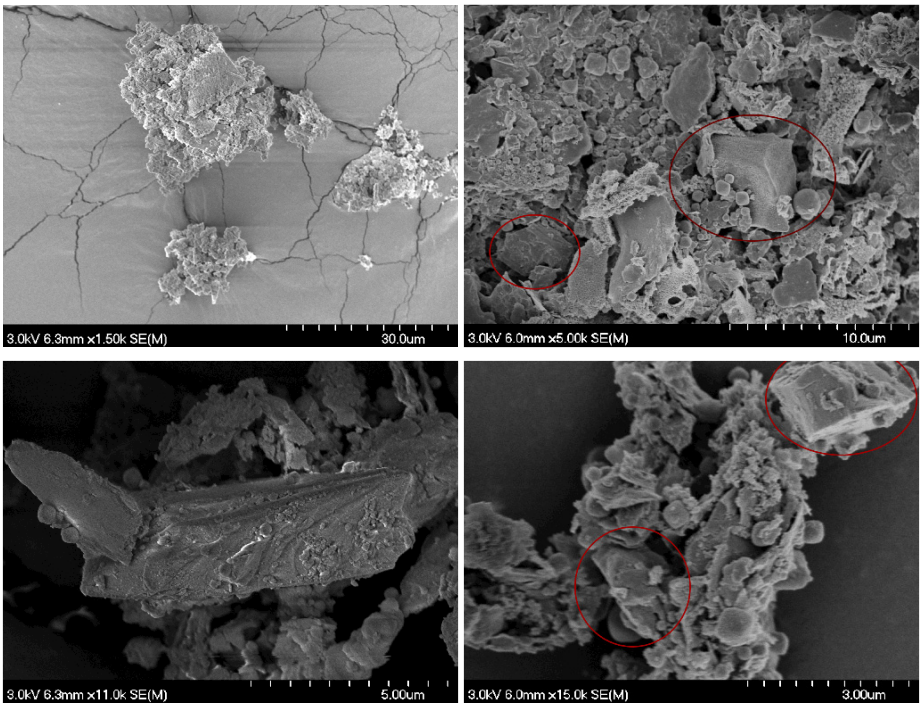


Figure 2.12: SEM images of the "removed barite" at different magnifications.

## 2.7 Grain Size End Member Modeling

Sediment source and sorting during transport combine to produce a characteristic grain size distribution. The distribution follows a unimodal curve for a single sedimentary component. When a bulk sediment contains more than one component, the distribution of the sediment exhibits a polymodal distribution, where each mode reflects different sources

and sorting histories. Empirically, these modes can be isolated from each other as different end members where each end member has its own distinct size distribution.

In this study, the Weibull distribution function was used to determine different end members in the sediment. Weibull distributions are asymmetrical, unimodal probability density functions, given by

$$W_n = \frac{\kappa_n}{\lambda_n} \left(\frac{x_n}{\lambda_n}\right)^{\kappa_n - 1} e^{-(x/\lambda_n)^{\kappa_n}} \tag{2.1}$$

where $\kappa_n$ is a shape parameter determining the width of the distribution, $\lambda_n$ is the scale parameter determining the modal value of the distribution, and $x$ is the grain size. Studies have shown that the Weibull distribution provides a good fit to the grain size distributions of eolian and loess deposits (*Zobeck et al.*, 1999; *Sun et al.*, 2002; *Sun*, 2004). In this study, three end members were used with $\kappa$ varying between 1 to 3 and $\lambda$ varying between 1 to 40. The model grain size distribution of a given sample was obtained as

$$Model = c_1 W_1 \ + \ c_2 W_2 \ + \ c_3 W_3 \tag{2.2}$$

where $c_1,\ c_2$, and $c_3$ are the loading coefficients of each end member and $c_1 + c_2 + c_3 = 1$.

The Weibull end members were determined using a MATLAB code provided by Dr. David McGee (personal communication, 2015). This code was used by *McGee et al.* (2013) to separate eolian from hemipelagic input. The best fit model was determined based on a small root mean square (RMS) deviation value between modeled and the observed grain size distribution. The average RMS error for the four cores used in this thesis was between 0.18 - 0.4 %. The RMS error at each depth for every core is taken as the error associated with the end member modeling.

## Results from End Member Modeling

Figure 2.13 shows the best fit Weibull end members for the four cores. The finest end member EM1 has a mode between 1 - 5 $\mu$m with a very narrow distribution. Coarser end members EM2 and EM3 have broader distributions and modes at $\sim$10, and between 15 - 40 $\mu$m, respectively for the three EEP cores. These modes are fairly consistent with *Saukel*

*et al.* (2010) who uses four end members for the grain size distribution in the equatorial and subtropical Pacific surface sediments. According to *Saukel et al.* (2010), surface sediment from the Panama Basin mainly consists of dust/hemipelagic clay, authigenic minerals from the spreading center, and coarse grained volcanic glass from the Galapagos Islands.

For the central Pacific core, EM2 has a narrow mode about 10 $\mu$m before barite was removed. This mode is at 5 $\mu$m after the barite removal. In both cases, EM3 has a broad mode about 15 $\mu$m (Figure 2.13, bottom panel).

The finest end member EM1 was used as eolian end member for this study as its mode is consistent with the grain size mode of atmospheric dust in the EEP (*Prospero and Bonatti*, 1969; *Rea and Hovan*, 1995) as well as with the eolian end member from *Saukel et al.* (2010). EM2 and EM3 comprise both sorted and unsorted silt fractions and contain a mixture of hemipelagic and authigenic particles. These end members may incorporate more than one sediment population (*Saukel et al.*, 2010), thus making the identification of the origin of the end members ambiguous.

## 2.8 Quantitative Analysis

### 2.8.1 Grain Size Fraction

The DIGS distributions were divided into different size fractions (Table 2.2). These size fractions are differentiated according to their associated particle characteristics (e.g., sortable/unsortable) and suspected origin (e.g., dust).

Table 2.2: Size fractions and their descriptions.

| **Size fraction** | **Sediment type** | **Descriptive terminology used in this thesis** |
|---|---|---|
| 1 - 5 $\mu$m | Clay and very fine silt | Labeled as dust if sorted |
| 1 - 10 $\mu$m | Clay, very fine and fine silt | - |
| 10 - 63 $\mu$m | Fine, medium and coarse silt | Sortable Silt |
| $>$ 63 $\mu$m | Sand | - |

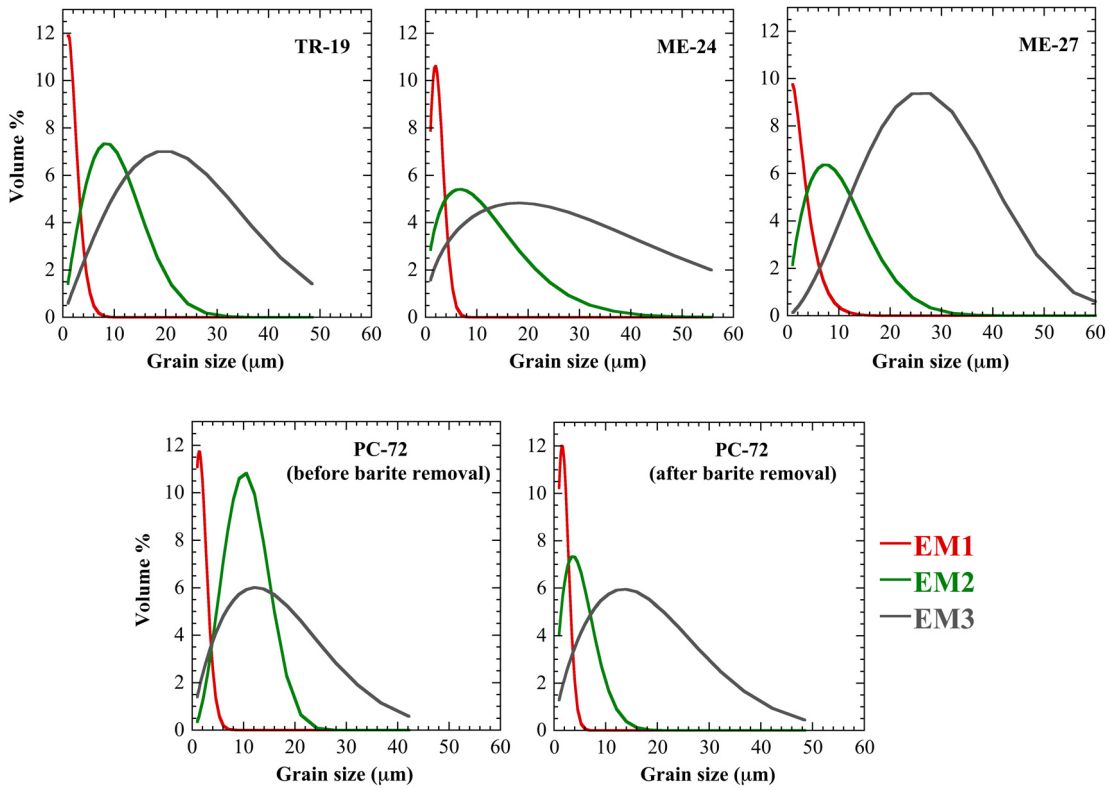


Figure 2.13: Best fit Weibull distribution functions representing three end members for the EEP cores (Top panel) and central Pacific core (Bottom panel). The fine end member EM1 is interpreted as eolian.

The volume contribution of each size fraction to the total volume was calculated as

$$V_{ij} = \sum_{m=i}^{j} f_m \tag{2.3}$$

where $V_{ij}$ is the volume (%) between grain size $i$ and $j$ and $f_m$ is the volume fraction (%) in size class $m$.

### 2.8.2 $^{230}$Th Normalized Bulk Flux

The vertical flux of material to the sea floor can be estimated using the known production rate of the radiogenic isotope thorium-230 ($^{230}$Th) in the water column (*Francois et al.*, 2004). Since $^{230}$Th is very particle reactive, it adsorbs to settling particles and is quickly scavenged from the water column. Thus, the flux of $^{230}$Th reaching the sea floor is expected to be approximately equal to its production rate by $^{234}$U decay in the overlying

water column. The relationship between the vertical flux and scavenged $^{230}$Th is explained more in Section (1.2.2) and given by Equation 1.4.

$$F_v = \frac{\beta_{230} \times z}{^{230}Th_{xs,\,0}}$$

where $F_v$ is the bulk vertical flux, $\beta_{230}$ is the production rate of $^{230}$Th (0.0267 dpm m$^{-3}$ yr$^{-1}$) over the water depth of z (m) and $^{230}Th_{xs,\,0}$ is the excess scavenged thorium concentration (dpm g$^{-1}$) corrected for decay and in-situ production of $^{230}$Th from authegenic and detrital uranium.

### 2.8.3 $^{232}$Th-based Dust Flux

Unlike $^{230}$Th, which is produced in seawater and occurs only at trace levels, thorium-232 ($^{232}$Th) is a primordial isotope and is significantly enriched in continental crust compared to oceanic crust and mid ocean ridge basalts (*Anderson et al.*, 2006; *McGee et al.*, 2007). Because of this, $^{232}$Th is used as a dust proxy, particularly suitable in regions where there are no other significant terrigenic sediment sources (*Winckler et al.*, 2008). Equation 1.5 gives the relationship between the bulk vertical flux and flux of a component "i" in the sediment. Thus, the vertical flux of $^{232}$Th ($F_i$) is,

$$F_i(g\ m^{-2}yr^{-1}) = F_v \times f_i$$

where, $f_i$ is the concentration of $^{232}$Th ($\mu$g g$^{-1}$) in the sediment. A $^{232}$Th-based dust flux estimate was obtained by dividing the $^{232}$Th flux by the average $^{232}$Th concentration of the upper continental crust (10.7 ppm, *Taylor and McLennan*, 1985).

$$Dust_{Th} = \frac{F_v \times {}^{232}Th}{10.7\ ppm} \tag{2.4}$$

where Dust$_{Th}$ is $^{232}$Th-based dust flux (g m$^{-2}$ yr$^{-1}$).

### 2.8.4 Grain size-based Dust Flux

*Prospero and Bonatti* (1969) collected atmospheric dust in the EEP and found that dust mass peaks in the 2 - 5 $\mu$m range. *Prospero* (1999) found that dust after long distance

transport typically shows a mode in the 2 - 5 $\mu$m grain size range. Therefore, among the three end members (Section 2.7), the finest end member (EM1 which has mode in the 1 - 5 $\mu$m size range) was considered to be of eolian origin. The loading coefficient of EM1 gives the volume contribution of the dust fraction in each sample depth. Since the grain size distributions were obtained from the inorganic fraction of the sediment, the dust contribution to the bulk sediment can be obtained by:

$$\%\ Dust_{bulk} = \frac{c_1 \times \%\ Inorg}{100} \tag{2.5}$$

where $c_1$ is the dust loading in each sample depth and $\%\ Inorg = (100 - CaCO_3 - Org.\ Carbon - Opal)\ \%$. The grain size-based dust flux was then calculated using Equation 1.5.

$$F_i(g\ m^{-2} yr^{-1}) = F_v\ \times\ f_i$$

*or*

$$Dust_{GS} = \frac{F_v\ \times \%Dust_{bulk}}{100} \tag{2.6}$$

where, Dust$_{GS}$ is the grain size-based dust flux (g m$^{-2}$ yr$^{-1}$) and F$_v$ is the total vertical flux.

### 2.8.5 Sorting Coefficient

Sediment sorting occurs during resuspension and/or deposition. Sediment that has undergone hydrodynamic sorting shows a modal peak in its grain size distribution. The width of the peak depends on the degree of sorting. If the sediment has undergone a high degree of sorting, the grain size distribution shows a narrow modal peak, conversely a less sorted sediment is expected to show a broader peak (*McCave et al.*, 1995; *McCave and Hall*, 2006).

The degree of sorting can be calculated as the standard deviation (sorting coefficient) about the mean and reflects the variation in grain sizes that makes up the sediment. Since sorting of deep sea sediments occurs in the sortable silt size range only, the sorting coefficient of the sortable silt fraction was calculated in this study. For this, the volume in

each size class between 10 - 63 $\mu$m was renormalized to 100%. Thus, the renormalized volume fraction ($f'_m$) is

$$f'_m = \frac{f_m}{V_{ss}} \times 100\% \tag{2.7}$$

where $f_m$ is the volume fraction in size class $m$ ($m$ ranges from 10 - 63 $\mu$m) and $V_{ss}$ is the total volume in sortable silt fraction. The sorting coefficient of sortable silt fraction was then calculated using the method of moments (*Blott and Pye*, 2001).

$$\sigma_g = exp \sqrt{\frac{\sum_{m=i}^{j} f'_m \left(\ln m - \ln \overline{x_g}\right)^2}{100}} \tag{2.8}$$

where $\sigma_g$ is the geometric standard deviation that represents the sorting coefficient and $\overline{x_g}$ is the geometric mean of the distribution. The geometric mean is described quantitatively as

$$\overline{x_g} = exp \frac{\sum_{m=i}^{j} f'_m \ln m}{100} \tag{2.9}$$

A high sorting coefficient indicates greater variation in grain sizes, i.e. a lower degree of sorting. Conversely, a lower sorting coefficient indicates a higher degree of sorting.

### 2.8.6 Focusing Factor

The focusing factor estimates the extent of sediment redistribution on the sea floor using the inventory of $^{230}Th_{xs,\,0}$ in the sediment. If the production rate of $^{230}$Th in the overlying water column corresponds to the flux of scavenged $^{230}$Th to the sea floor, then the concentration of scavenged $^{230}$Th in the sediment between depth $Z_1$ and $Z_2$ should be equal to its production rate in the overlying water column integrated over the time of accumulation of the depth interval (*Francois et al.*, 2004):

$$\int_{Z_1}^{Z_2} {}^{230}Th_{xs,\,0} \times \rho \quad dz = \int_{t_1}^{t_2} \beta_{230} \times z \quad dt \tag{2.10}$$

where $\rho$ is the dry bulk density and $t_1$ and $t_2$ are the corresponding ages for the depths $Z_1$ and $Z_2$, respectively. This relationship only holds true if there is no syndepositional redistribution of the sediment. Sediment redistribution on the sea floor changes the $^{230}$Th inventory in the sediment. *Suman and Bacon* (1989) quantified the syndepositional sediment redistribution as focusing factor ($\Psi$) where

$$\Psi = \int_{Z_1}^{Z_2} \frac{^{230}Th_{xs,\,0} \times \rho}{\beta_{230} \times z\,(t_2 - t_1)} \quad dz \tag{2.11}$$

A focusing factor of 1 ($\Psi = 1$) indicates that sediments are undisturbed, thus, accumulation of $^{230}$Th in the sediment is equal to production of $^{230}$Th in the overlying water column. A focusing factor greater than 1 ($\Psi > 1$) indicates lateral addition of $^{230}$Th to a given site which results in higher local accumulation of $^{230}$Th than predicted by its production rate in the overlying water column. Similarly, a focusing factor less than 1 ($\Psi < 1$) indicates winnowing i.e., the removal of $^{230}$Th due to lateral sediment movement.

Dry bulk density ($\rho$) of the three EEP cores was estimated from their carbonate content using an empirical relationship published by *Snoeckx and Rea* (1994).

$$\rho = \frac{1}{3.6 - 0.0279 \times \%\, CaCO_3} \tag{2.12}$$

For the central Pacific core PC-72, the relationship detailed by (*Murray and Leinen*, 1993), which is more appropriate for high carbonate setting, was used.

$$\rho = [1.012 \times 10^{-4}\,(\%\, CaCO_3)^2] - [3.277 \times 10^{-3}\,(\%\, CaCO_3)] + 0.337 \tag{2.13}$$

## 2.9 Acquisition of Data

Total $^{230}$Th and $^{232}$Th data of cores TR-19, ME-27 and ME-24 are taken from *Kienast et al.* (2007, 2013). These data were obtained using isotope dilution on an Inductive Coupled Plasma Mass Spectrometer (ICP-MS) following acid digestion of sediment samples. The organic carbon ($C_{org}$), carbonate ($CaCO_3$) and opal data for these cores were taken from

*Dubois et al.* (2011) and *Kienast et al.* (2007). A description of the methods and their associated error can be found in these references.

For the central Pacific core PC-72, $^{232}$Th data as well as $^{232}$Th-based dust flux estimates were taken from *Winckler et al.* (2008). $^{230}$Th, $^{230}$Th normalized bulk flux, carbonate ($CaCO_3$) and opal data are from *Hayes et al.* (2011). The total organic carbon ($C_{org}$) values from *Murray et al.* (2000, 2012) were interpolated (using the software AnalySeries) to obtain a $C_{org}$ value for the corresponding depths in *Hayes et al.* (2011). Barium (Ba) and Aluminum (Al) data of PC-72 were taken from *Murray et al.* (2000, 2012). The bulk vertical flux as well as $^{232}$Th-based dust flux for all four cores were calculated as described in Sections 2.8.2 and 2.8.3, respectively. A list of all data sources is provided in Table 2.3.

Table 2.3: Core ID and data sources.

| **Core ID** | **Data** | **References** |
|---|---|---|
| TR163-19P | Age model | *Dubois et al.* (2011) |
| | Org carbon, $CaCO_3$, Opal | *Kienast et al.* (2007) |
| | DIGS | This study |
| | $^{230}$Th and $^{232}$Th | *Kienast et al.* (2007) |
| | Fe, Mg, and Al | *S. Kienast and S. Calvert,* unpublished |
| ME0005A-24JC | Age model | *Dubois et al.* (2011) |
| | Org carbon, $CaCO_3$, Opal | *Kienast et al.* (2007) |
| | DIGS | *S. Kienast,* unpublished |
| | $^{230}$Th and $^{232}$Th | *Kienast et al.* (2007, 2013) |
| | Fe, Mg, and Al | *S. Kienast and S. Calvert,* unpublished |
| ME0005A-27JC | Age model | *Dubois et al.* (2011) |
| | Org carbon, $CaCO_3$, Opal | *Kienast et al.* (2007) |
| | DIGS | *S. Kienast,* unpublished |
| | $^{230}$Th and $^{232}$Th | *Kienast et al.* (2007) |
| TTN013-PC72 | Age model | *Winckler et al.* (2008); *Hayes et al.* (2011) |
| | $\delta^{18}$O | *Murray et al.* (2000, 2012) |
| | Org carbon | *Murray et al.* (2000, 2012) |
| | $CaCO_3$, Opal | *Hayes et al.* (2011) |
| | DIGS | This study |
| | $^{230}$Th and $^{232}$Th | *Winckler et al.* (2008); *Hayes et al.* (2011) |
| | Ba and Al | *Murray et al.* (2000, 2012) |

# CHAPTER 3

# RESULTS

## 3.1 Disaggregated Inorganic Grain Size Distributions

### 3.1.1 The Eastern Equatorial Pacific Cores

Figures 3.1, 3.2, and 3.3 show downcore disaggregated inorganic grain size (DIGS) distributions of the three eastern equatorial Pacific (EEP) cores TR-19, ME-24, and ME-27, respectively, over the last 30 ka. Each DIGS distribution is shown with its corresponding depth and age. The shaded blue area shows the sortable silt size (SS) range.

The distributions of TR-19 (Figure 3.1) show a small peak in the size class between 1 - 5 $\mu$m (dust) and no material coarser than 50 $\mu$m. The first two depths (0.5 and 3.5 cm) show a mode in the fine silt range (between 10 and 20 $\mu$m) and a minor mode in the 1 - 5 $\mu$m size range. The same trend also appears in two deeper depths (30.5 and 33.5 cm). DIGS distributions from depths 15.5 and 21.5 cm and subsequent depths of 45.5, 48.5 and 51.5 cm show a flatter distribution between 10 - 30 $\mu$m. No modal peak in the SS size range is seen at 54.5 cm depth. DIGS from 60.5 to 123.5 cm depths have a bimodal distribution with modes at $\sim$2 $\mu$m and $\sim$10 $\mu$m. Compared to the shallower depths (0.5 to 51.5 cm), where the SS mode appears at $\sim$12 $\mu$m, deeper depths (57.5 to 123.5 cm) show a slightly finer SS size mode ($\sim$10 $\mu$m). The modes between 1 - 5 $\mu$m size range are highest for depths 48.5, 111.5 and 123.5 cm.

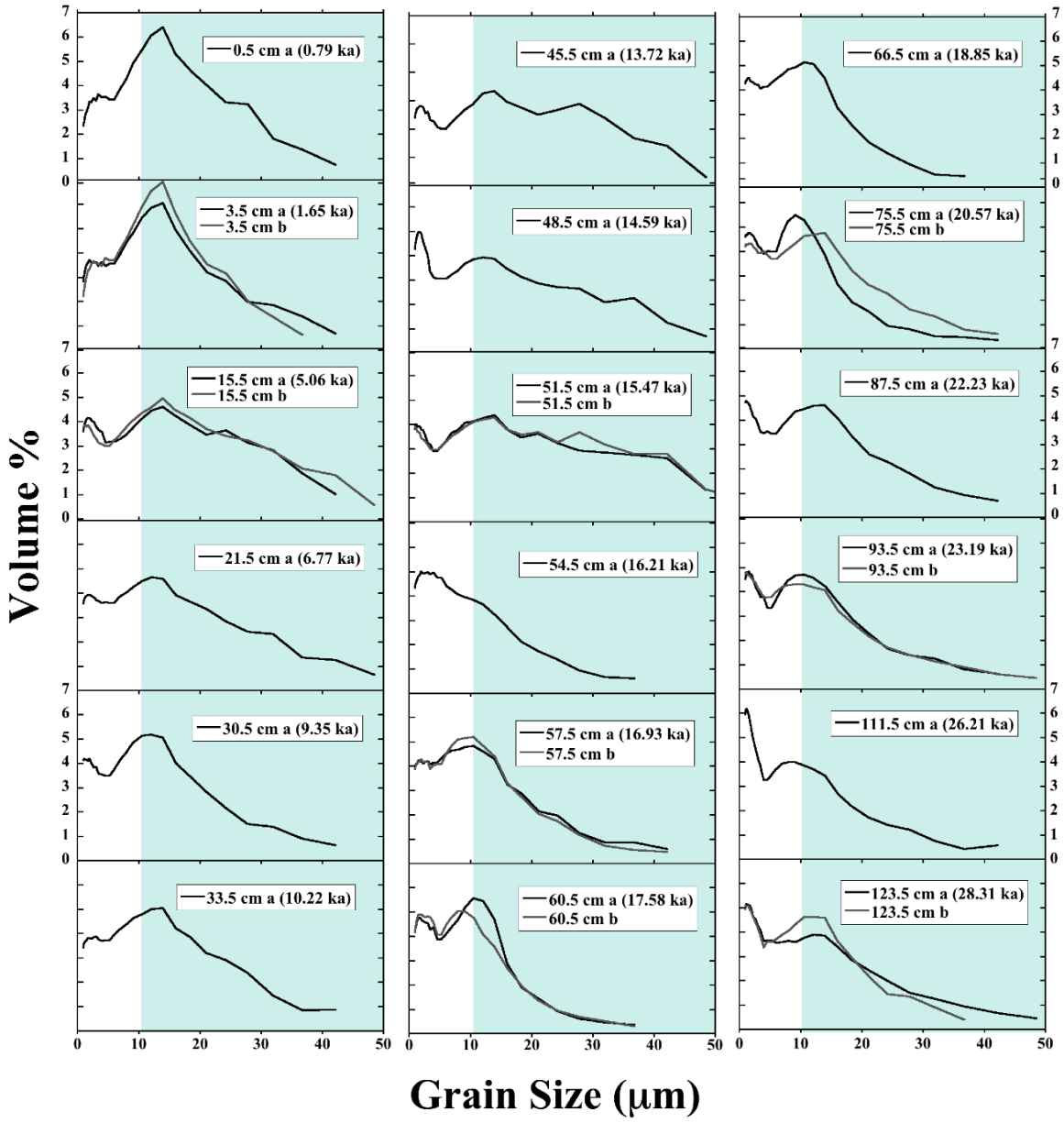


Figure 3.1: Downcore DIGS distributions of the core TR-19 with corresponding depth and age. The shaded blue area represents the sortable silt size range (10 - 63 $\mu$m).

Unlike TR-19, ME-24 does not show bimodal DIGS distributions in most cases (Figure 3.2). Most of the depths contain materials finer than 50 $\mu$m, however the first three shallow depths (0, 8, and 28 cm) and two deeper depths (80 and 335 cm) also contain coarser materials (50 - 60 $\mu$m). The mode in the 1 - 5 $\mu$m size range is more pronounced than in TR-19 and reaches up to 8 vol %. A few depths in ME-24 (52, 92, 100, 120, 136, and 140 cm) also show a small shoulder in their DIGS distributions at $\sim$10 $\mu$m.

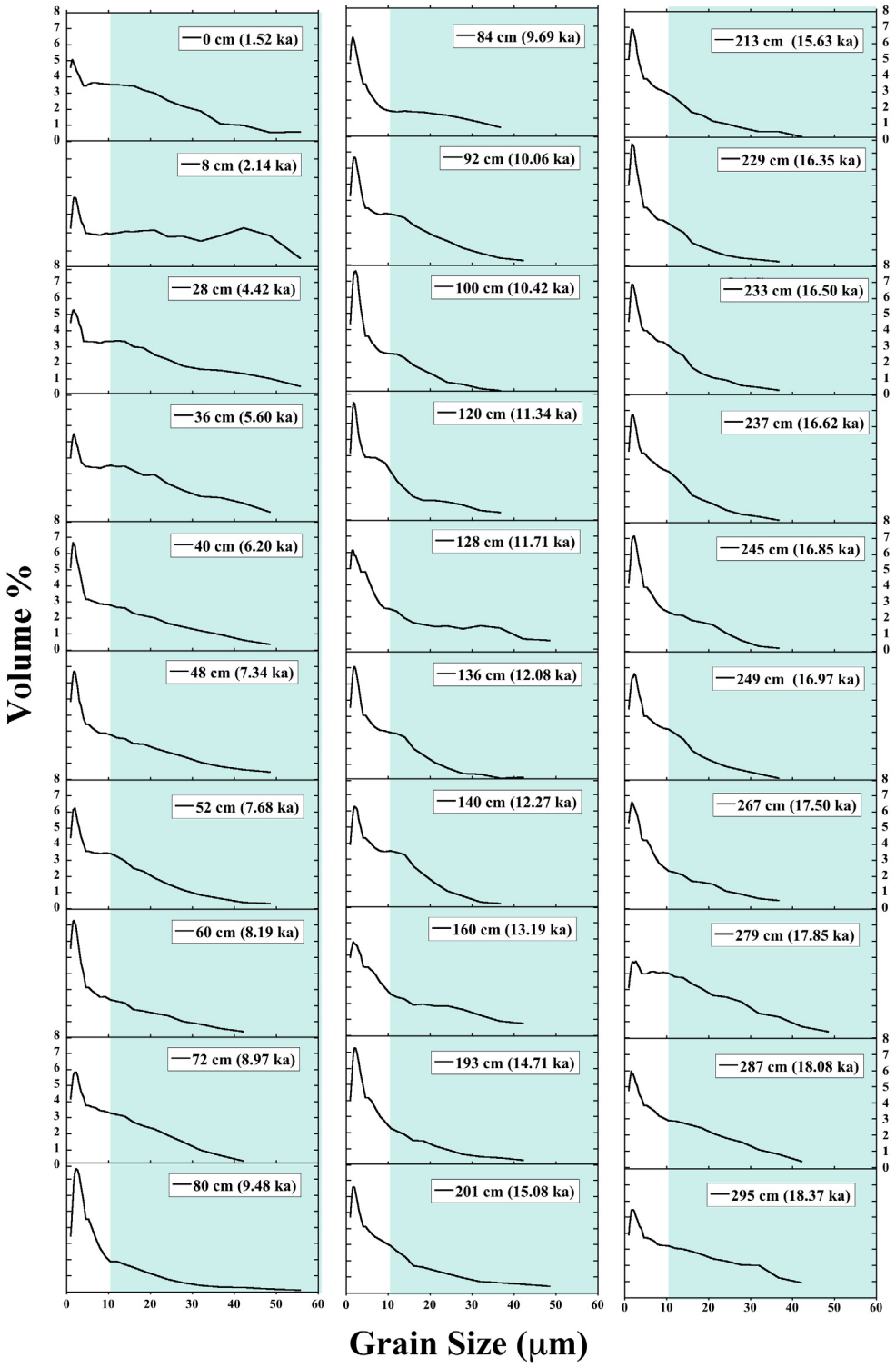


Figure 3.2: Downcore DIGS distributions of the core ME-24 with corresponding depth and age. The shaded blue area represents the sortable silt size range (10 - 63 $\mu$m).

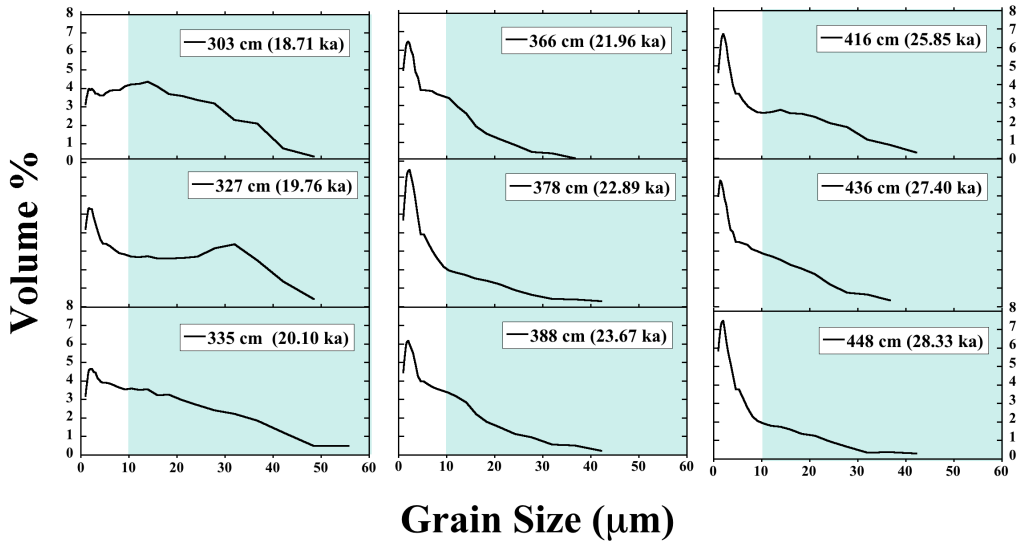


Figure 3.2: (cont.) Downcore DIGS distributions of the core ME-24 with corresponding depth and age. The shaded blue area represents the sortable silt size range (10 - 63 $\mu$m).

DIGS distributions of ME-27 do not show material coarser than 60 $\mu$m but contain a higher percentage of coarser grains, on average, compared to TR-19 and ME-24 (Figure 3.3). Shallow depths (2 to 36 cm) show a broad mode in the sortable silt size range and a smaller peak (4 vol %) in the 1 - 5 $\mu$m size range. The sortable silt mode, however, disappears in the deeper depths (60.5 to 166 cm) and the peak between the 1 - 5 $\mu$m reaches up to 7 vol % at these depths. This peak decreases slightly in the depths 118, 134, and 149.5 cm.

**Size Fractions**

The volume contribution of different size fractions as described in Table 2.2 to the total volume was calculated using Equation 2.3 for the three EEP cores over the last 30 ka (Figure 3.4). In all three cores, the 1 - 5 $\mu$m fraction contributes >70 % of the 1 - 10 $\mu$m fraction of the sediment.

TR-19 (Figure 3.4(a)) shows a gradual decrease in the 1 - 10 $\mu$m fraction from the glacial period to the Holocene. On average, the Holocene shows the highest (36.67 vol %) sortable silt (SS) fractions (10 - 63 $\mu$m) in this core. Similarly, ME-24 also has the highest SS (average of 22.28 vol %) during the late Holocene (Figure 3.4(b)). However, the

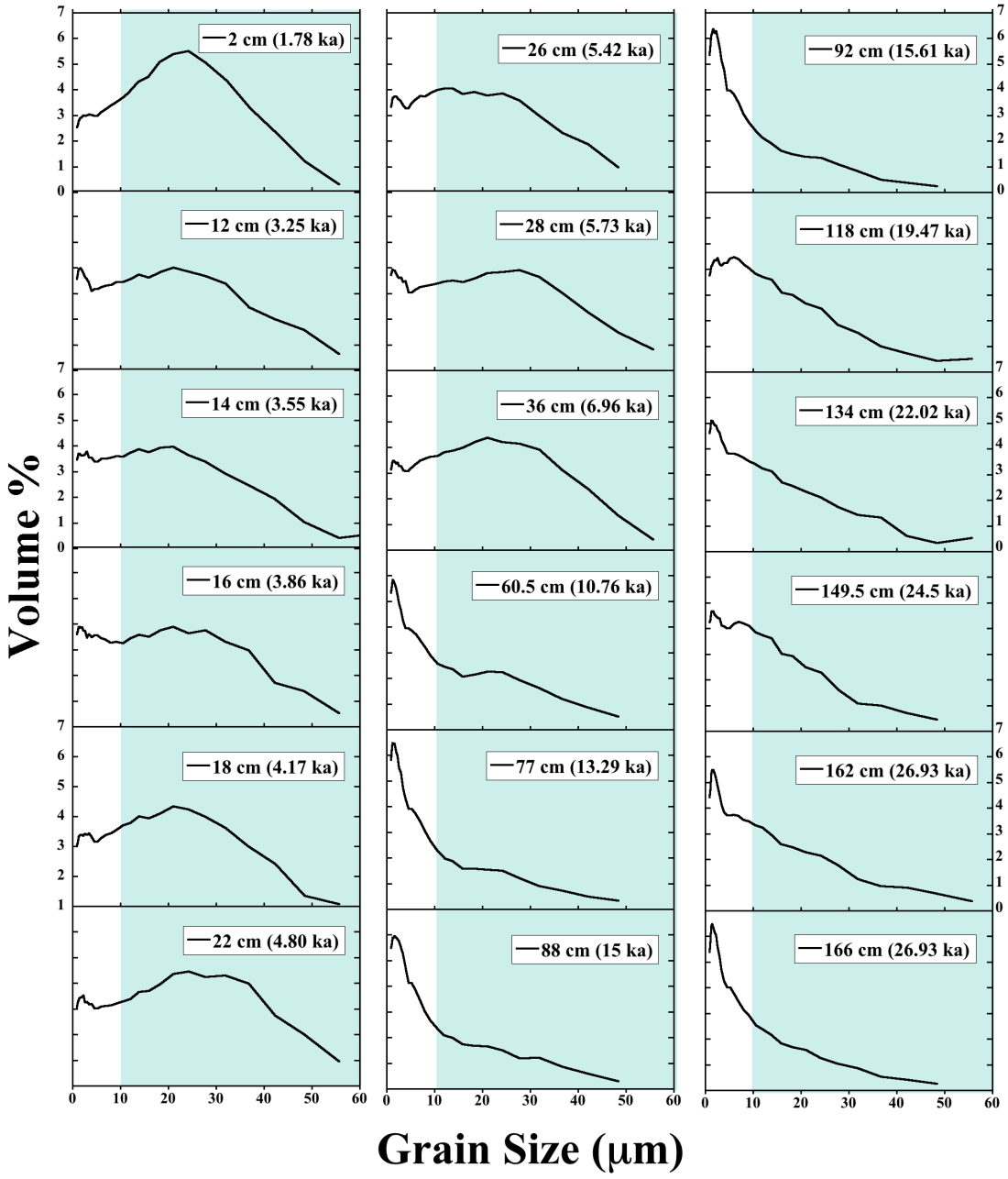


Figure 3.3: Downcore DIGS distributions of the core ME-27. The shaded blue area shows the sortable silt size range (10 - 63 $\mu$m).

concentration of the SS fraction gradually decreases from the Holocene to the transition period (average of 16 %). Overall, ME-24 shows a high average concentration of the 1 - 10 $\mu$m fraction (ranging from 77.7 to 83.6 vol %) compared to TR-19 and ME-27. ME-27 shows the lowest (average of 57.97 vol %) 1 - 10 $\mu$m fraction and the highest (average of

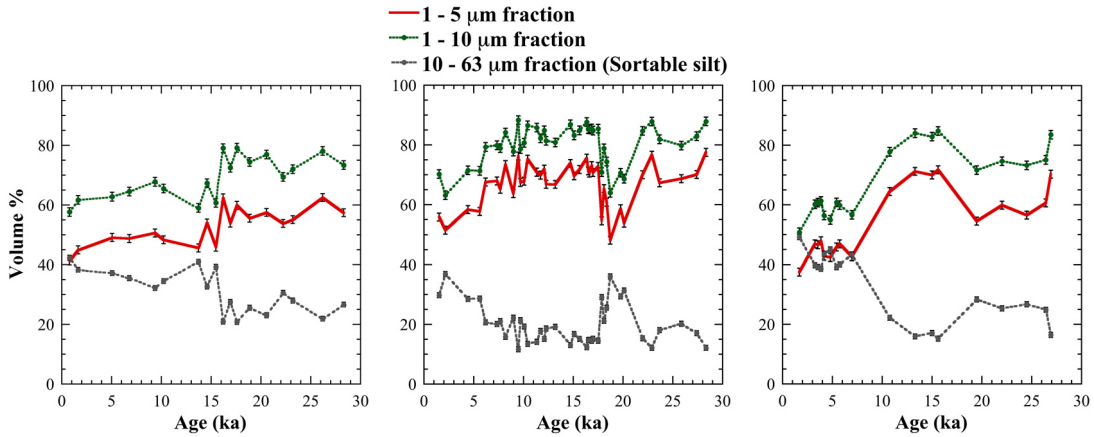


(a) TR- 19 (b) ME-24 (c) ME-27

Figure 3.4: Contribution of the different size fractions (as described in Table 2.2) to the total volume for the EEP cores over the last 30 ka. Red lines show the 1 - 5 $\mu$m fraction, green dotted lines show the 1 - 10 $\mu$m fraction of the sediment and grey dotted lines show the sortable silt fraction of the sediment (10 - 63 $\mu$m). Error bars are the corresponding size fraction errors in Standard-1 (1.32, 1.44, and 0.81 % errors in 1 - 5, 1 - 10, and 10 - 63 $\mu$m size fraction, respectively; see Figure 2.7).

42.02 %) SS fraction during the Holocene (Figure 3.4(c)). The transition period shows the highest 1 - 10 $\mu$m fraction (average of 82.37 vol %) in this core.

### 3.1.2 The Central Pacific Core

The DIGS distributions for two glacial-interglacial cycles (0 - 100 cm and 200 - 265 cm) were obtained for the central Pacific core PC-72 (Figure 3.5). The first glacial-interglacial (G-IG) cycle (15 - 100 cm corresponding to 6 - 39 ka ) has no material coarser than 40 $\mu$m and shows very high peaks (up to 12 vol %) between 1 - 5 $\mu$m. These peaks are higher than in any of the EEP cores. DIGS distributions from depths of 50 - 100 cm, except 55 cm, show another mode at around 10 $\mu$m grain size. Samples from depths of 80 and 100 cm clearly have a bimodal distribution (a dust mode and a SS mode). Most DIGS distributions of the second G-IG cycle (200 - 265 cm corresponding to 100 - 143 ka) have a small quantity of material coarser than 40 $\mu$m. The 1 - 5 $\mu$m peaks are lower than the peaks in the first G-IG cycle. There are no bimodal distributions within this cycle, however material coarser than 10 $\mu$m has a larger volume contribution compared to the first cycle (Figure 3.5).

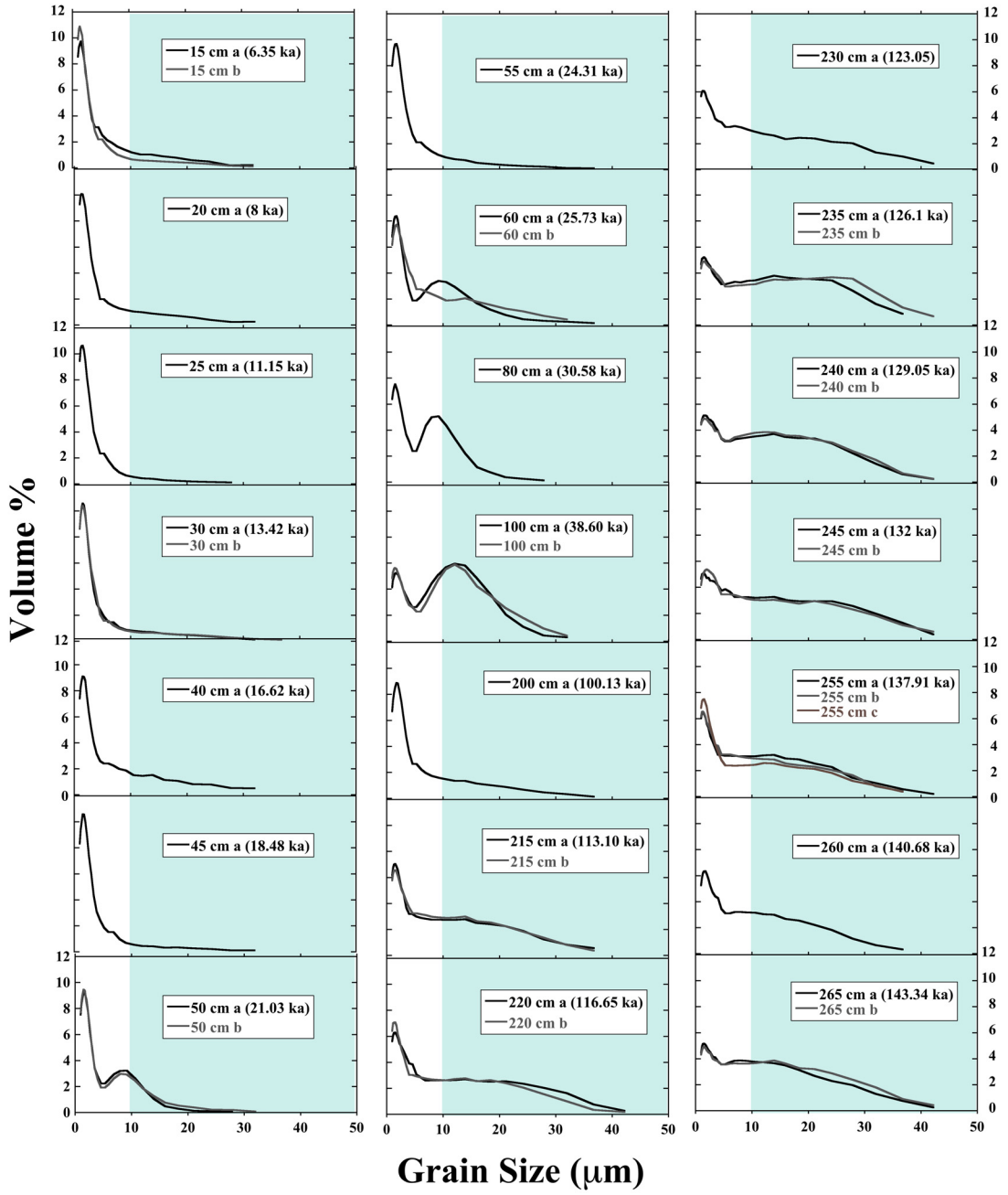


Figure 3.5: Downcore DIGS distributions of the central Pacific core PC-72 over the two glacial-interglacial cycles. The shaded blue area represents the sortable silt size range (10 - 63 $\mu$m).

#### 3.1.2.1 After Barite Separation

Figure 3.6 shows the DIGS distributions for the central Pacific core after the removal of biogenic barite compared to the original DIGS distributions shown in Figure 3.5. Many

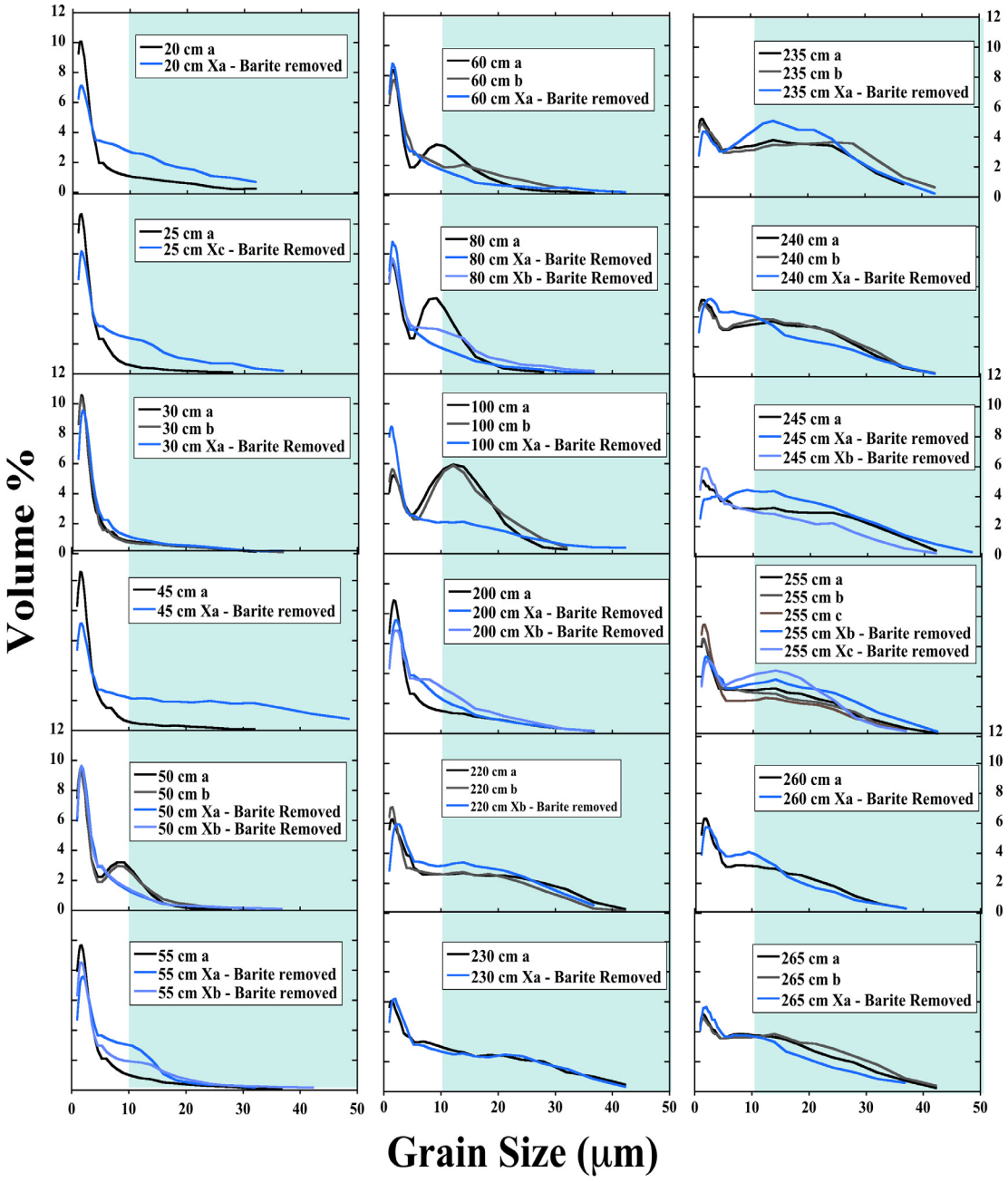


Figure 3.6: Downcore DIGS distributions of the central Pacific core PC-72 after the barite was removed (blue lines) compared to the samples prior to the barite removal (black lines) (from Figure 3.5). The shaded blue area shows the sortable silt size range (10 - 63 $\mu$m).

distributions are clearly different before and after the barite removal. After barite removal, the distributions show a decrease in the 1 - 5 $\mu$m peak, except at 80 and 100 cm depths where this peak increases. This decrease in the 1 - 5 $\mu$m peak is accompanied by an

increase of the fraction coarser than 10 $\mu$m. The SS modes between 50 and 100 cm depths disappeared after the barite was removed. Except at the 235 cm depth, none of the depths show a bimodal distribution after barite removal.

#### 3.1.2.2 Size Fractions

Figure 3.7(a) shows the volume % of different size fractions for PC-72 before barite removal. The 1 - 10 $\mu$m fraction is almost entirely made up of the 1 - 5 $\mu$m fraction. The SS fraction (10 - 63 $\mu$m) makes up less than 15 % of the total sediment in the first G-IG cycle (Figure 3.7(a): Top panel) except at 40 ka, where the SS fraction is 30 % of the sediment. In the second G-IG cycle, the 1 - 10 $\mu$m material contributes to 70 - 80 % of the sample, except at 100 ka (91.3 vol %). Unlike the first cycle, SS makes up about 15 - 30 % of the sediment.

After the barite removal, the samples show similar distributions of size fractions (Figure 3.7(b)). The 1 - 10 $\mu$m fraction consists almost entirely of 1 - 5 $\mu$m in both cycles and the first G-IG cycle still shows more 1 - 10 $\mu$m fraction than the second cycle. After the removal of barite, the volume of the 1 - 10 $\mu$m fraction decreases by 12.7 % on average during the Holocene and increases by 21.5 % at 40 ka. The second G-IG cycle shows no significant changes in average size fraction before and after the procedure.

## 3.2 Dust Flux

### 3.2.1 $^{232}$Th-based Dust Flux

The $^{232}$Th-based dust (dust$_{Th}$) fluxes for the three EEP cores calculated using Equation 2.4 are shown in Figure 3.8. Dust fluxes throughout the last 30 ka show a systematic decrease from south (ME-27) to north (TR-19) and with distance from the continent. The flux at TR-19 ranges between 0.2 and 0.5 g m$^{-2}$ yr$^{-1}$ whereas fluxes at ME-27 are consistently $>$1 g m$^{-2}$ yr$^{-1}$. TR-19 and ME-24 show higher dust fluxes during the glacial period compared to the Holocene. Both of these cores show peak dust flux during the transition period. However, dust$_{Th}$ spikes earlier in ME-24 (between 15 - 17 ka) than in TR-19 (between 13 - 17 ka). ME-27 does not show a consistent change in dust fluxes between the glacial

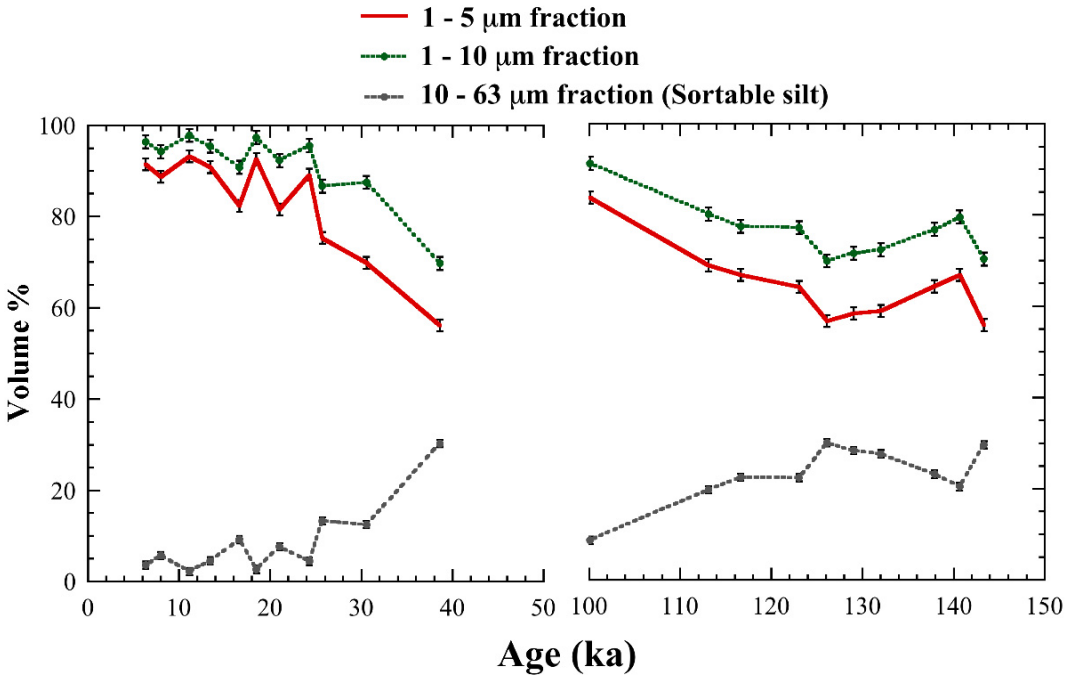


(a) Before barite removal

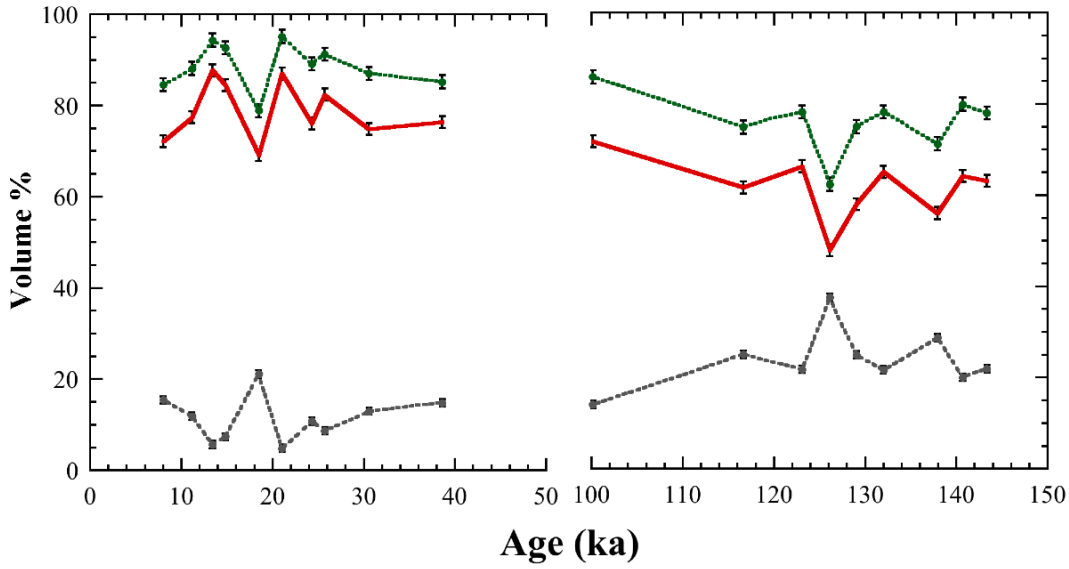


(b) After barite removal

Figure 3.7: Contribution of the different size fractions to the total volume for the central Pacific core PC-72 over the two glacial-interglacial cycles (a) before and (b) after the samples were subjected to barite removal. Red lines show the 1 - 5 $\mu$m fraction, green dotted lines show the 1 - 10 $\mu$m fraction of the sediment and grey dotted lines show the sortable silt fraction of the sediment (10 - 63 $\mu$m). Error bars are the corresponding size fraction errors in Standard-1 (1.32, 1.44, and 0.81 % errors in 1 - 5, 1 - 10, and 10 - 63 $\mu$m size fraction, respectively; Figure 2.7).

period and the Holocene. This core shows a very high peak in dust flux (7.5 g $m^{-2}$ $yr^{-1}$) at 5.6 ka that is not observed at other sites. This $dust_{Th}$ spike is caused by a high $^{232}Th$ concentration at this depth.

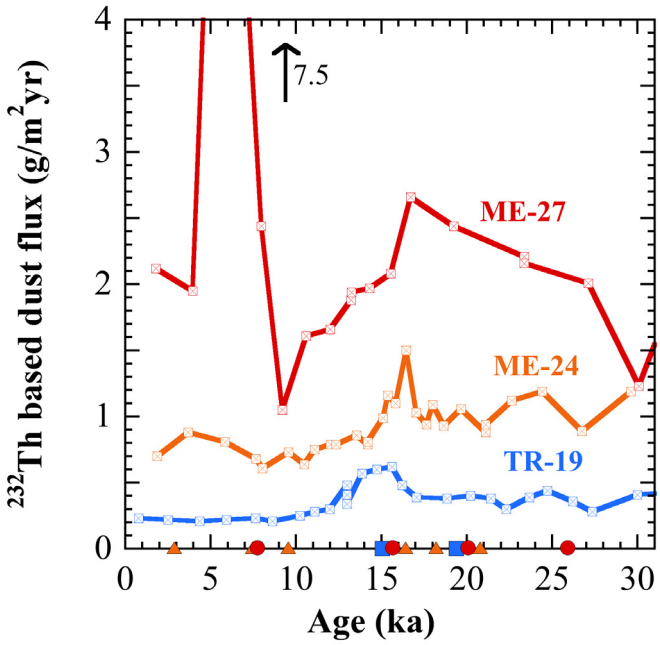


Figure 3.8: $^{232}Th$-based dust fluxes for the three EEP cores over the last 30 ka. The out of range dust flux value at 5.6 ka in ME-27 reaches 7.5 g $m^{-2}$ $yr^{-1}$. The symbols on the x-axis are the calibrated radiocarbon dates for TR-19 (blue boxes), ME-24 (orange triangles), and ME-27(red circles).

### 3.2.2 Grain Size-based Dust Flux

The grain size-based dust ($dust_{GS}$) fluxes (Figure 3.9) are largely consistent with the $dust_{Th}$ for the EEP cores over the last 30 ka. The absolute dust flux values between the two estimates are very comparable. Similar to $dust_{Th}$ fluxes, $dust_{GS}$ fluxes also show a decreasing offshore and an increasing north-south gradient. The fluxes in ME-27 are approximately four times higher than TR-19. The $dust_{GS}$ also shows increased fluxes during the transition in all three cores. This elevated dust flux is seen between 12 - 17 ka in ME-27, between 14 - 17 ka in ME-24, and between 13 - 17 ka in TR-19. These transition dust peaks are broader than the $dust_{Th}$ peaks. ME-24 shows a dust flux maximum between 10 and 14 ka where the flux reaches values as high as 3.1 g $m^{-2}$ $yr^{-1}$ at 11.3 ka.

The dust fluxes for the central Pacific core over the last two glacial-interglacial (G-IG)

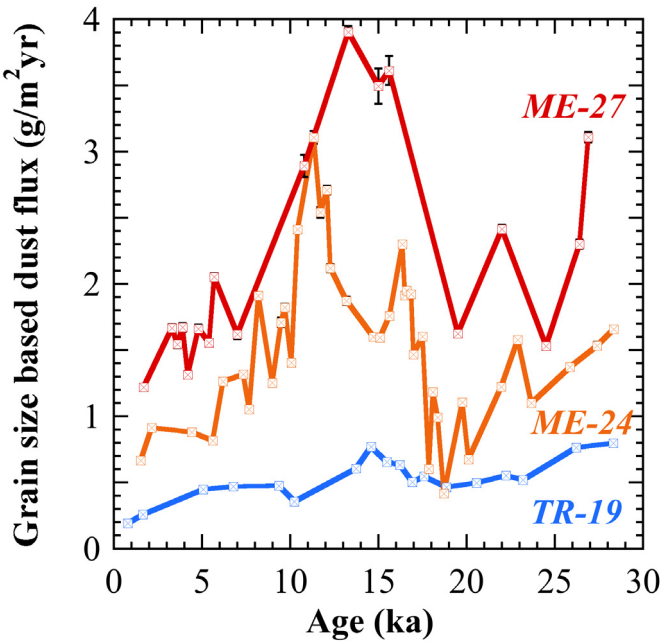


Figure 3.9: Grain size-based dust fluxes for the EEP cores over the last 30 ka. The error bars represent both, error associated with internal standard (Std-1) as well as errors from end member modeling. Errors are mostly <0.1g m$^{-2}$ yr$^{-1}$.

cycles are shown in Figure 3.10. The figure includes the dust fluxes from before and after the removal of barite. Before barite removal, the dust flux varies between 0.28 - 0.68 g m$^{-2}$ yr$^{-1}$ and there is a gradual increase of dust flux from the glacial period to the Holocene in the first cycle. In the second G-IG cycle, dust flux varies between 0.2 - 0.44 g m$^{-2}$ yr$^{-1}$. After the barite was removed, there is a high flux at 40 ka and the dust flux decreases during the Holocene. The flux after the barite removal tracks the flux before the removal but with a lower amplitude in the second G-IG cycle. Because of the large errors due to poor reproducibility of the replicate samples for barite removal process, the dust fluxes after the barite removal are not significantly lower than the fluxes before the removal.

## 3.3 Sorting Coefficient

Sorting coefficients calculated using Equation 2.8 for the three EEP cores are shown in Figure 3.11. The sorting coefficients are between 1.35 - 1.66, indicating moderately to well sorted sediments (*Blott and Pye*, 2001). All three cores show higher sorting coefficients (averaged over the time interval) during the Holocene (core top - 11 ka) compared to the

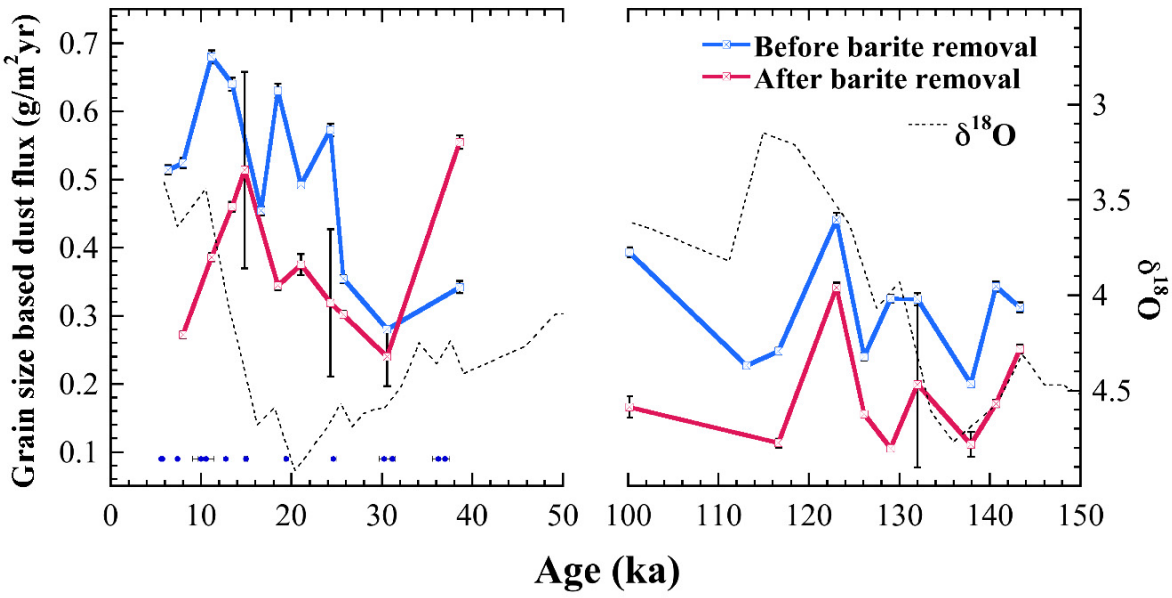


Figure 3.10: Grain size-based dust fluxes for PC-72 over the two glacial-interglacial cycles. The blue line shows the dust flux before and pink line shows the dust flux after the removal of barite. The error bars before the barite removal represent both errors associated with internal standard (Std-1) as well as errors from end member modeling. The error bars after barite removal include errors from Std-1, end member modeling errors, and errors associated with the barite removal process. The dotted black line shows the $\delta^{18}$O of the core (*Murray et al.*, 2000) for stratigraphic reference. The radiocarbon dates for the first 100 cm of the core (*Anderson et al.*, 2008) are shown as blue circles along the x-axis.

glacial (18 - 30 ka). Overall, ME-27 shows the highest values in all three time intervals and the lowest range of coefficients. The sorting coefficients are highest during the transition in TR-19 and lowest in ME-24 and ME-27. Overall, averaging the sorting coefficients across specified time intervals has large uncertainties associated, because of the high variability within the time intervals. As a result, the average sorting coefficient between different time intervals are not significantly different (*Wilcoxon signed-rank test, p-value* $> 0.05$), except between the Holocene and transition period in ME-27 (*p-value* = 0.014).

The central Pacific core does not show a consistent change in sorting coefficients between glacial and interglacial periods (Figure 3.12). Before the barite removal (Figure 3.12, blue lines), PC-72 shows well sorted sediments (1.27 - 1.41, *Blott and Pye*, 2001) in the first cycle and moderately well to well sorted sediments (1.38 -1.5, *Blott and Pye*, 2001) in the second. After the removal (Figure 3.12, pink lines), the first cycle shows overall higher sorting coefficients and a maximum value at 18.4 ka. The second cycle

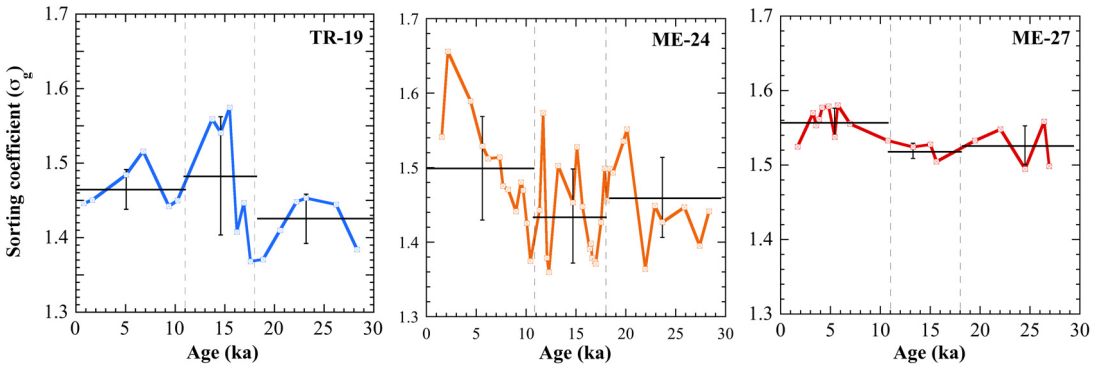


Figure 3.11: Sorting coefficients for the EEP cores calculated using geometric method of moments over the last 30 ka. Vertical dashed lines represent the boundary between different time intervals (core top to 11, 11 - 18, and 18 - 30 ka). Black horizontal lines give the average sorting coefficients with $\pm 1\sigma$ over the time intervals.

shows very small changes in sorting coefficients before and after the removal of barite.

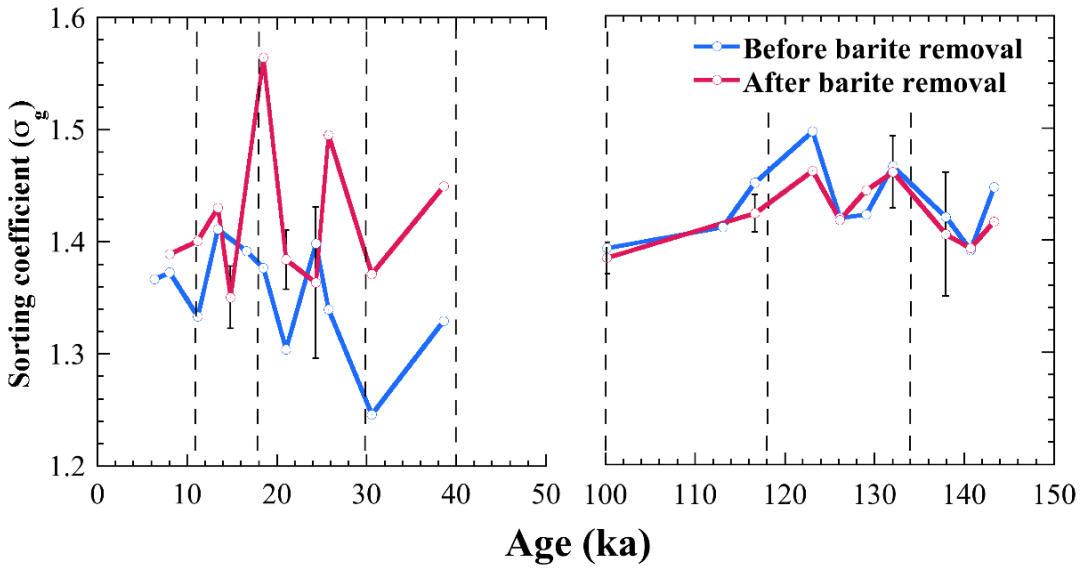


Figure 3.12: Sorting coefficients for the central Pacific core before (blue lines) and after (pink lines) the barite removal over the two glacial-interglacial cycles. Vertical dashed lines represent the boundary between different time intervals (core top - 11, 11 - 18, 18 -30 and 30 - 40 ka for the first G-IG cycle and 100 - 118, 118 - 134, and 134 - 144 ka for the second G-IG cycle).

## 3.4 Focusing Factor

All EEP cores show focusing factors higher than 1 (Figure 3.13). The cores show higher focusing during the glacial period compared to the Holocene. Among the three cores, ME-24 has the highest ($\psi$ = 4.8 - 6.9) and ME-27 has the lowest focusing factor ($\psi$ = 1.6 - 2). The focusing factor in ME-27 does not show a significant change between the three time intervals but is slightly lower during 11 - 18 ka. Similarly, TR-19 also shows a decreased focusing factor ($\psi$ = 1.9) during this time interval. Unlike the other two cores, ME-24 shows an increased focusing factor ($\psi$ = 6.9) during the 11 - 18 ka time interval.

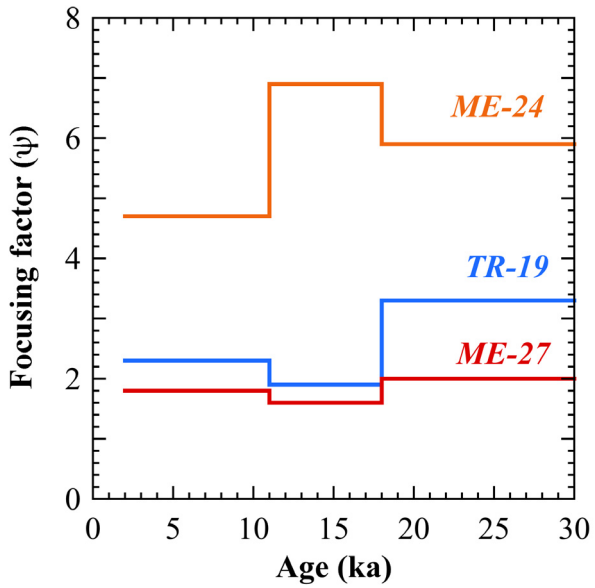


Figure 3.13: Focusing factors for the EEP cores for the time intervals from core top - 11, 11 - 18, and 18 - 30 ka.

In contrast, the central Pacific core shows higher focusing factors during the interglacial periods compared to the glacial periods (Figure 3.14). The highest focusing factor ($\psi$ = 3) is observed during the Holocene. Overall, the second G-IG cycle shows lower focusing factors than the first cycle.

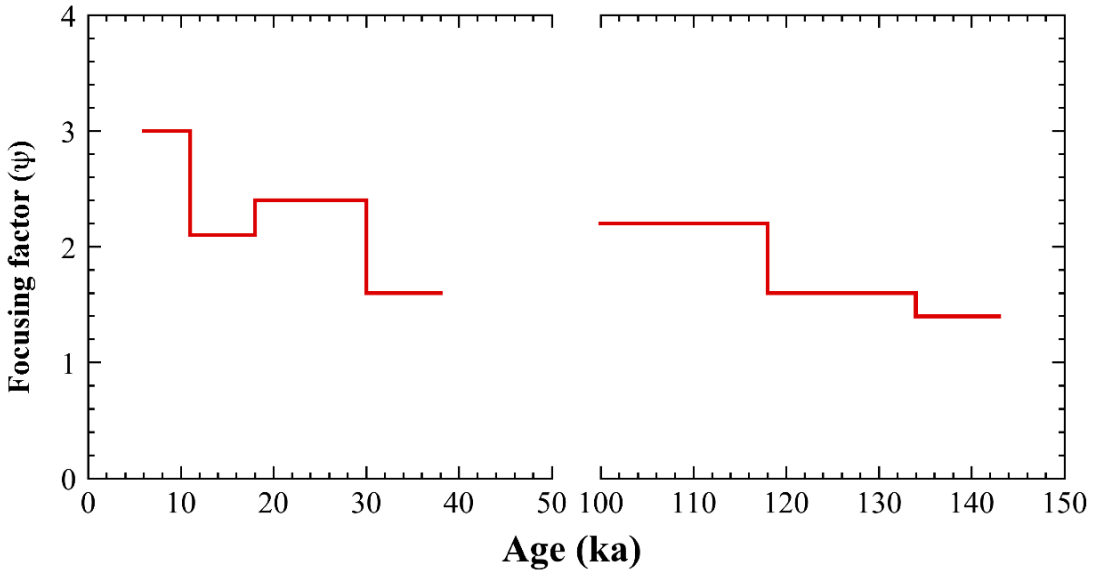


Figure 3.14: Focusing factors for the central Pacific core for the time intervals over two glacial-interglacial cycles. The time intervals are from core top - 11 ka, 11 - 18 ka, 18 - 30 ka, and 30 - 40 ka for the first cycle and 100 - 118 ka, 118 - 134 ka, and 134 - 144 ka for the second cycle. Note the break in x-axis.

# CHAPTER 4

# DISCUSSION

The discussion is organized as follows. First, the influence of different sources of material on DIGS distributions is examined to determine the most accurate grain size-based dust ($dust_{GS}$) flux. Secondly, the barite separation technique developed in this thesis is critically evaluated and recommendations for further method development are provided. Then, key findings regarding $dust_{GS}$ fluxes and their implications are discussed. Finally, sorting coefficients are compared to focusing factors and discussed in the context of the focusing debate.

## 4.1 Distinguishing Eolian from Other Sources in the Eastern Equatorial Pacific

The eastern equatorial Pacific (EEP) is a dynamic oceanographic region, influenced by a number of sedimentary sources that have the potential to bias dust estimates of eolian input. *Singh et al.* (2011) used $^{232}$Th as a proxy for detrital input in the EEP and found that the average $^{232}$Th flux decreases exponentially with distance from the continent. These authors assigned a distance of 300 km from the continental margin as the boundary between hemipelagic dominated sediment and eolian dominated sediment. Within 300 km, the sediments are mostly influenced by river runoff and hemipelagic material. As distance to the continental margin increases, wind derived sources dominate over hemipelagic sources and after 300 km, the sediments on the sea floor are largely eolian. This implies that

Table 4.1: Elemental ratios found in the upper continental crust (*Taylor and McLennan*, 1985), basalt (*Faure*, 1998) and hydrothermal sediments found south of the Galapagos Spreading center (*Corliss et al.*, 1978).

| Elemental ratio | Upper Continental crust | Basalt | Hydrothermal Deposits |
|---|---|---|---|
| Fe/Al | 0.44 | 1.3 | 43±8.7 |
| Mg/Al | 0.17 | 0.54 | 2.9±0.6 |

sediments at sites ME-24 and TR-19, which are located at a distance of 600 and 1250 km offshore, respectively, are mostly eolian (Table 2.1). However, core ME-27 at the distance of 155 km from the continent, could be affected by both hemipelagic as well as eolian sources.

The input of hemipelagic material could be the reason for the distinct $^{232}$Th-based dust (dust$_{Th}$) peak of 7.5 g m$^{-2}$ yr$^{-1}$ at 5.6 ka (Figure 3.8) in ME-27. This high dust$_{Th}$ flux is due to a high concentration of $^{232}$Th at this depth. Considering the absence of a grain size-based dust (dust$_{GS}$) peak at this depth, the dust$_{Th}$ peak in ME-27 indicates an influence of a hemipelagic source in addition to eolian sources. This interpretation is further supported by the absence of dust peaks in the other two proximal EEP cores (TR-19 and ME-24) at ∼5 ka. The influence of hemipelagic material, possibly at all the depths of ME-27, makes the interpretation of dust$_{Th}$ flux in ME-27 challenging.

*Kienast et al.* (2007) found that site ME-24 is influenced by hydrothermal material because of its close proximity (∼50 nautical miles) to the active Galapagos Spreading Center (Figure 2.1). *Saukel et al.* (2010) investigated the grain size composition of surface sediment samples, assumed to be of late Holocene age, from the tropical southeast Pacific and conducted end member modeling to identify the sediment population that contributes to the inorganic fraction of these sediments. The authors found that the area closest to site ME-24 is dominated by authigenic minerals and dust/hemipelagic clay with 60 - 71% smectite. The area closest to TR-19 is dominated by submarine volcanism containing 84 % smectite (*Saukel et al.*, 2010). Authigenic minerals are produced in-situ within the depositional site. A high percentage of smectites indicates a volcanic source because smectites are generally produced from wet weathering of submarine volcanic rocks (*Calvert and Pedersen*, 2007). *Kienast et al.* (2007) and *Saukel et al.* (2010) suggested that at site ME-24 and possibly also

at site TR-19, the fine fraction of the inorganic sediment may be influenced by authigenic and volcanic inputs from the Galapagos Spreading Center. To investigate these influences, the elemental composition of the sediment can be used.

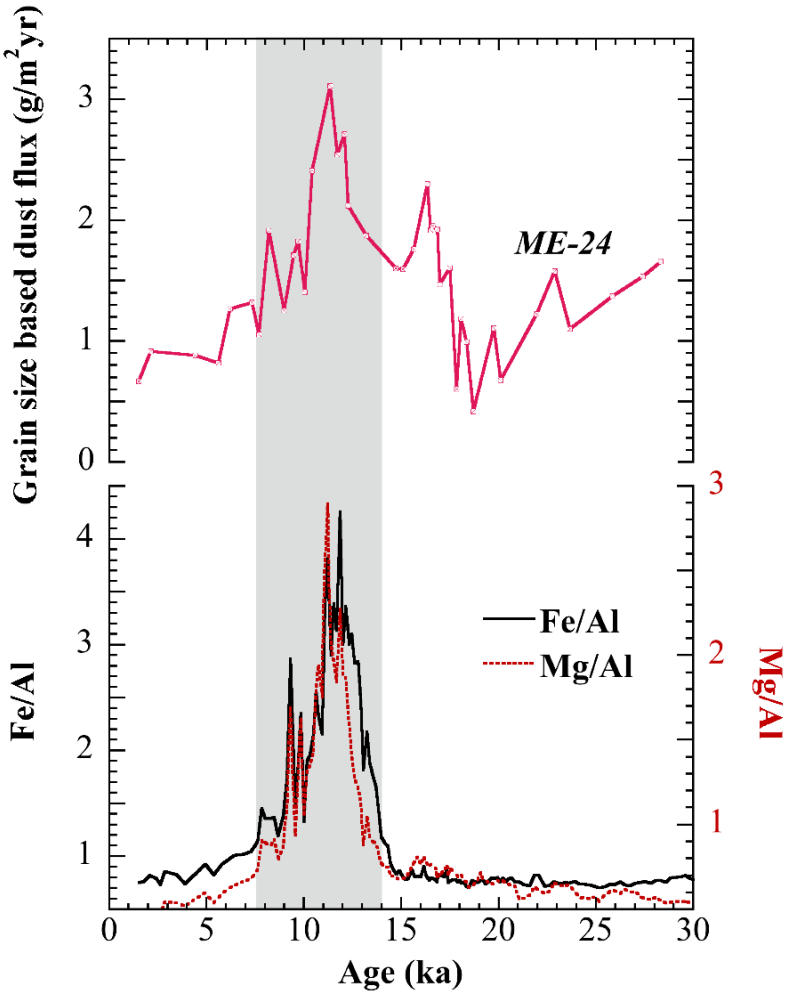


Figure 4.1: Grain size-based dust flux (pink line) with Fe/Al (black solid line) and Mg/Al (red dotted line) ratios in core ME-24 over the last 30 ka. The grey vertical bar indicates the elevated values in all three cases.

Normalizing an element to aluminum (Al) measured in the same sample gives the enrichment of the element in the sediment relative to the upper continental crust (*Calvert and Pedersen*, 2007). The Fe/Al and Mg/Al ratios in the upper continental crust are 0.44 and 0.17, respectively (Table 4.1). Compared to the crust, both basalt and hydrothermal deposits have elevated Fe/Al and Mg/Al values. ME-24 shows a clear enrichment of Fe and Mg relative to the upper continental crust between 8 - 14 ka (Figure 4.1). This implies

that during this time interval, site ME-24 was influenced by the hydrothermal deposits from the Galapagos Spreading Center. The core also shows a large 1 - 5 $\mu$m fraction between 8 - 14 ka (Figure 3.4(b)), indicating the size of the hydrothermal deposits to be similar to the dust particles. The elevated Fe/Al and Mg/Al ratios are synchronous to the elevated grain size-based dust flux in this core (Figure 4.1). The hydrothermal deposits were likely superimposed on the eolian material, thus biasing the grain size interpretation itself. This resulted in a "false" dust peak between 8 - 14 ka with the grain size-based approach that is not observed with the $^{232}$Th method.

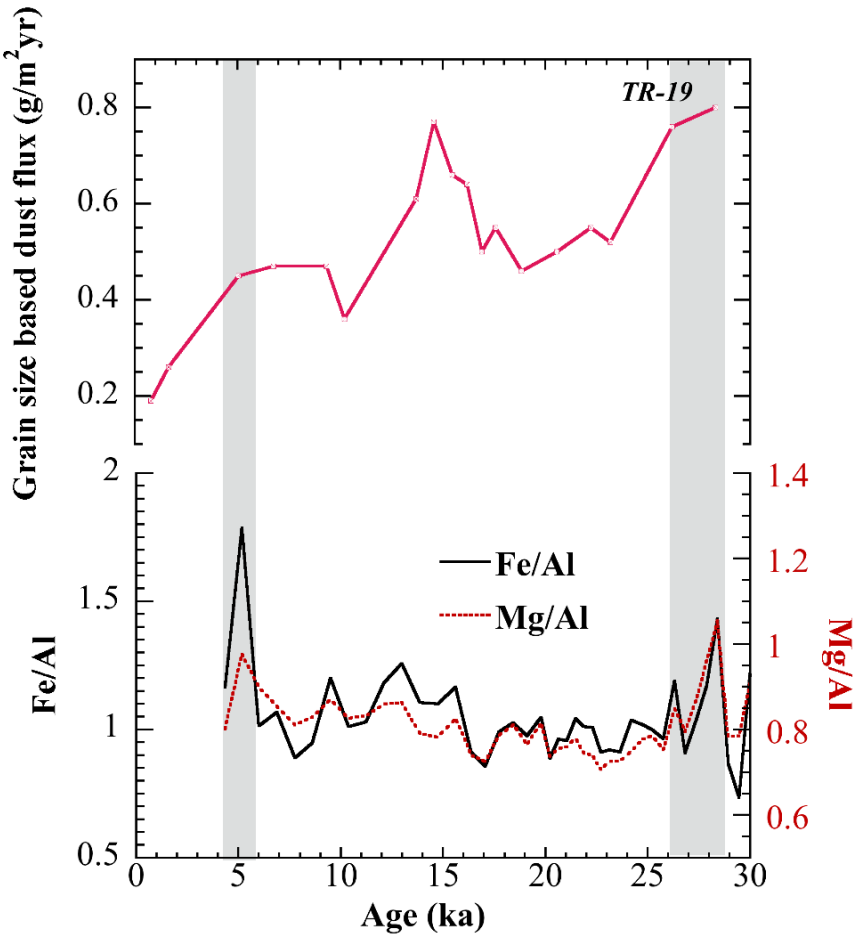


Figure 4.2: Grain size-based dust flux (pink line) with Fe/Al (black solid line) and Mg/Al (red dotted line) ratios in TR-19 over the last 30 ka. The grey vertical bar indicated the elevated values in all three cases.

Similarly, Fe/Al and Mg/Al ratios in TR-19 (Figure 4.2) are also higher than the upper continental crust and the values are closer to average basalt (Table 4.1), suggesting an additional input of volcanic basalt at this site. *Saukel et al.* (2010) classified the area close

to TR-19 as dominated by materials from submarine volcanoes. Thus, the sediment at this site may have the influence of volcanic deposits. This may indeed explain the slightly elevated dust$_{GS}$ estimates which are concurrent with the elevated Fe/Al and Mg/Al values at 5 ka and between 26 - 29 ka.

The use of two independent, but complementary proxies in environments that have multiple sediment sources, helps to produce more robust dust flux estimates. The dust$_{Th}$ estimates are not affected by hydrothermal and authigenic inputs into the sediment, and the dust$_{GS}$ estimates lessen the hemipelagic bias on the dust flux. Excluding these biases, the key features in the EEP dust flux records are (1) decreasing offshore gradient, (2) higher Last Glacial Maximum (LGM) to Holocene dust flux ratio, and (3) deglaciation dust peak. These features are discussed in Section 4.3.

## 4.2 Validation of Barite Separation Method

In the central Pacific core, almost all the depths show lower dust$_{GS}$ flux estimates after barite removal, indicating materials from the 1 - 5 $\mu$m size fraction were removed from these samples (Figure 3.10). To examine if the removed material contains barite, % changes in 1 - 5 $\mu$m fraction volume after barite removal ($\Delta$) are compared to excess barium[1] concentration (barium data from *Murray et al.*, 2000, 2012) for the same depths in PC-72 (Figure 4.3). Positive $\Delta$ values represent a decrease, and thus removal of material from the 1 - 5 $\mu$m fraction of the sediment during the separation process. However, if the coarser fraction ($>$5 $\mu$m) of sediment is removed during the process, the vol % of the 1 - 5 $\mu$m fraction will increase, resulting in a negative $\Delta$ value after barite removal. A negative $\Delta$ value (at 40 ka) is shown by the red data point in Figure 4.3. The decrease in the fraction $>$5 $\mu$m and proportional increase in the 1 - 5 $\mu$m fraction at this particular depth is also evident in Figure 3.6, 100 cm and also in Figure 3.7(b).

Figure 4.3 shows that the changes in the vol % of 1 - 5 $\mu$m fraction is correlated with the excess barium concentration of the sediment (Pearson's rho = 0.61, p-value = 0.0075). The correlation is consistent with the assumption that the particles, which are removed from the 1 - 5 $\mu$m size range during the separation procedure are mostly marine barite

[1] Excess barium, Ba$_{xs}$ (ppm) = [Ba/Al - Ba/Al$_{terrig.}$] $*$ Al (ppm)

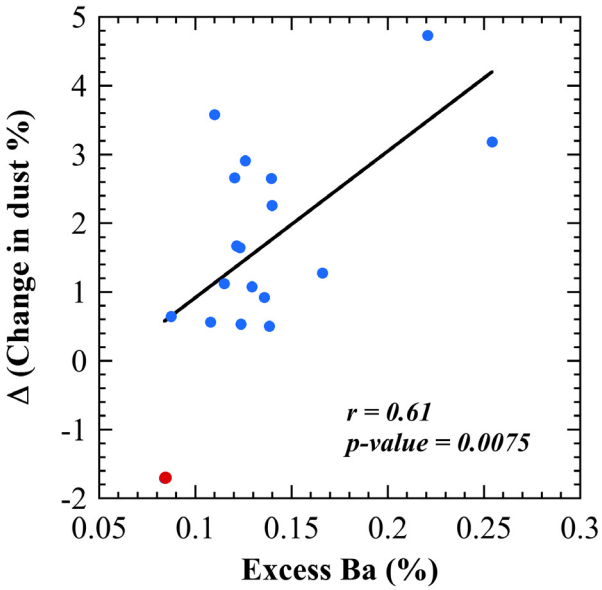


Figure 4.3: Correlation between excess Ba concentrations and $\Delta$ values (decrease in 1 - 5 $\mu$m vol %) after the removal of barite from the sediment. Both data are calculated for bulk sediment. The data point shown in red represents removal of coarser fraction (>5 $\mu$m) during the separation process thus resulting in a negative change in 1 - 5 $\mu$m fraction vol % at 40 ka. The correlation coefficient (r) was calculated using the parametric Pearson's rho. A p-value $< 0.05$ suggests the data are correlated.

crystals. However, Pearson's r of 0.61 suggests that the removed material also contained other dense particles.

The barite separation method is based on buoyancy, and therefore relies on the densities of different sedimentary components. For more consistent outcomes, it is necessary to know if denser minerals are present in the sediment, and what their densities are. Another difficulty encountered in this study during the removal process was the presence of aggregates. Disaggregating samples once they were mixed with the heavy density liquid was nearly impossible. This can lead to the removal of aggregated clay and/or dust particles stuck together with heavy minerals, causing relatively poor reproducibility in the DIGS distributions after the removal, as shown by the large error bars in Figure 3.10.

For future studies the use of liquids with a density closer to barite i.e., 4000 - 4480 kg $m^{-3}$ could also be used instead of SPT solution. One such liquid is clerici solution (equal parts thallium formate and thallium malonate) of density 4250 kg $m^{-3}$. However, care should be taken to ensure that the heavy density solution is compatible with the membrane

filter (Section 2.4.3) that is used during filtration.

## 4.3 Dust Flux in the Eastern Equatorial Pacific

The three EEP cores show similar absolute values for both $dust_{GS}$ and $dust_{Th}$ estimates and a decreasing offshore gradient (Figure 4.4). The flux estimates range from 0.2 - 0.8 g $m^{-2}$ $yr^{-1}$ in TR-19 to 0.5 - 2.29 g $m^{-2}$ $yr^{-1}$ in ME-24. *Duce et al.* (1991) estimated the flux of mineral aerosol in the EEP to be 0.1 - 1 g $m^{-2}$ $yr^{-1}$ by interpolating from a limited number of field observations in the Pacific. Similarly, *Luo et al.* (2003) estimated the mineral aerosol flux to be 0.2 - 1 g $m^{-2}$ $yr^{-1}$ in the North Pacific, and the model study by *Mahowald et al.* (2006) suggested dust fluxes of 0.2 - 0.5 g $m^{-2}$ $yr^{-1}$ in the EEP region. These values are close to both $dust_{Th}$ and $dust_{GS}$ estimates in TR-19 and $dust_{Th}$ estimates in ME-24 but slightly underestimate the $dust_{GS}$ in ME-24 (Figure 4.4). Overall, $dust_{Th}$ and $dust_{GS}$ flux estimates show regionally consistent absolute values.

### 4.3.1 Dust Fluxes During the LGM and the Holocene

In general, dust fluxes in the EEP are 1.05 - 1.65 times higher during the Last Glacial Maximum (LGM) compared to the Holocene (Table 4.2). This is consistent with previous findings in the equatorial Pacific. *Singh et al.* (2011) showed that the cores that are dominantly influenced by eolian input (cores >300 km offshore) have a glacial/Holocene ratio of $^{232}$Th flux greater than 1. The farthest core from the continent (TR163-22 at 92.4° W) showed a 2-fold increase of $^{232}$Th flux during the LGM. Similarly, *McGee et al.* (2007) also used $^{232}$Th as a proxy for eolian input along a core transect from 3°S to 7°N at 110°W and found dust fluxes to be higher by a factor of 1.25 - 2 during the LGM compared to the Holocene. Further west at 140°W, *Anderson et al.* (2006) and *Winckler et al.* (2008) also found higher dust fluxes by a factor of 2 during the LGM. Note that their core (PC-72) was also used in this thesis. A comparison between $^{232}$Th derived dust flux (*Anderson et al.*, 2006; *Winckler et al.*, 2008) and grain size-based dust flux (this thesis) is presented later in this chapter (Section 4.4). Together, the results of all these studies and the findings from this thesis, clearly indicate that the glacial dust flux was higher (by a factor of $\sim$2) compared to the Holocene in the equatorial Pacific region.

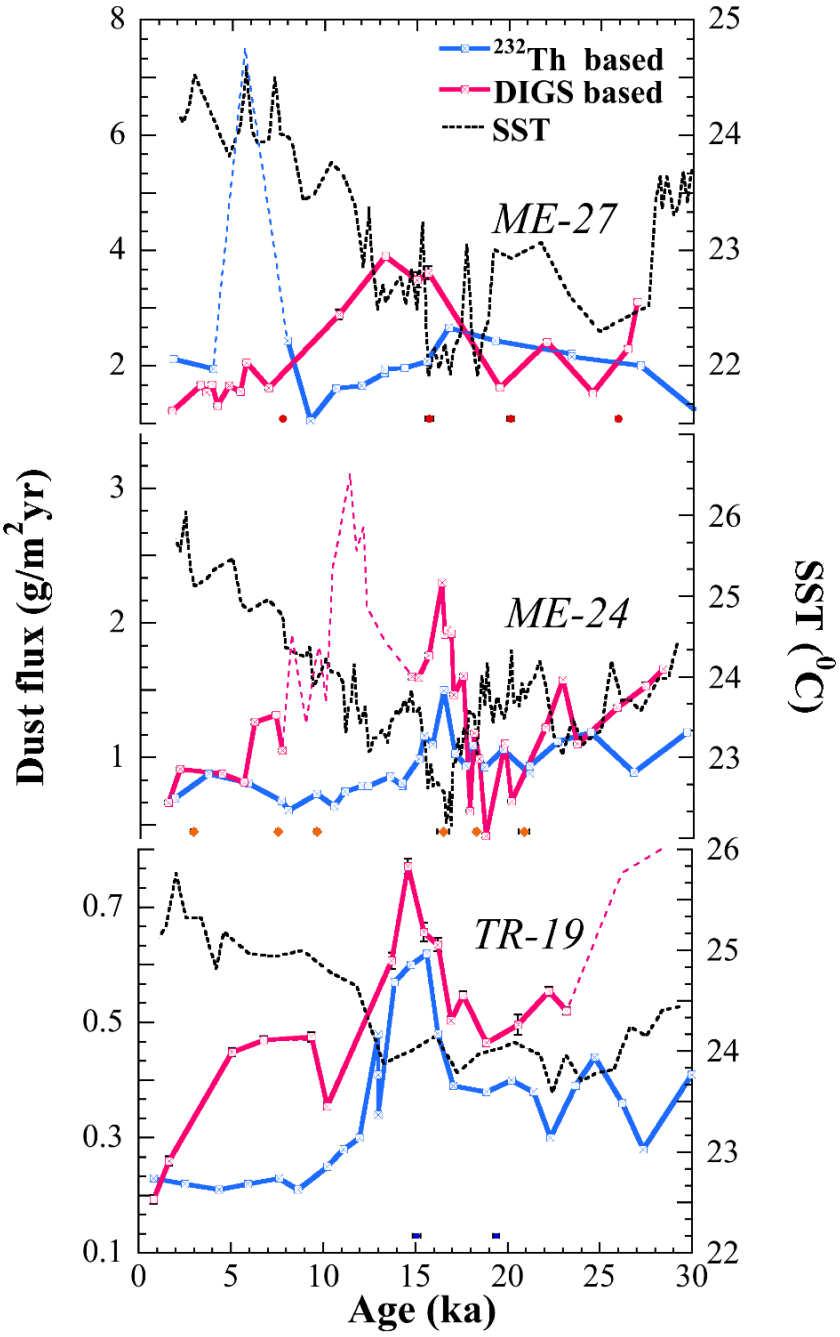


Figure 4.4: $^{232}$Th-based (blue) and grain size-based (pink) dust fluxes plotted with sea surface temperature (dashed black lines) over the last 30 ka in the EEP cores. Dashed colored lines give the dust flux values influenced by hemipelagic materials (in ME-27) and hydrothermal deposits (in ME-24 and TR-19). The radiocarbon dates for each core are shown as blue boxes (TR-19), orange diamonds (ME-24), and red dots (ME-27). Note the different y-axis for different panels.

Table 4.2 provides dust$_{Th}$, dust$_{GS}$ (this thesis), and model (*Jickells et al.*, 2005; *Mahowald et al.*, 2006; *Albani et al.*, 2014) estimates for the LGM and Holocene dust flux. These dust flux estimates are comparable within an order of magnitude for the LGM as well as the Holocene. However, the decreasing LGM-Holocene dust flux trend clearly seen in the EEP cores is not reproduced by the model (CCSM3, *Mahowald et al.*, 2006). At all three sites, the model shows higher flux in the Holocene compared to the LGM (Table 4.2).

Even though there have been significant improvements in numerical simulations of the global dust cycle, there are still large uncertainties within the models and differences between their outputs (e.g., *Mahowald et al.*, 1999; *Luo et al.*, 2003; *Jickells et al.*, 2005; *Mahowald et al.*, 2006). More recent simulations are now able to capture the overall magnitude and spatial variability of the dust cycle but still contain big uncertainties (*Jickells et al.*, 2005; *Mahowald et al.*, 2006; *Albani et al.*, 2014). This is due, in part, to gaps in observational data. The dust flux records presented in this thesis confirms the regional dust flux estimates in the equatorial Pacific. At the same time, these results also support the decreasing LGM-Holocene trend that is seen globally, but not yet captured by the model (*Mahowald et al.*, 2006).

### 4.3.2 Dust Flux During the Deglaciation

Dust$_{Th}$ and dust$_{GS}$ show elevated values during the deglaciation in TR-19 and ME-24 (Figure 4.4). The deglacial dust peak in ME-24 appears to lead the peaks in TR-19 by $\sim$1.8 ka. The maximum 1$\sigma$ error in the radiocarbon age models in that time interval is $\pm$0.32 ka, which is not sufficient to explain the apparent 1.8 ka lead. However, the lack of temporal resolution, especially in TR-19, makes the interpretation of temporal lead and lag of dust fluxes ambiguous. Given the proximity of these cores, the elevated deglacial dust flux could be synchronous.

The higher dust fluxes during the deglaciation in the EEP cores are consistent with the finding of *Kienast et al.* (2013) where the authors observed an increased flux of the continental isotope ($^{232}$Th) between 15 - 18 ka. *McGee et al.* (2013) examined the cores from the northwest African margin to estimate North African dust flux over the last 20 ka. The study used the same grain size approach to derive dust flux as presented in this thesis. The authors found that dust flux reached its maximum (6 g cm$^{-2}$ ka$^{-1}$) during

Table 4.2: $^{232}$Th and grain size-based dust fluxes (g m$^{-2}$ yr$^{-1}$) from this thesis and different model estimates (g m$^{-2}$ yr$^{-1}$) during the Holocene (core top - 11 ka) and the LGM (18 - 23 ka). The $^{232}$Th and grain size-based dust fluxes are averaged over the time interval and the associated standard derivation is also given.

| **Source of flux estimates** | **ME-27** | **ME-24** | **TR-19** | **PC-72** |
|---|---|---|---|---|
| | **Holocene** | | | |
| $^{232}$Th | $1.84 \pm 0.53$<br>*$2.78 \pm 2.36$*[‡] | $0.72 \pm 0.09$ | $0.22 \pm 0.01$ | $0.17 \pm 0.01$ |
| DIGS | $1.72 \pm 0.47$ | $0.98 \pm 0.24$<br>*$1.34 \pm 0.51$*[*] | $0.37 \pm 0.12$ | 0.27[§] |
| CCSM3-SOMB[a] | 1.69 | 0.89 | 0.86 | 0.29 |
| Composite [b] | 0.152 | 0.203 | 0.18 | 0.123 |
| CESM1-C4fn [c] | 1.025 | 0.863 | 1.114 | 0.085 |
| | **LGM** | | | |
| $^{232}$Th | 2.44[†] | $1 \pm 0.1$ | $0.37 \pm 0.04$ | $0.35 \pm 0.03$ |
| DIGS | $2.02 \pm 0.56$ | $1.03 \pm 0.38$ | $0.51 \pm 0.05$ | $0.36 \pm 0.02$[§] |
| CCSM3-SOMB[a] | 1.24 | 0.73 | 0.63 | 0.336 |

[‡] Including the one high value (7.5 g m$^{-2}$ yr$^{-1}$) of $^{232}$Th dust flux at 5.6 ka.
[*] Including the grain size dust flux influenced by the hydrothermal input. For more information see Section 4.1.
[§] Dust$_{GS}$ after the removal of barite. Holocene dust$_{GS}$ has only one data point.
[†] Only one data point during the LGM.
[a] *Mahowald et al.* (2006). Holocene values represent the modern dust flux.
[b] Composite model based on several dust models (*Jickells et al.*, 2005).
[c] *Albani et al.* (2014)

Heinrich Stadial 1 (HS-1, 15 - 18 ka). North Africa is one of the major dust sources into the atmosphere and is assumed to be one of the distal dust source regions for the EEP (*Luo et al.*, 2003; *Mahowald et al.*, 2011; *Xie and Marcantonio*, 2012). There is good agreement between increased dust flux in the EEP and the North African source area (*McGee et al.*, 2013) during HS-1. Dust flux in marine sediments is a function of wind strength, distance from the source region and the extent of the source region (*Kohfeld and Harrison*, 2001). Thus, higher dust fluxes during the deglaciation suggest enhanced atmospheric circulation and/or more active dust source areas.

*Prospero and Bonatti* (1969) and *Saukel et al.* (2010) assigned North, Central and South America as major proximal dust source regions to the EEP. Isotope and model studies have suggested that North Africa, China, and possibly even Australia are distal dust sources to the EEP (*Luo et al.*, 2003; *Mahowald et al.*, 2011; *Xie and Marcantonio*, 2012). The increased dust loading in the EEP during HS-1 indicates that these source areas generated more dust. Indeed, studies based on lake sediments, pollen, and gypsum deposits at various sites have shown that the northern hemisphere was drier during HS-1 (e.g., *Peterson et al.*, 2000; *Mulitza et al.*, 2008; *Escobar et al.*, 2012; *McGee et al.*, 2013; *Gibbons et al.*, 2014). The coupling of drier source regions with increased trade winds during the early deglaciation (*Zhang and Delworth*, 2005; *Timmermann et al.*, 2007) could have resulted in higher dust loads in the EEP. Furthermore, studies with various paleo-proxies have shown that there was a latitudinal displacement of the Inter Tropical Convergence Zone (ITCZ) over time (e.g., *Peterson et al.*, 2000; *Escobar et al.*, 2012; *Kienast et al.*, 2013; *Gibbons et al.*, 2014; *McGee et al.*, 2014, and references therein). According to these authors, the ITCZ was at its southern-most position during HS-1. In the EEP, the migration of the ITCZ south of the equator during this period would place the three cores north of the ITCZ, subjecting them to higher northern hemisphere dust loads.

Previous studies on dust fluxes in the EEP have relied only on $^{232}$Th measurements. Furthermore, the deglacial dust peak has only been observed in one study (*Kienast et al.*, 2013) so far in this region. This thesis is the first study to combine two independent approaches (dust$_{Th}$ and dust$_{GS}$) to derive dust flux and confirms the increased deglacial dust flux in the EEP.

## 4.4 Dust Flux in the Central Equatorial Pacific

Overall, the absolute values of the dust$_{GS}$ are comparable with the dust$_{Th}$ in the central Pacific core PC-72 (*Winckler et al.*, 2008), particularly in the second cycle (Figure 4.5). However, dust$_{GS}$ and dust$_{Th}$ show divergent trends over the two G-IG cycles. The dust$_{Th}$ estimates consistently show maxima in glacial periods ($\sim$0.4 g m$^{-2}$ yr$^{-1}$) suggesting a dustier glacial period. However, ignoring the value at 40 ka, where high dust flux maybe an artifact from the barite separation method (see Section 4.2), the dust$_{GS}$ shows the highest

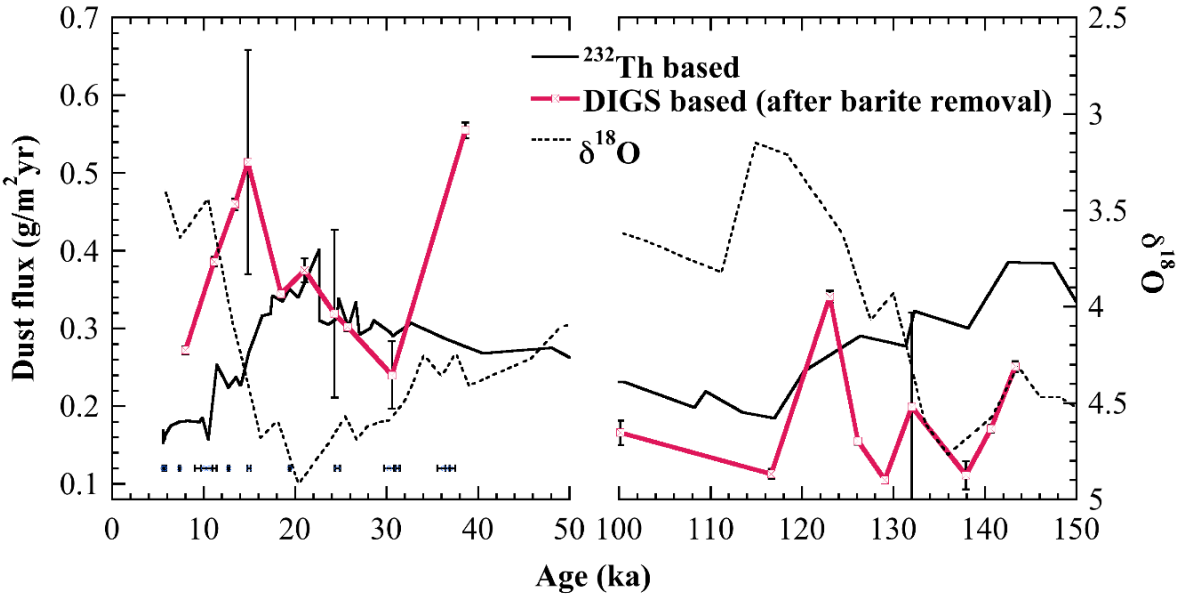


Figure 4.5: Grain size-based dust flux (pink solid line) compared with the $^{232}$Th-based dust flux (black solid line) (*Winckler et al.*, 2008) over the last two glacial-interglacial cycles in the central Pacific core PC-72. Oxygen isotope data (black dashed line) (*Murray et al.*, 2000, 2012) are shown for reference.

flux during the transition periods.

The dust$_{GS}$ estimates in the central Pacific (Figure 4.5) observed in this thesis are different from those in other studies. Along with the $^{232}$Th-based dust flux by *Winckler et al.* (2008), model studies (*Mahowald et al.*, 2006; *Luo et al.*, 2003) also report higher dust fluxes during the LGM (Table 4.2). The possible reasons for the divergence of dust$_{GS}$ estimates from other studies in the central Pacific could be due to the assumption made in this thesis that (1) the dust in the central Pacific is between 1 - 5 $\mu$m, and (2) sediments in the 1 - 5 $\mu$m fraction size range at this core site are solely from wind derived sources. Based on the remoteness of the core site it is possible, but unlikely, that eolian particles reaching this location are >5 $\mu$m in size. *Anderson et al.* (2006) indicated that the principle source of lithogenic material in the central equatorial Pacific is eolian but also suggested that the Equatorial Undercurrent (EUC) possibly serves as an additional source (*Coale et al.*, 1996; *Wells et al.*, 1999). The lithogenic particles transported by the EUC superimposed on the eolian dust could change the inventory of fine grains in the sediment, thus affecting dust$_{GS}$ flux estimates at this core site. Still, the large uncertainty in the dust$_{GS}$ estimates comes from the error associated with the barite separation method. Given the large error due to

poor DIGS distribution reproducibility as well as insufficient temporal resolution of the data, a concrete conclusion cannot be drawn at this point. As discussed in Section 4.2, the barite separation method requires further development to become a more robust technique.

## 4.5 Focusing Factor and Sorting Coefficient

The focusing factor quantitatively estimates the extent of sediment redistribution on the sea floor either by sediment focusing (addition of sediment to a site) or by sediment winnowing (removal of material from a site). It is a geochemical approach based on the assumption that the flux of scavenged $^{230}Th_{xs,0}$ to the sea floor is equal to its production rate in the overlying water column. If there is no lateral redistribution of the sediment on the sea floor then the accumulation of excess $^{230}$Th relative to its production is 1 (*Suman and Bacon*, 1989; *Francois et al.*, 2004). This approach is discussed in more detail in Section 2.8.6.

In contrast, the sorting coefficient estimates the degree of sediment sorting using the inorganic grain size distribution of the sediment. A higher coefficient indicates a lower degree of sorting while a lower sorting coefficient shows a higher degree of sorting in the sediment. This is because a better sorted sediment has less variability within the grain size. Sediment sorting occurs hydrodynamically during resuspension, transportation and deposition (*McCave et al.*, 1995). Thus, the degree of sorting in the sediment indicates the extent of lateral redistribution on the sea floor due to bottom currents.

Figures 3.11 and 3.13 show the sorting coefficients and focusing factors, respectively, for the three EEP cores. The sorting coefficients are averaged over three time intervals (core top - 11, 11 - 18, and 18 - 30 ka roughly corresponding to the Holocene, transition and glacial period). The average sorting coefficients during the glacial period show lower values compared to the Holocene, implying better sediment sorting during this period. This suggests that sediments during the glacial period are more laterally transported than during the Holocene. The focusing factors also show higher values during the glacial period, illustrating a higher accumulation of excess $^{230}$Th compared to its production. This indicates that sediments were laterally transported to this site from surrounding areas during the glacial period. In addition, TR-19 shows a good agreement between the highest sorting coefficient and the lowest focusing factor during the transition period (Figures 3.11

and 3.13). Similarly, ME-24 has the lowest sorting coefficient and the highest focusing factor during this period. However, ME-27 shows opposite results for the sorting coefficient and focusing factor during the transition period.

The sorting coefficient and the focusing factor approaches are two independent proxies for estimating lateral sediment redistribution and mostly provide similar results across the three time intervals (Figure 3.11 and 3.13). However, averaging the sorting coefficients over a time interval gives large errors because of the variability in values within the interval (Figure 3.11). As a result, the averaged sorting coefficients are not significantly different between the three different time intervals.

For better comparison, smaller time intervals were used. In addition to the three time intervals (core top - 11, 11 - 18, and 18 - 30 ka), the focusing factor was also calculated between each consecutive depth using Equation 2.11 and compared with the sorting coefficient value for each depth (Figure 4.6). For these shorter time intervals, the focusing factor and sorting coefficients again show similar trends. Depths showing more sorted sediment (smaller sorting coefficient) match with the depths for which higher focusing factors were calculated.

The correlation between sorting coefficients and focusing factors for each core were examined using Pearson's rho. The scatter plots for each core with respective correlation coefficients (r) and p-values are shown in Figure 4.7. Sorting coefficients and focusing factors are negatively correlated in TR-19 (r = -0.58, Figure 4.7(a)) and ME-24 (r = -0.62, Figure 4.7(b)). ME-27, however, does not show a correlation between sorting coefficient and focusing factor (r = -0.28, Figure 4.7(c)). ME-27 has the smallest range in sorting coefficients and focusing factor (Figure 4.6) and, importantly, the smallest overall focusing factor of all EEP cores (Figure 3.13). Given this small range and the dependence of focusing factors on the age model, the lack of correlation between sorting coefficients and focusing factors in ME-27 is likely not meaningful.

For consistency with the published literature, focusing factors for the EEP cores presented in *Kienast et al.* (2007), which used slightly different time intervals are recalculated in the Appendix C using the latest age model (see Section 2.3).

Note also that the divergence between focusing factor and sorting coefficient values

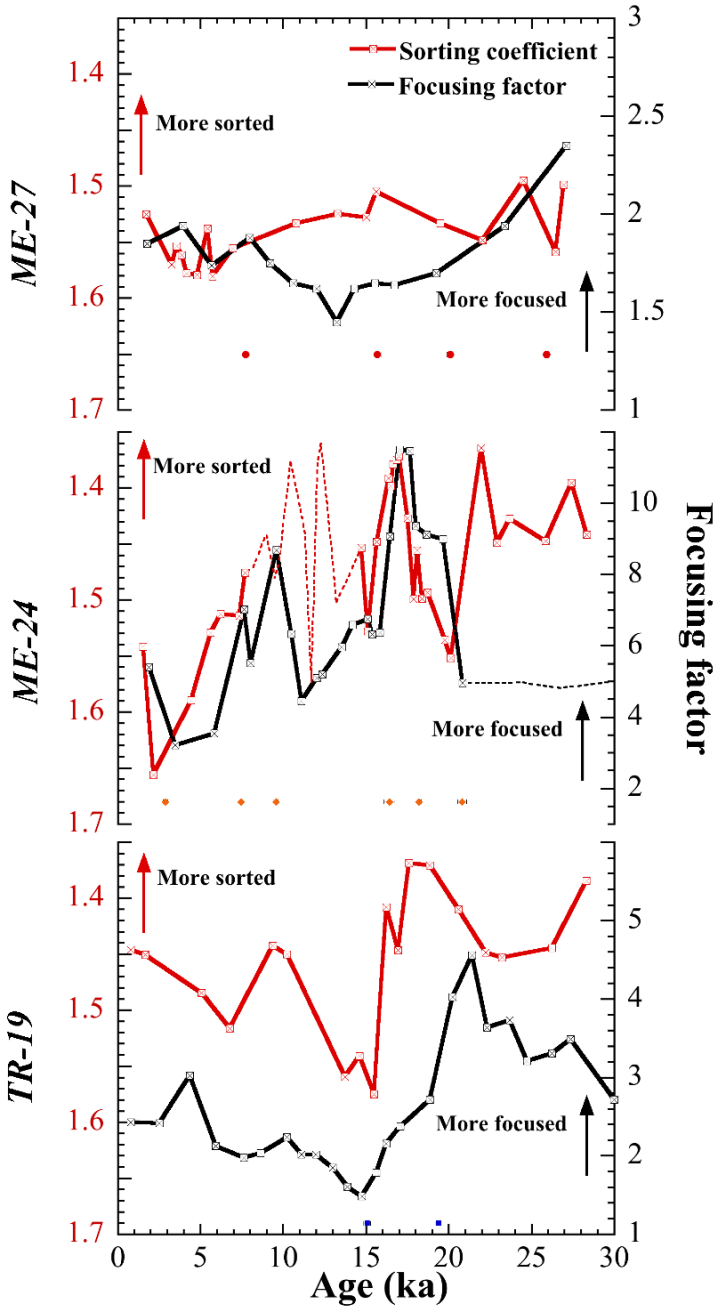


Figure 4.6: Sorting coefficients in 10 - 63 $\mu$m grain size range calculated using geometric method of moments along with the focusing factors for the three EEP cores over the last 30 ka. Y-axis for sorting coefficients are reversed showing more sorted sediment with lower values. The dotted lines represent the data influenced by hydrothermal input (8 - 14 ka, red) and age model (20 - 30 ka, black). The radiocarbon dates for each core are shown as blue boxes (TR-19), orange diamonds (ME-24), and red dots (ME-27). Note the different y-axis for focusing factor.

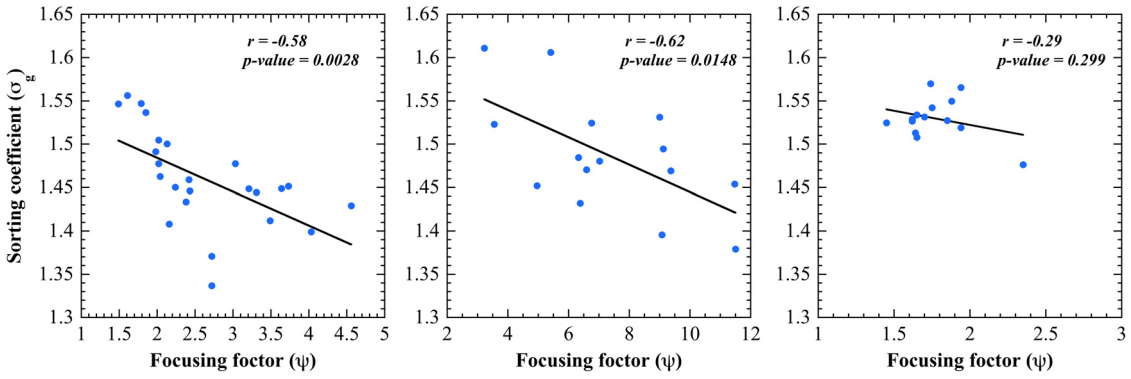


(a) TR-19 (b) ME-24 (c) ME-27

Figure 4.7: Correlation between sorting coefficients and focusing factors in the EEP cores. The correlation coefficients (r) were calculated using the parametric Pearson's rho. A p-value $< 0.05$ indicates that the data are correlated with each other. The data for ME-24 exclude the depths influenced by hydrothermal inputs (8 - 14 ka) and depths after 20 ka.

after 21 ka in ME-24 could easily be due to the age model uncertainty and radiocarbon age constraints in this core. The last radiocarbon date in ME-24 is at 20.79 ka and the next tie point is at 38.9 ka with the $\delta^{18}O_{ice}$ EPICA Dronning Maud Land (EDML) record from Antarctica (*Dubois et al.*, 2011). The interval between 20.79 and 38.9 ka could provide a large age uncertainty in the age-depth relationship thus influencing focusing factor values older than 20 ka. Even with the uncertainty concerning the age model, the focusing factor and sorting coefficient trends are in relatively good agreement for the EEP cores (Figure 4.7).

Contrary to the EEP cores, the focusing factors and the sorting coefficients do not show any correlation in the central Pacific core (Figure 3.12 and 3.14). Even when the focusing factor is calculated for smaller intervals, there is no correlation with the sorting coefficient values (Figure 4.8). This is true for values both before (r = -0.42, Figure 4.9(a)) and after barite removal (r = 0.12, Figure 4.9(b)). The disagreement between sorting coefficient and focusing factor in the central Pacific core could be due to the small contribution of sortable silt (10 - 63 $\mu$m) fraction in this core. The sorting coefficient is calculated within the sortable silt size range because the grains in this size range is most likely to be affected by bottom current(s) (*McCave et al.*, 1995). Compared to the carbonate rich bulk sediment (80 - 90 %), the sortable silt fraction is insignificant ($<$3 %) and thus, the sorting coefficient calculated within this small fraction may not be a good proxy for bottom current induced

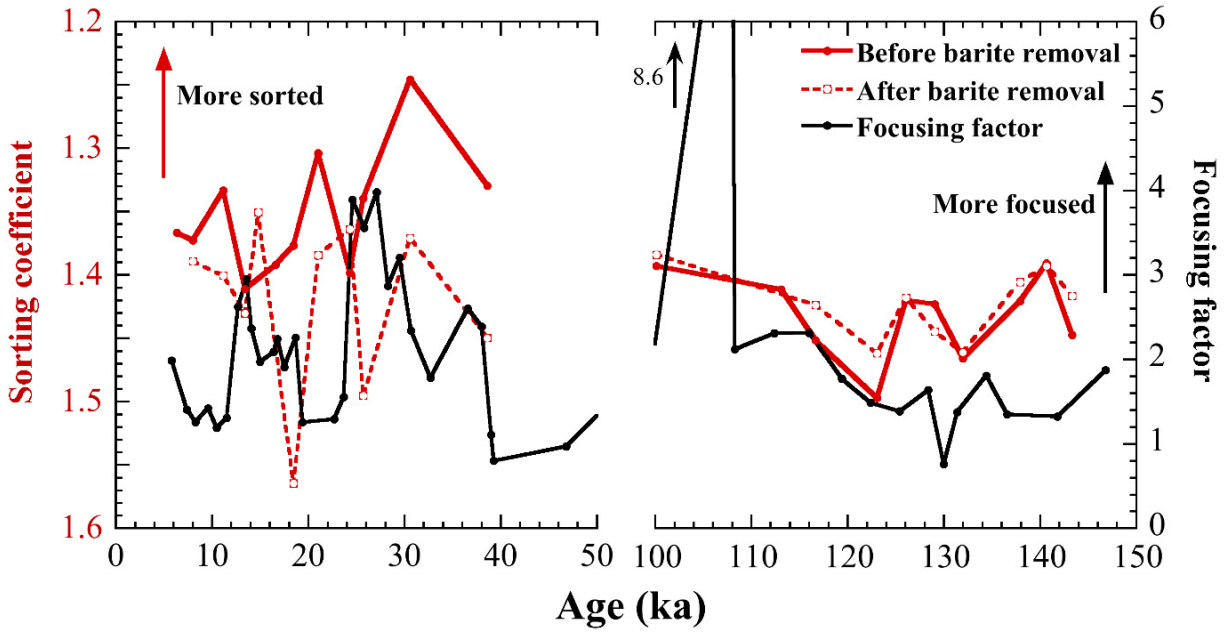


Figure 4.8: Sorting coefficients in 10 - 63 $\mu$m grain size range calculated using geometric method of moments (red lines) along with the focusing factors (black line) for PC-72 over the two glacial-interglacial cycles. Y-axis for sorting coefficient is reversed showing more sorted sediment with lower values. Red solid line shows the sorting coefficient before the barite removal and red dotted line shows the coefficient after the barite removal.

sediment sorting in this region.

## 4.6 Implication of Sediment Sorting on the Focusing Debate

The paleoceanographic community has known about syndepositional sediment redistribution in the equatorial Pacific for some time (e.g., *Loubere et al.*, 2004; *Francois et al.*, 2004; *Lyle et al.*, 2005; *Kienast et al.*, 2007; *Siddall et al.*, 2008; *Singh et al.*, 2011). Sediment redistribution on the sea floor from areas of sediment winnowing to areas of sediment focusing leads to higher apparent mass accumulation rates (MARs) and hence inaccurate vertical flux estimates. Normalization to $^{230}$Th (Section 1.2.2) is becoming an increasingly used approach to more accurately estimate vertical flux by eliminating the effect of sediment redistribution. However, there has been a good deal of controversy regarding the validity of the $^{230}$Th normalization technique (e.g., *Lyle et al.*, 2005; *Francois*

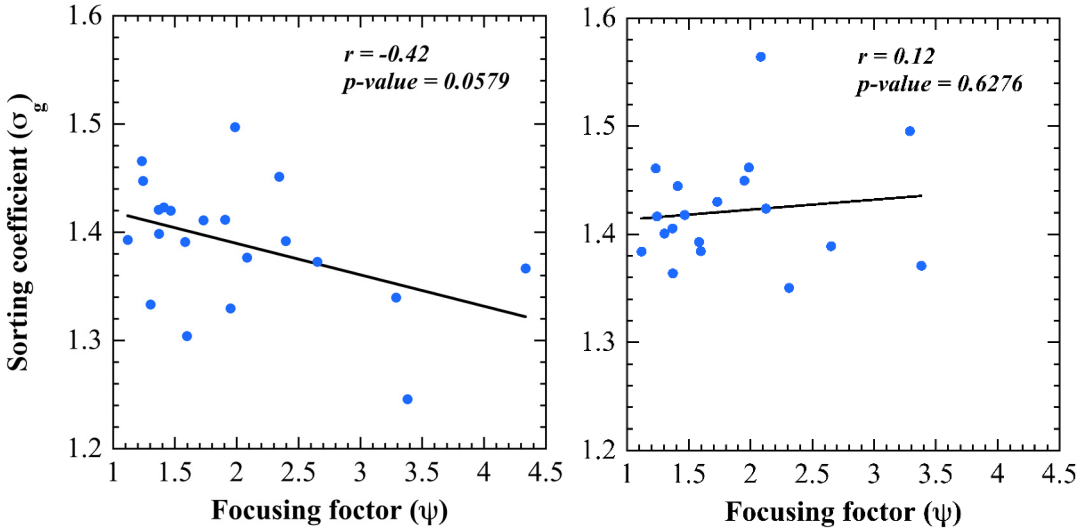


(a) Before barite removal (b) After barite removal

Figure 4.9: Correlation between focusing factors and sorting coefficients before (a) and after (b) barite removal in the central Pacific core. The correlation coefficients (r) were calculated using the parametric Pearson's rho. P-value $> 0.05$ indicates that the data are not correlated to each other.

*et al.*, 2007; *Broecker*, 2008).

Studies opposed to the normalization method (*Lyle et al.*, 2005, 2007; *Broecker*, 2008) argue that higher accumulation of excess $^{230}$Th is not due to sediment redistribution on the sea floor but instead to the preferential removal of dissolved $^{230}$Th in areas of high particle flux such as the equatorial Pacific. The removal of dissolved $^{230}$Th at a given location promotes the addition of $^{230}$Th from areas of lower particle flux by diffusion. These authors argued that the excess $^{230}$Th deposition in the equatorial belt is likely due to the result of water column scavenging rather than along bottom sediment transport.

Studies supporting the $^{230}$Th normalization method (e.g., *Marcantonio et al.*, 2001; *Francois et al.*, 2004, 2007; *Kienast et al.*, 2007) suggest syndepositional lateral sediment transport on the sea floor as the reason for higher observed MARs in EEP. *Kienast et al.* (2007) found that at some sites in the EEP, sediment accumulation is 5 - 8 times higher than its vertical flux. *Singh et al.* (2013) measured the dissolved $^{230}$Th concentration and its lateral transport between the Guatemala, Peru and Panama Basins in the EEP. The authors found that about 15 - 30 % of the total inventory of dissolved $^{230}$Th in Panama Basin is advected from the Peru Basin. This however, can only explain focusing factors up to 1.3

in Panama Basin (*Singh et al.*, 2013). Evidence of sediment focusing in the equatorial Pacific was also provided by *Dubois and Mitchell* (2012). The authors looked at digital seismic profiles across the eastern-central Pacific and found large scale sediment anomalies in sediment thickness, pointing to bottom-current induced sediment resuspension and deposition.

Disaggregated inorganic grain size (DIGS) distribution is a completely independent proxy and can shed new light on the focusing debate. Sorting in the 10 - 63 $\mu$m size range occurs during lateral sediment transport due to bottom currents (*McCave et al.*, 1995; *McCave and Hall*, 2006). Overall, there is relatively good agreement between the degree of sediment sorting represented by the sorting coefficients and the focusing factors derived from $^{230}$Th measurements in the EEP cores (TR-19 and ME-24, Figures 4.6 and 4.7). This suggests that more focused sediment is indeed better sorted. According to the sorting coefficients, the sediments are moderately to well sorted. Taken together, these lines of evidence support the notion that syndepositional sediment redistribution occurs in the EEP. The results from this thesis thus support the idea of sediment redistribution on the sea floor and provide further validity to the $^{230}$Th normalization method.

There have been limited studies of bottom currents (*Johnson and Johnson*, 1970; *Gardner et al.*, 1984; *Marcantonio et al.*, 2001) or current induced resedimentation in the equatorial Pacific (*Dubois and Mitchell*, 2012). This thesis is the first step towards understanding the issue of sediment focusing using grain size properties of the sediment. Unfortunately, this method encounters problem in the regions of high carbonate content. Therefore, using the inorganic grain size properties of the sediment at these sites does not provide a more concrete result to explain sediment redistribution. However, this study provides a baseline for future grain size-based work in highly productive areas with dynamic depositional environment.

# CHAPTER 5

# CONCLUSIONS

The equatorial Pacific has been an area of great interest for oceanographic and paleoceanographic studies for many years. However, not much is known about the present or paleo-dust fluxes in this region. The sparsity of dust flux data from the equatorial Pacific has contributed to the uncertainties in modeling the global dust cycle with coupled climate models. Furthermore, the equatorial Pacific is at the focus of a current controversy regarding sediment focusing on the sea floor in this region.

The grain size distribution of sediment is useful in deriving information about its sources as well as the environmental conditions during the time of its deposition. Disaggregated inorganic grain size (DIGS) distributions of equatorial Pacific sediments were analyzed in this thesis (1) to estimate dust fluxes and (2) to examine sediments for evidence of bottom-current induced size sorting. Three cores from the eastern equatorial Pacific (EEP) region (82°W - 90°W) and one core from the central Pacific (140°W) were used in this thesis, covering 0 - 30 and 0 - 150 ka, respectively. Grain size-based dust fluxes were quantified for each core using end member modeling that isolates the 1 - 5 $\mu$m fraction (considered dust) from coarser silts, and by multiplying this fraction with the $^{230}$Th derived bulk flux. These estimates were then compared with $^{232}$Th-based dust fluxes, $^{232}$Th being a proxy for detrital continental material.

Furthermore, based on the different densities of barite and siliciclastic sediment, a new method was developed in this study for separating authigenic barite from sediments. This method was carried out on the central Pacific core to examine the potential bias of barite

on grain size-based dust flux.

Grain size and $^{232}$Th are two independent approaches for estimating the paleo-dust fluxes. Both approaches show highest dust fluxes in the EEP during the glacial-interglacial transition period. Unlike some of the previous studies, a dust flux maximum is not observed during the Last Glacial Maximum (LGM). However, both grain size and $^{232}$Th-based estimates show higher dust fluxes during the LGM compared to the Holocene. This strongly suggests that models, which show higher Holocene dust flux at these sites, do not yet obtain correct sign for the LGM-Holocene dust flux change. The results of this thesis show that $^{232}$Th-based dust fluxes and grain size-based dust fluxes largely complement each other in the EEP region. However, the equatorial Pacific is a dynamic sedimentary environment receiving sediments from eolian, hemipelagic, hydrothermal and submarine volcanic sources. Thus, the episodic input of hemipelagic (in ME-27) and hydrothermal materials (in ME-24 and TR-19) leads to apparent overestimates of $^{230}$Th-based and grain size-based dust fluxes, respectively, and causes the divergence between these two approaches at certain time intervals.

The sediments from the EEP cores are moderately to well sorted, implying that there was indeed along-bottom sediment transport that resulted in size selective sorting. The relatively good agreement between the focusing factor and sorting coefficient (i.e., a more sorted sediment also shows a higher focusing factor) suggests that lateral sediment redistribution on the sea floor, and not scavenging of dissolved $^{230}$Th from the water column, is the cause of higher accumulation of excess $^{230}$Th in the sediment. This supports the validity of the $^{230}$Th normalization method for the particle flux reconstruction in the eastern equatorial Pacific.

Contrary to the EEP, the central Pacific core neither shows similar glacial-interglacial trends in grain size and $^{232}$Th-based dust fluxes, nor shows a correlation between sorting coefficients and focusing factors. The divergence in dust fluxes could be because of the assumption (made in this study) that eolian dust reaching this location is between 1 - 5 $\mu$m in size. Even though it is unlikely that particles larger than 5 $\mu$m reach the central Pacific, there is a possibility that coarser grains get transported to this location. This site could also have other lithogenic or authigenic sources that contribute to the $<$5 $\mu$m fraction of the sediment, and the barite separation method did not fully work and requires further study.

Central Pacific sediments are dominated by carbonates (80 - 90 % of the bulk sediment) and only $<$3 % of the bulk sediment is between 10 - 63 $\mu$m in size. Thus, using this size fraction may not be the best approach to estimate lateral sediment redistribution in the central Pacific.

Overall, sediment DIGS distribution has been found to be a useful tool in understanding sedimentary sources and depositional processes in the deep sea. Additionally, this thesis is the first ever to provide DIGS downcore study in the EEP.

# APPENDIX A

# BARITE SETTLING VELOCITY

Stokes' law states that a particle falling under its own weight will reach its terminal (settling) velocity when the gravitational force is balanced by the buoyancy and drag force on the particle. The terminal velocity of the particle is given by

$$v = \frac{d^2 g(\rho_s - \rho_l)}{18\mu} \tag{A.1}$$

where $v$ is the settling velocity (m $s^{-1}$), $d$ is the diameter of the particle (m), $g$ is the gravitational acceleration (9.8 m $s^{-2}$), $\rho_s$ is density of the particle (kg $m^{-3}$), $\rho_l$ is density of the fluid (kg $m^{-3}$), and $\mu$ is the dynamic viscosity of the fluid (kg $m^{-1}$ $s^{-1}$).

Using Equation A.1, the settling velocity of a barite crystal in a heavy density liquid can be calculated. The diameter of the barite crystal is assumed to be 2 $\mu m$ with a density of 4490 kg $m^{-3}$. The heavy density liquid (sodium polytungstate) has a density of 2890 kg $m^{-3}$ and dynamic viscosity of 26 mPa.s (0.026 kg $m^{-1}$ $s^{-1}$). Thus, the settling velocity of a barite crystal is

$$v = \frac{(2 \times 10^{-6})^2 \times 9.81 \times (4490 - 2890)}{18 \times 0.026}$$
$$v = 1.34 \times 10^{-7} m\ s^{-1} \tag{A.2}$$

In a 9 cm long test tube, a barite crystal would take about 7.77 days to settle to the bottom. To speed up the settling velocity of the barite particles, a centrifuge was used.

Centrifuging significantly increases the downward force by replacing the acceleration due to gravity ($g$) in Equation A.1 with the centrifugal force ($CF$). The centrifuge used for this project has a centrifugal force of 2700$\times$ $g$ at 4000 RPM. This increases the settling velocity of barite particles to

$$v = \frac{(2 \times 10^{-6})^2 \times 2700 \times 9.81 \times (4490 - 2890)}{18 \times 0.026}$$
$$v = 3.62 \times 10^{-4} m\ s^{-1} \tag{A.3}$$

The use of a centrifuge thus decreases the settling time for barite particles to 4.14 minutes. To make sure that all the particles are separated, the centrifugation time was increased to 10 minutes. Increasing the time to more than 10 minutes tends to break the test tubes, resulting in a loss of sample.

# APPENDIX B

# SEM IMAGES

## B.1 Laboratory Standard 1

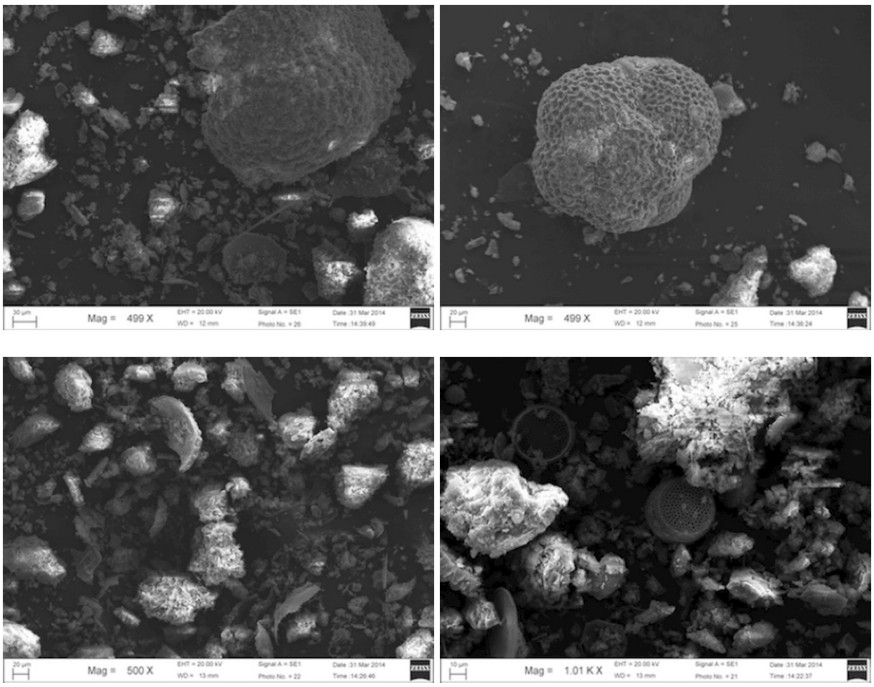


Figure B.1: SEM images of the freeze dried Standard 1 bulk sediment at different magnification.

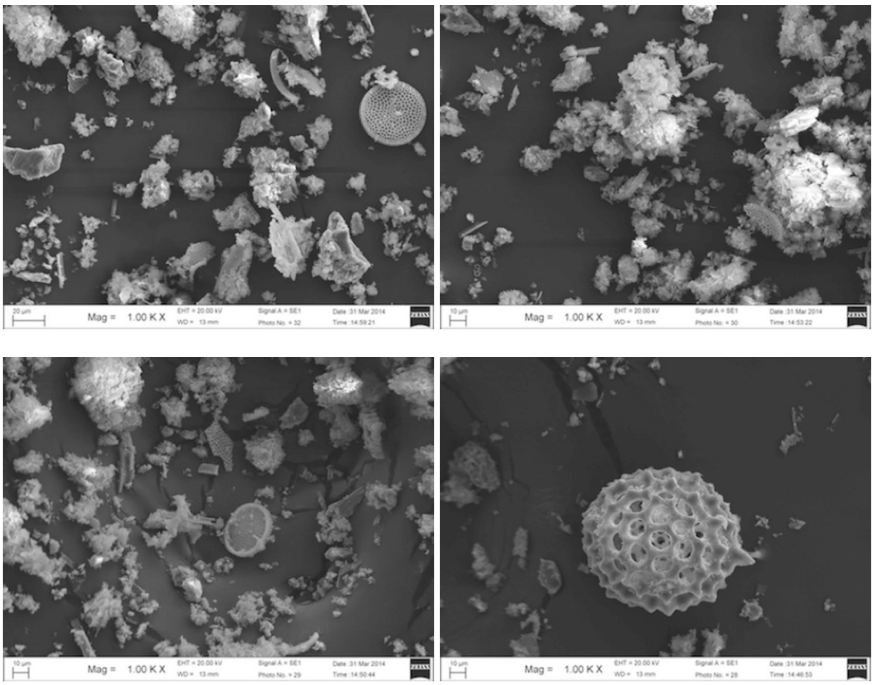


Figure B.2: SEM images of Standard 1 from which organic carbon and carbonate have been removed.

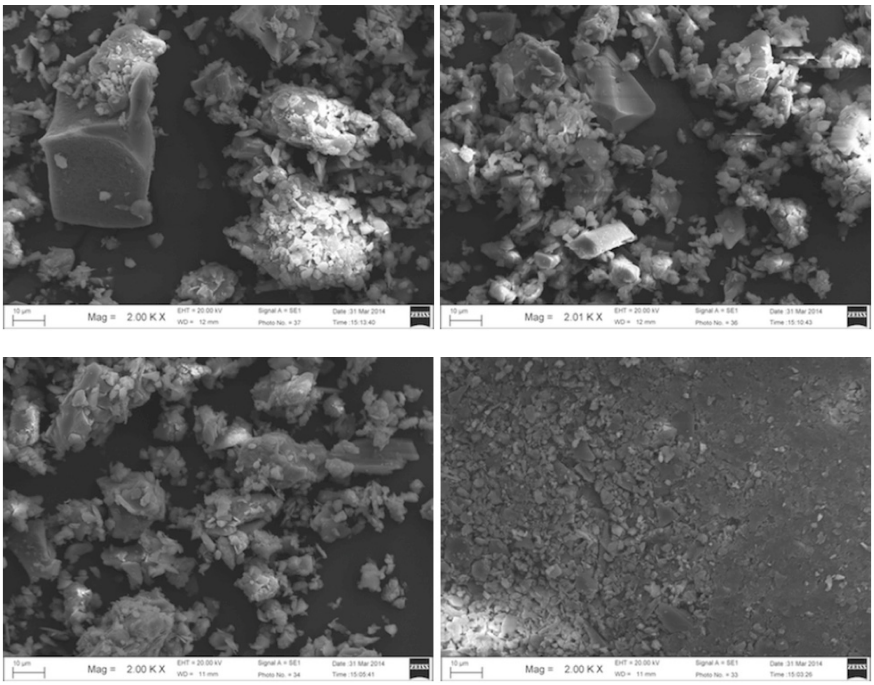


Figure B.3: SEM images of a Standard 1 from which organic carbon, carbonate and opal have been removed.

## B.2 Laboratory Standard 2

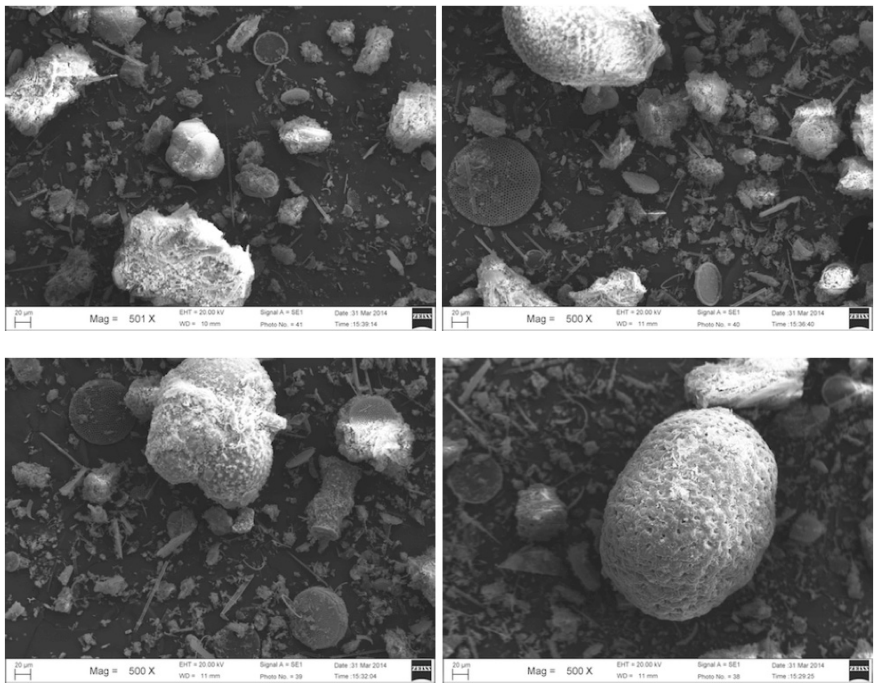


Figure B.4: SEM images of the freeze dried Standard 2 bulk sediment.

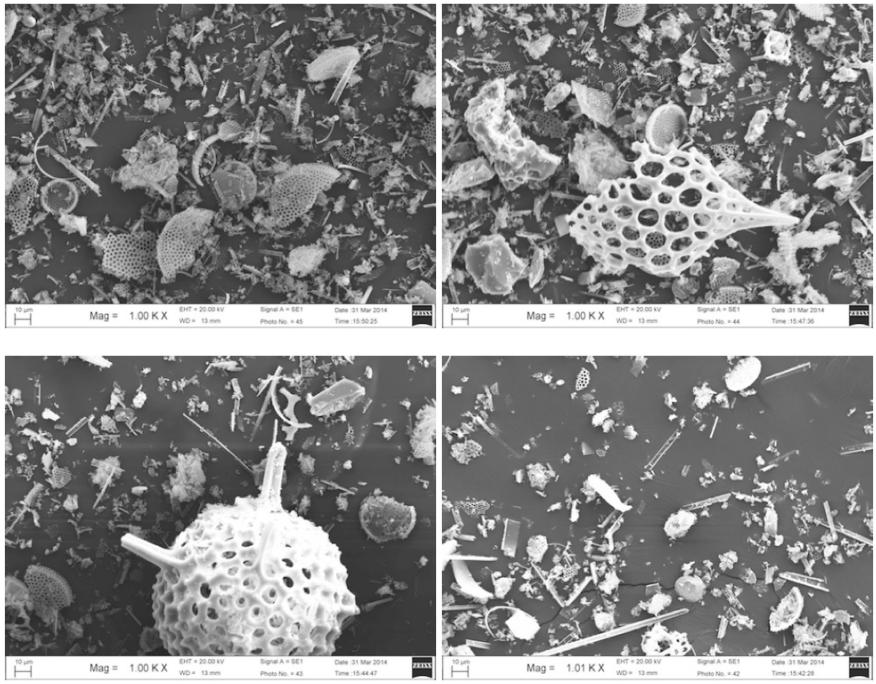


Figure B.5: SEM images of Standard 2 from which organic carbon and carbonate have been removed.

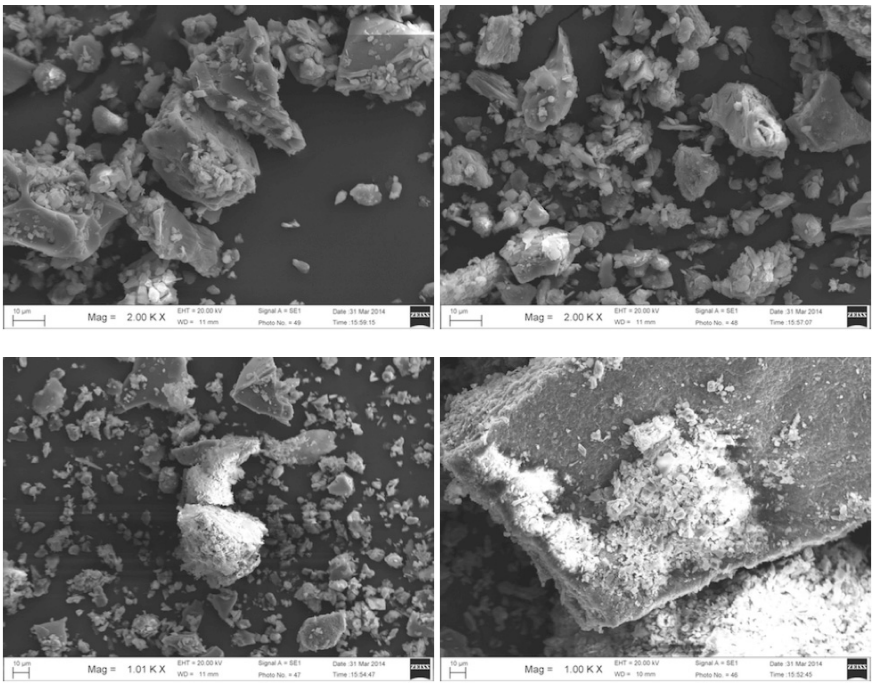


Figure B.6: SEM images of a Standard 2 from which organic carbon, carbonate and opal have been removed.

## B.3 ME0005A-27JC, 118 cm

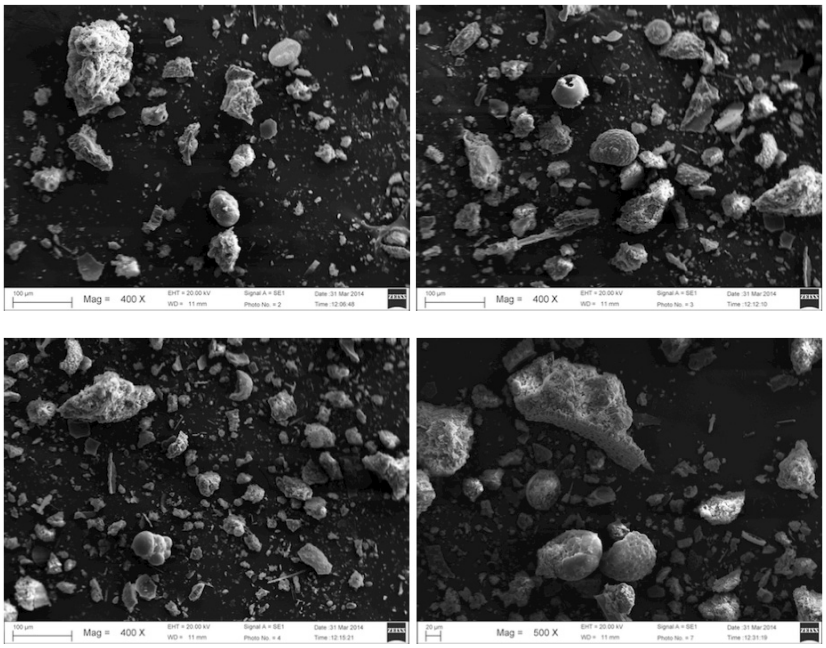


Figure B.7: SEM images of the freeze dried bulk sediment of ME0005A-27JC core (118 cm depth).

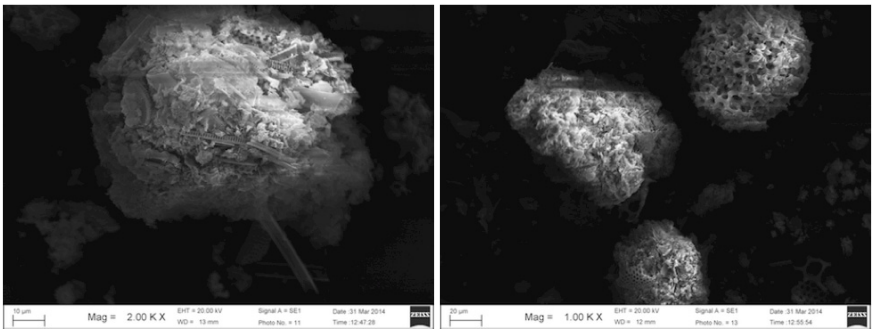


Figure B.8: SEM images of sediment of ME0005A-27JC core (118 cm) from which organic carbon and carbonate have been removed.

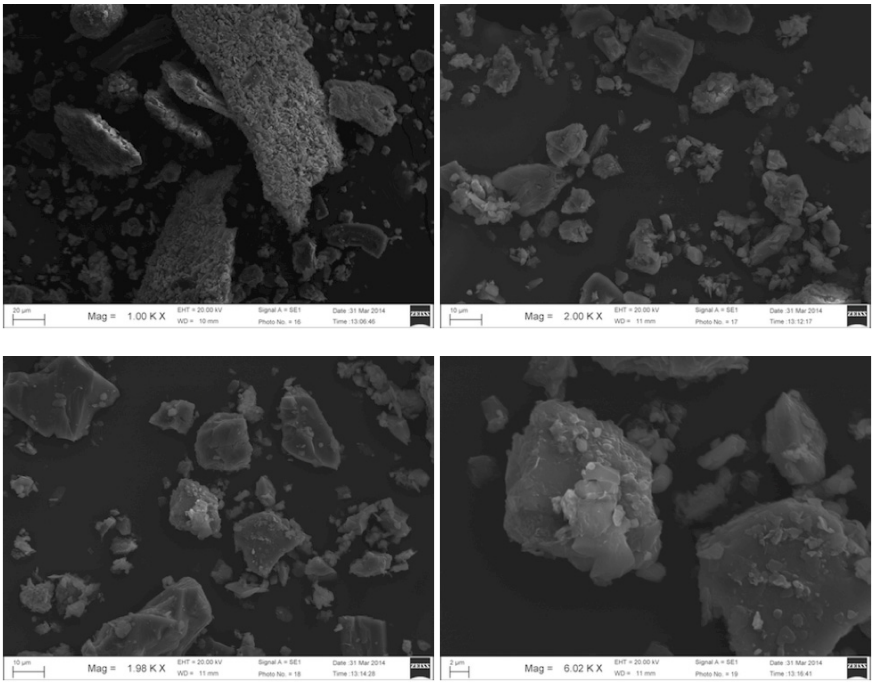


Figure B.9: SEM images of sediment of ME0005A-27JC core (118 cm) from which organic carbon, carbonate, opal have been removed.

# APPENDIX C

# FOCUSING FACTOR

*Kienast et al.* (2007) calculated the focusing factor for the three EEP cores (TR-19, ME-24 and ME-27) and discussed the dependence of focusing factor on the age model. This thesis uses an updated age model taken from (*Dubois et al.*, 2011) for these three cores. Because of this, the focusing factors change from the values presented by *Kienast et al.* (2007). Figure C.1 shows the focusing factors of the EEP cores for the same time intervals used by *Kienast et al.* (2007). When the focusing factors are calculated across only two time intervals over the last 30 ka, the values do not show significant changes from the previous estimates by *Kienast et al.* (2007) (Figure C.1(a)). With shorter time intervals (Figure C.1(b)), TR-19 and ME-27 show similar focusing factors but ME-24 shows significant differences in focusing factors between 9 to 21 ka. The divergence in calendar age based on the updated age model (Figure 2.3), makes the focusing factor lower ($\psi$= 5.8) than the previous estimate ($\psi$= 7.7, *Kienast et al.* (2007)) during the 9.5 -13.4 ka time interval. In turn, with the use of the updated age model, the focusing factor between 13.4 - 21 ka increases from $\psi$ = 5.9 (*Kienast et al.*, 2007) to $\psi$ = 8.2.

In addition, errors in the age model itself propagate to the calculation of focusing factors. Figure C.2 shows focusing factors for the EEP cores calculated for shorter time intervals (same as Figure 4.6) along with the errors that propagated from the errors in age model .

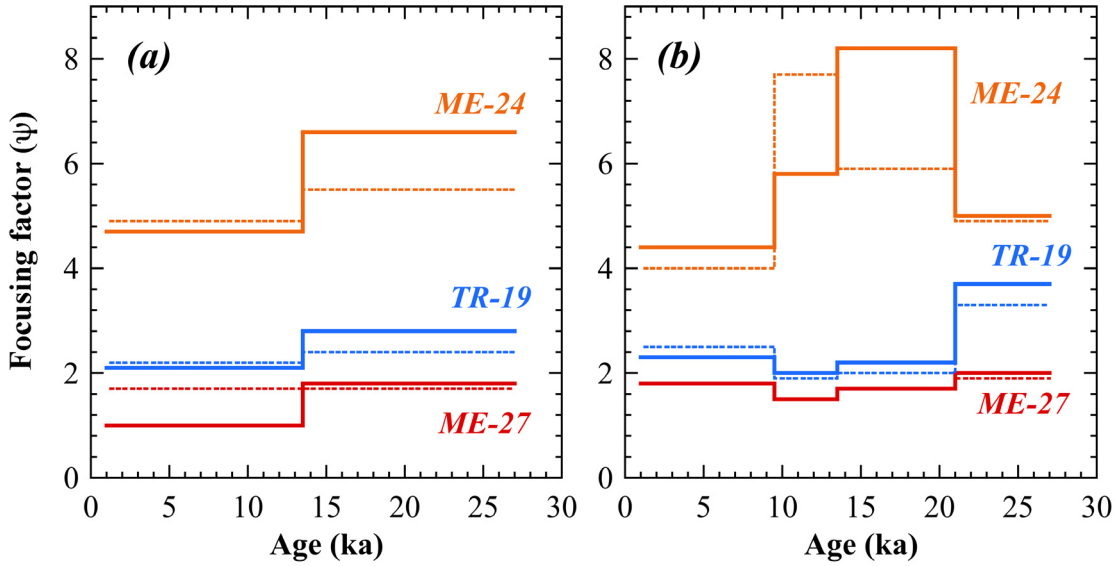


Figure C.1: Comparison between the focusing factors in *Kienast et al.* (2007) (dotted lines) and the focusing factors calculated using an updated age model (solid lines). (a) The time intervals from core top - 13.4 ka and 13.4 - 27 ka. (b) The time intervals from core top - 9.5, 9.5 - 13.4, 13.4 - 21, and 21 - 27 ka.

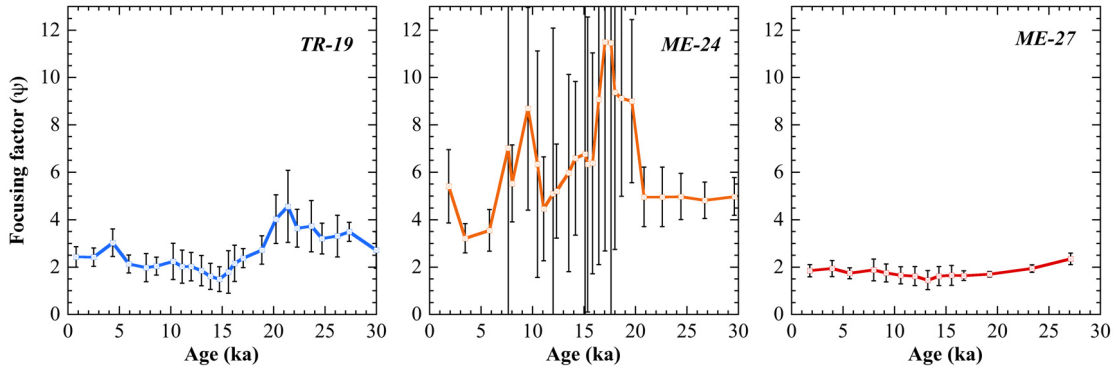


Figure C.2: Focusing factors calculated for small time intervals (same as Figure 4.6) with error bars resulting from the errors in age model in the EEP cores.

# BIBLIOGRAPHY


Albani, S., N. Mahowald, A. Perry, R. Scanza, C. Zender, N. Heavens, V. Maggi, J. Kok, and B. Otto-Bliesner, Improved dust representation in the community atmosphere model, *Journal of Advances in Modeling Earth Systems*, *6*, 541–570, 2014.

Anderson, R. F., M. Fleisher, and Y. Lao, Glacial interglacial variability in the delivery of dust to the central Equatorial Pacific Ocean, *Earth and Planetary Science Letters*, *242*, 406–414, 2006.

Anderson, R. F., M. Fleisher, Y. Lao, and G. Winckler, Modern $CaCO_3$ preservation in equatorial Pacific sediments in the context of late-Pleistocene glacial cycles, *Marine Chemistry*, *111*, 30–46, 2008.

Antoine, D., André, Jean-Michel, and A. Morel, Oceanic primary production: 2. estimation at global scale from satellite (coastal zone color scanner) chlorophyll, *Global biogeochemical cycles*, *10*, 57–69, 1996.

Averty, K., and A. Paytan, A comparison of multiple proxies for export production in the Equatorial Pacific, *Paleoceanography*, *19*, 2004.

Bacon, M. P., Glacial to interglacial changes in carbonate and clay sedimentation in the Atlantic Ocean estimated from $^{230}$Th measurements, *Chemical geology*, *46*, 97–111, 1984.

Bacon, M. P., and R. F. Anderson, Distribution of thorium isotopes between dissolved and particulate forms in the deep sea, *Journal of Geophysical Research: Oceans (1978–2012)*, *87*, 2045–2056, 1982.

Bishop, J. K., Determination of barium in seawater using vanadium/silicon modifier and direct injection graphite furnace atomic absorption spectrometry, *Analytical Chemistry*, *62*, 553–557, 1990.

Blott, S. J., and K. Pye, GRADISTAT: A grain size distribution and statistics package for the analysis of unconsolidated sediments, *Earth surface processes and Landforms*, *26*, 1237–1248, 2001.

Bopp, L., K. E. Kohfeld, C. Le Quéré, and O. Aumont, Dust impact on marine biota and atmospheric $CO_2$ during glacial periods, *Paleoceanography*, *18*, 2003.

Boyd, P. W., et al., Mesoscale iron enrichment experiments 1993-2005: Synthesis and future directions, *science*, *315*, 612–617, 2007.

Broecker, W., Excess sediment $^{230}$Th: transport along the sea floor or enhanced water column scavenging?, *Global Biogeochemical Cycles*, *22*, 2008.

Broecker, W. S., and G. M. Henderson, The sequence of events surrounding Termination II and their implications for the cause of glacial-interglacial $CO_2$ changes, *Paleoceanography*, *13*, 352–364, 1998.

Brzezinski, M. A., et al., Co-limitation of diatoms by iron and silicic acid in the Equatorial Pacific, *Deep Sea Research Part II: Topical Studies in Oceanography*, *58*, 493–511, 2011.

Calvert, S. E., and T. Pedersen, *Chapter fourteen- Elemental proxies for palaeoclimatic and palaeoceanographic variability in marine sediments: interpretation and application*, vol. 1, Elsevier, 2007.

Chavez, F. P., and R. T. Barber, An estimate of new production in the equatorial Pacific, *Deep Sea Research Part A. Oceanographic Research Papers*, *34*, 1229–1243, 1987.

Cheng, H., et al., Improvements in $^{230}$Th dating, $^{230}$Th and $^{234}$U half-life values, and u–th isotopic measurements by multi-collector inductively coupled plasma mass spectrometry, *Earth and Planetary Science Letters*, *371*, 82–91, 2013.

Chuey, J. M., D. K. Rea, and N. G. Pisias, Late pleistocene paleoclimatology of the central equatorial Pacific: A quantitative record of eolian and carbonate deposition, *Quaternary Research*, *28*, 323–339, 1987.

Coale, K. H., et al., A massive phytoplankton bloom induced by an ecosystem-scale iron fertilization experiment in the Equatorial Pacific Ocean, *Nature*, *383*, 495–501, 1996.

Corliss, J. B., M. Lyle, J. Dymond, and K. Crane, The chemistry of hydrothermal mounds near the Galapagos Rift, *Earth and Planetary Science Letters*, *40*, 12–24, 1978.

Curry, W., and G. Lohmann, Late Quaternary carbonate sedimentation at the Sierra Leone Rise (Eastern Equatorial Atlantic Ocean), *Marine Geology*, *70*, 223–250, 1986.

DeGelleke, L., P. S. Hill, M. Kienast, and D. J. Piper, Sediment dynamics during heinrich event H1 inferred from grain size, *Marine Geology*, *336*, 160–169, 2013.

DeMaster, D. J., The supply and accumulation of silica in the marine environment, *Geochimica et Cosmochimica acta*, *45*, 1715–1732, 1981.

Dietze, E., K. Hartmann, B. Diekmann, J. IJmker, F. Lehmkuhl, S. Opitz, G. Stauch, B. Wünnemann, and A. Borchers, An end-member algorithm for deciphering modern detrital processes from lake sediments of Lake /Donggi Cona, NE Tibetan Plateau, China, *Sedimentary Geology*, *243*, 169–180, 2012.

Dubois, N., and N. C. Mitchell, Large-scale sediment redistribution on the equatorial Pacific seafloor, *Deep Sea Research Part I: Oceanographic Research Papers*, *69*, 51–61, 2012.

Dubois, N., M. Kienast, S. Kienast, C. Normandeau, S. E. Calvert, T. D. Herbert, and A. Mix, Millennial-scale variations in hydrography and biogeochemistry in the Eastern Equatorial Pacific over the last 100 kyr, *Quaternary Science Reviews*, *30*, 210–223, 2011.

Duce, R., Sources, distributions, and fluxes of mineral aerosols and their relationship to climate, *Aerosol forcing of climate*, *6*, 43–72, 1995.

Duce, R. A., et al., The atmospheric input of trace species to the world ocean, *Global biogeochemical cycles*, *5*, 193–259, 1991.

Dugdale, R., A. Wischmeyer, F. Wilkerson, R. Barber, F. Chai, M.-S. Jiang, and T.-H. Peng, Meridional asymmetry of source nutrients to the Equatorial Pacific upwelling ecosystem and its potential impact on ocean atmosphere $CO_2$ flux; a data and modeling approach, *Deep Sea Research Part II: Topical Studies in Oceanography*, *49*, 2513 – 2531, 2002.

Dugdale, R., F. Chai, R. Feely, C. Measures, A. Parker, and F. Wilkerson, The regulation of equatorial Pacific new production and $pCO_2$ by silicate-limited diatoms, *Deep Sea Research Part II: Topical Studies in Oceanography*, *58*, 477– 492, 2011.

Dunk, R. M., R. Mills, and W. Jenkins, A re-evaluation of the oceanic uranium budget for the Holocene, *Chemical Geology*, *190*, 45–67, 2002.

Escobar, J., et al., A 43-ka record of paleoenvironmental change in the Central American lowlands inferred from stable isotopes of lacustrine ostracods, *Quaternary Science Reviews*, *37*, 92–104, 2012.

Faure, G., *Principles and applications of geochemistry: a comprehensive textbook for geology students*, Prentice Hall, 1998.

Fisher, N. S., R. R. Guillard, and D. C. Bankston, The accumulation of barium by marine phytoplankton grown in culture, *Journal of marine research*, *49*, 339–354, 1991.

Flemming, B. W., The influence of grain-size analysis methods and sediment mixing on curve shapes and textural parameters: implications for sediment trend analysis, *Sedimentary Geology*, *202*, 425–435, 2007.

Folk, R. L., and W. C. Ward, Brazos river bar: a study in the significance of grain size parameters, *Journal of Sedimentary Research*, *27*, 1957.

Francois, R., M. Frank, M. M. Rutgers van der Loeff, and M. P. Bacon, $^{230}$Th normalization: An essential tool for interpreting sedimentary fluxes during the late Quaternary, *Paleoceanography*, *19*, 2004.

Francois, R., et al., Comment on: "Do geochemical estimates of sediment focusing pass the sediment test in the equatorial Pacific?" by M. Lyle et al., *Paleoceanography*, *22*, 2007.

Ganeshram, R. S., R. François, J. Commeau, and S. L. Brown-Leger, An experimental investigation of barite formation in seawater, *Geochimica et Cosmochimica Acta*, *67*, 2599–2605, 2003.

Gardner, W. D., L. G. Sullivan, and E. M. Thorndike, Long-term photographic, current, and nephelometer observations of manganese nodule environments in the Pacific, *Earth and Planetary Science Letters*, *70*, 95–109, 1984.

GeoLiquids, I., *MSDS: Sodium Polytungstate*, Geoliquids, Inc., Prospect Height, IL, 2012, Retrieved from http://geoliquids.com/wp-content/uploads/2014/03/MSDS-Sodium-Polytungstate.pdf.

Gibbons, F. T., D. W. Oppo, M. Mohtadi, Y. Rosenthal, J. Cheng, Z. Liu, and B. K. Linsley, Deglacial $\delta^{18}$O and hydrologic variability in the tropical Pacific and Indian Oceans, *Earth and Planetary Science Letters*, *387*, 240–251, 2014.

Goldberg, E. D., and G. Arrhenius, Chemistry of pacific pelagic sediments, *Geochimica et Cosmochimica Acta*, *13*, 153–212, 1958.

Gregg, W. W., M. E. Conkright, P. Ginoux, J. E. O'Reilly, and N. W. Casey, Ocean primary production and climate: Global decadal changes, *Geophysical Research Letters*, *30*, 2003.

Griffith, E. M., and A. Paytan, Barite in the ocean–occurrence, geochemistry and palaeoceanographic applications, *Sedimentology*, *59*, 1817–1835, 2012.

Harrison, S. P., K. E. Kohfeld, C. Roelandt, and T. Claquin, The role of dust in climate changes today, at the last glacial maximum and in the future, *Earth-Science Reviews*, *54*, 43–80, 2001.

Hayes, C., R. Anderson, and M. Fleisher, Opal accumulation rates in the Equatorial Pacific and mechanisms of deglaciation, *Paleoceanography*, *26*, 2011.

Higgins, S. M., R. F. Anderson, F. Marcantonio, P. Schlosser, and M. Stute, Sediment focusing creates 100-ka cycles in interplanetary dust accumulation on the Ontong Java Plateau, *Earth and Planetary Science Letters*, *203*, 383–397, 2002.

IPCC, *Climate Change 2013: The Physical Science Basis. Contribution of Working Group I to the Fifth Assessment Report of the Intergovernmental Panel on Climate Change*, Cambridge University Press, Cambridge, United Kingdom and New York, NY, USA, 2013.

Jickells, T., et al., Global iron connections between desert dust, ocean biogeochemistry, and climate, *science*, *308*, 67–71, 2005.

Johnson, D. A., and T. C. Johnson, Sediment redistribution by bottom currents in the central Pacific, in *Deep Sea Research and Oceanographic Abstracts*, vol. 17, pp. 157–169, Elsevier, 1970.

Kienast, S., M. Kienast, A. C. Mix, S. Calvert, and R. François, Thorium-230 normalized particle flux and sediment focusing in the Panama Basin region during the last 30,000 years, *Paleoceanography*, *22*, 2007.

Kienast, S. S., T. Friedrich, N. Dubois, P. S. Hill, A. Timmermann, A. C. Mix, and M. Kienast, Near collapse of the meridional SST gradient in the eastern equatorial pacific during Heinrich Stadial 1, *Paleoceanography*, *28*, 663–674, 2013.

Kohfeld, K. E., and S. P. Harrison, Dirtmap: the geological record of dust, *Earth-Science Reviews*, *54*, 81–114, 2001.

Kranck, K., Sediment deposition from flocculated suspensions, *Sedimentology*, *22*, 111–123, 1975.

Kranck, K., and T. Milligan, Origin of grain size spectra of suspension deposited sediment, *Geo-marine letters*, *5*, 61–66, 1985.

Kretschmer, S., W. Geibert, M. M. R. van der Loeff, and G. Mollenhauer, Grain size effects on $^{230}\mathrm{Th}_{xs}$ inventories in opal-rich and carbonate-rich marine sediments, *Earth and Planetary Science Letters*, *294*, 131–142, 2010.

Ledbetter, M. T., A late Pleistocene time-series of bottom-current speed in the Vema Channel, *Palaeogeography, palaeoclimatology, palaeoecology*, *53*, 97–105, 1986.

Lisiecki, L. E., and M. E. Raymo, A Pliocene-Pleistocene stack of 57 globally distributed benthic $\delta^{18}$O records, *Paleoceanography*, *20*, 2005.

Locarnini, R. A., A. V. Mishonov, J. I. Antonov, T. P. Boyer, H. E. Garcia, O. K. Baranova, M. M. Zweng, and D. R. Johnson, World ocean database 2009, Volume 1: Temperature, *Ed. NOAA Atlas NESDIS 68*, p. 184, 2010.

Longsdale, P., and K. D. Klitgord, Structure and tectonic history of the eastern Panama Basin, *Geological Society of America Bulletin*, *89*, 981–999, 1978.

Loubere, P., F. Mekik, R. Francois, and S. Pichat, Export fluxes of calcite in the eastern equatorial Pacific from the Last Glacial Maximum to present, *Paleoceanography*, *19*, 2004.

Luo, C., N. M. Mahowald, and J. Del Corral, Sensitivity study of meteorological parameters on mineral aerosol mobilization, transport, and distribution, *Journal of Geophysical Research: Atmospheres (1984–2012)*, *108*, 2003.

Lyle, M., A. Mix, and N. Pisias, Patterns of $CaCO_3$ deposition in the eastern tropical Pacific Ocean for the last 150 kyr: Evidence for a southeast Pacific depositional spike during marine isotope stage (MIS) 2, *Paleoceanography*, *17*, 3–1, 2002.

Lyle, M., N. Mitchell, N. Pisias, A. Mix, J. I. Martinez, and A. Paytan, Do geochemical estimates of sediment focusing pass the sediment test in the equatorial Pacific?, *Paleoceanography*, *20*, 2005.

Lyle, M., N. Pisias, A. Paytan, J. I. Martinez, and A. Mix, Reply to comment by R. Francois et al. on "Do geochemical estimates of sediment focusing pass the sediment test in the equatorial Pacific?": Further explorations of $^{230}$Th normalization, *Paleoceanography*, *22*, 2007.

Maher, B., J. Prospero, D. Mackie, D. Gaiero, P. Hesse, and Y. Balkanski, Global connections between aeolian dust, climate and ocean biogeochemistry at the present day and at the last glacial maximum, *Earth-Science Reviews*, *99*, 61–97, 2010.

Mahowald, N., Aerosol indirect effect on biogeochemical cycles and climate, *Science*, *334*, 794–796, 2011.

Mahowald, N., K. Kohfeld, M. Hansson, Y. Balkanski, S. P. Harrison, I. C. Prentice, M. Schulz, and H. Rodhe, Dust sources and deposition during the last glacial maximum and current climate: A comparison of model results with paleodata from ice cores and marine sediments, *Journal of Geophysical Research: Atmospheres (1984–2012)*, *104*, 15895–15916, 1999.

Mahowald, N., S. Albani, S. Engelstaedter, G. Winckler, and M. Goman, Model insight into glacial–interglacial paleodust records, *Quaternary Science Reviews*, *30*, 832–854, 2011.

Mahowald, N. M., D. R. Muhs, S. Levis, P. J. Rasch, M. Yoshioka, C. S. Zender, and C. Luo, Change in atmospheric mineral aerosols in response to climate: Last glacial period, preindustrial, modern, and doubled carbon dioxide climates, *Journal of Geophysical Research*, *111*, D10202, 2006.

Marcantonio, F., R. F. Anderson, S. Higgins, M. Stute, P. Schlosser, and P. Kubik, Sediment focusing in the central equatorial Pacific Ocean, *Paleoceanography*, *16*, 260–267, 2001.

Marcantonio, F., M. Lyle, and R. Ibrahim, Particle sorting during sediment redistribution processes and the effect on $^{230}$Th-normalized mass accumulation rates, *Geophysical Research Letters*, *41*, 5547–5554, 2014.

Martin, J. H., Glacial-interglacial $CO_2$ change: The iron hypothesis, *Paleoceanography*, *5*, 1–13, 1990.

McCave, I., and I. Hall, Size sorting in marine muds: Processes, pitfalls, and prospects for paleoflow-speed proxies, *Geochemistry, Geophysics, Geosystems*, *7*, 2006.

McCave, I., B. Manighetti, and S. Robinson, Sortable silt and fine sediment size/composition slicing: parameters for palaeocurrent speed and palaeoceanography, *Paleoceanography*, *10*, 593–610, 1995.

McGee, D., F. Marcantonio, and J. Lynch-Stieglitz, Deglacial changes in dust flux in the eastern equatorial Pacific, *Earth and Planetary Science Letters*, *257*, 215–230, 2007.

McGee, D., F. Marcantonio, J. F. McManus, and G. Winckler, The response of excess $^{230}$Th and extraterrestrial $^{3}$He to sediment redistribution at the Blake Ridge, western North Atlantic, *Earth and Planetary Science Letters*, *299*, 138–149, 2010.

McGee, D., G. Winckler, J. Stuut, L. Bradtmiller, et al., The magnitude, timing and abruptness of changes in North African dust deposition over the last 20,000 yr, *Earth and Planetary Science Letters*, *371*, 163–176, 2013.

McGee, D., A. Donohoe, J. Marshall, and D. Ferreira, Changes in ITCZ location and cross-equatorial heat transport at the Last Glacial Maximum, Heinrich Stadial 1, and the mid-Holocene, *Earth and Planetary Science Letters*, *390*, 69–79, 2014.

Middleton, G. V., Hydraulic interpretation of sand size distributions, *The Journal of Geology*, pp. 405–426, 1976.

Miller, R., and I. Tegen, Climate response to soil dust aerosols, *Journal of climate*, *11*, 3247–3267, 1998.

Milligan, T., and K. Kranck, Electroresistance particle size analyzers, *Principles, Methods and Applications of Particle Size Analysis. Cambridge University Press, New York*, pp. 109–118, 1991.

Monnin, C., C. Jeandel, T. Cattaldo, and F. Dehairs, The marine barite saturation state of the world's oceans, *Marine Chemistry*, *65*, 253–261, 1999.

Moore Jr., T. C., G. R. Heath, and R. O. Kowsmann, Biogenic sediments of the Panama Basin, *The Journal of Geology*, *81*, 458–472, 1973.

Mortlock, R. A., and P. N. Froelich, A simple method for the rapid determination of biogenic opal in pelagic marine sediments, *Deep Sea Research Part A. Oceanographic Research Papers*, *36*, 1415–1426, 1989.

Mulitza, S., M. Prange, J. Stuut, M. Zabel, T. von Dobeneck, A. Itambi, J. Nizou, M. Schulz, and G. Wefer, Sahel megadroughts triggered by glacial slowdowns of Atlantic meridional overturning, *Paleoceanography*, *23*, 2008.

Murray, R., C. Knowlton, M. Leinen, A. C. Mix, and C. Polsky, Export production and carbonate dissolution in the central equatorial Pacific Ocean over the past 1 Myr, *Paleoceanography*, *15*, 570–592, 2000.

Murray, R. W., and M. Leinen, Chemical transport to the seafloor of the equatorial Pacific Ocean across a latitudinal transect at 135°W: tracking sedimentary major, trace, and rare earth element fluxes at the Equator and the Intertropical Convergence Zone, *Geochimica et Cosmochimica Acta*, *57*, 4141–4163, 1993.

Murray, R. W., M. Leinen, D. W. Murray, A. C. Mix, and C. W. Knowlton, Terrigenous Fe input and biogenic sedimentation in the glacial and interglacial equatorial Pacific Ocean, *Global biogeochemical cycles*, *9*, 667–684, 1995.

Murray, R. W., M. Leinen, and C. W. Knowlton, Links between iron input and opal deposition in the pleistocene equatorial Pacific Ocean, *Nature Geoscience*, *5*, 270–274, 2012.

Paytan, A., and M. Kastner, Benthic Ba fluxes in the central Equatorial Pacific, implications for the oceanic Ba cycle, *Earth and Planetary Science Letters*, *142*, 439–450, 1996.

Paytan, A., M. Kastner, E. Martin, J. Macdougall, and T. Herbert, Marine barite as a monitor of seawater strontium isotope composition, *Nature*, *366*, 445–449, 1993.

Paytan, A., M. Kastner, and F. Chavez, Glacial to interglacial fluctuations in productivity in the equatorial Pacific as indicated by marine barite, *Science*, *274*, 1355–1357, 1996.

Paytan, A., S. Mearon, K. Cobb, and M. Kastner, Origin of marine barite deposits: Sr and S isotope characterization, *Geology*, *30*, 747–750, 2002.

Peterson, L. C., G. H. Haug, K. A. Hughen, and U. Röhl, Rapid changes in the hydrologic cycle of the tropical Atlantic during the last glacial, *Science*, *290*, 1947–1951, 2000.

Prospero, J. M., Long-range transport of mineral dust in the global atmosphere: Impact of African dust on the environment of the southeastern United States, *Proceedings of the National Academy of Sciences*, *96*, 3396–3403, 1999.

Prospero, J. M., and E. Bonatti, Continental dust in the atmosphere of the Eastern Equatorial Pacific, *Journal of geophysical research*, *74*, 3362–3371, 1969.

Rea, D. K., The paleoclimatic record provided by eolian deposition in the deep sea: the geologic history of wind, *Reviews of Geophysics*, *32*, 159–195, 1994.

Rea, D. K., and S. A. Hovan, Grain size distribution and depositional processes of the mineral component of abyssal sediments: Lessons from the North Pacific, *Paleoceanography*, *10*, 251–258, 1995.

Reader, M., I. Fung, and N. McFarlane, The mineral dust aerosol cycle during the Last Glacial Maximum, *Journal of Geophysical Research: Atmospheres (1984–2012)*, *104*, 9381–9398, 1999.

Saukel, C., R. Stein, C. Vogt, and V. P. Shevchenko, Clay-mineral and grain-size distributions in surface sediments of the White Sea (Arctic Ocean): indicators of sediment sources and transport processes, *Geo-Marine Letters*, *30*, 605–616, 2010.

Schenau, S., M. Prins, G. De Lange, and C. Monnin, Barium accumulation in the Arabian Sea: Controls on barite preservation in marine sediments, *Geochimica et Cosmochimica Acta*, *65*, 1545–1556, 2001.

Siddall, M., R. F. Anderson, G. Winckler, G. M. Henderson, L. I. Bradtmiller, D. McGee, A. Franzese, T. F. Stocker, and S. A. Müller, Modeling the particle flux effect on distribution of $^{230}$Th in the equatorial Pacific, *Paleoceanography*, *23*, 2008.

Singh, A. K., F. Marcantonio, and M. Lyle, Sediment focusing in the Panama Basin, eastern equatorial Pacific Ocean, *Earth and Planetary Science Letters*, *309*, 33–44, 2011.

Singh, A. K., F. Marcantonio, and M. Lyle, Water column $^{230}$Th systematics in the eastern equatorial Pacific Ocean and implications for sediment focusing, *Earth and Planetary Science Letters*, *362*, 294–304, 2013.

Smith, W. H., and D. T. Sandwell, Global sea floor topography from satellite altimetry and ship depth soundings, *Science*, *277*, 1956–1962, 1997.

Snoeckx, H., and D. K. Rea, Dry bulk density and $CaCO_3$ relationships in upper Quaternary sediments of the eastern equatorial Pacific, *Marine Geology*, *120*, 327 – 333, 1994.

Suman, D. O., and M. P. Bacon, Variations in Holocene sedimentation in the North American Basin determined from $^{230}$Th measurements, *Deep Sea Research Part A. Oceanographic Research Papers*, *36*, 869–878, 1989.

Sun, D., Monsoon and westerly circulation changes recorded in the late Cenozoic aeolian sequences of Northern China, *Global and Planetary Change*, *41*, 63–80, 2004.

Sun, D., J. Bloemendal, D. Rea, J. Vandenberghe, F. Jiang, Z. An, and R. Su, Grain-size distribution function of polymodal sediments in hydraulic and aeolian environments, and numerical partitioning of the sedimentary components, *Sedimentary Geology*, *152*, 263–277, 2002.

Taylor, S. R., and S. M. McLennan, *The continental crust: Its composition and evolution*, Blackwell Scientific Pub., Palo Alto, CA, 1985.

Tegen, I., and A. A. Lacis, Modeling of particle size distribution and its influence on the radiative properties of mineral dust aerosol, *Journal of Geophysical Research: Atmospheres (1984–2012)*, *101*, 19237–19244, 1996.

Thomson, J., S. Colley, R. Anderson, G. Cook, A. MacKenzie, and D. Harkness, Holocene sediment fluxes in the northeast atlantic from $^{230}Th_{excess}$ and radiocarbon measurements, *Paleoceanography*, *8*, 631–650, 1993.

Timmermann, A., et al., The influence of a weakening of the Atlantic meridional overturning circulation on ENSO, *Journal of Climate*, *20*, 4899–4919, 2007.

Toggweiler, J., and S. Carson, What are upwelling systems contributing to the ocean's carbon and nutrient budgets?, *Environmental Science Research Report Es*, *18*, 337–360, 1995.

Toggweiler, J. R., K. Dixon, and W. S. Broecker, The peru upwelling and the ventilation of the south Pacific thermocline, *Journal of Geophysical Research: Oceans*, *96*, 20467–20497, 1991.

Twomey, S. A., M. Piepgrass, and T. Wolfe, An assessment of the impact of pollution on global cloud albedo, *Tellus B*, *36*, 356–366, 1984.

Van Andel, T. H., G. R. Heath, and T. C. Moore, Cenozoic history and paleoceanography of the central equatorial Pacific Ocean: A regional synthesis of deep sea drilling project data, *Geological Society of America Memoirs*, *143*, 1–223, 1975.

Van Beek, P., R. François, M. Conte, J.-L. Reyss, M. Souhaut, and M. Charette, $^{228}$Ra/$^{226}$Ra and $^{226}$Ra/Ba ratios to track barite formation and transport in the water column, *Geochimica et cosmochimica acta*, *71*, 71–86, 2007.

Wells, M. L., G. K. Vallis, and E. A. Silver, Tectonic processes in Papua New Guinea and past productivity in the eastern equatorial Pacific Ocean, *Nature*, *398*, 601–604, 1999.

Weltje, G. J., and M. A. Prins, Genetically meaningful decomposition of grain-size distributions, *Sedimentary Geology*, *202*, 409–424, 2007.

Winckler, G., R. F. Anderson, M. Q. Fleisher, D. McGee, and N. Mahowald, Covariant glacial-interglacial dust fluxes in the equatorial Pacific and Antarctica, *Science*, *320*, 93–96, 2008.

Xie, R. C., and F. Marcantonio, Deglacial dust provenance changes in the eastern equatorial Pacific and implications for ITCZ movement, *Earth and Planetary Science Letters*, *317*, 386–395, 2012.

Zhang, R., and T. L. Delworth, Simulated tropical response to a substantial weakening of the Atlantic thermohaline circulation, *Journal of Climate*, *18*, 1853–1860, 2005.

Zobeck, T. M., T. E. Gill, and T. W. Popham, A two-parameter Weibull function to describe airborne dust particle size distributions, *Earth Surface Processes and Landforms*, *24*, 943–955, 1999.